



## *Catalytic Upgrading of Biofuel Pyrolysis*

A thesis submitted by

**Andrew Harrison Hubble**

In partial fulfillment of the requirements

for the degree of

Doctor of Philosophy

in

Biological and Environmental Engineering

Bioenergy and Integrated Energy Systems

Cornell University

Ithaca, NY

May 2022

© 2022 Andrew Harrison Hubble

## Table of Contents

Executive Summary .....	i
Biographical Sketch .....	iii
Acknowledgements and Dedication .....	iv
List of Tables .....	v
List of Figures .....	vi
Chapter 1: Introduction .....	1
Chapter 2: Background .....	3
2.1 Pyrolysis .....	3
2.2 Pyrolysis Reactors .....	5
2.2.1 Batch Reactors .....	6
2.2.2 Fluidized Bed Reactors .....	6
2.3 Feedstock Selection .....	7
2.3.1 Cellulose .....	8
2.3.2 Hemicellulose .....	10
2.3.3 Lignin .....	13
2.4 Catalysts .....	17
2.4.1 Clay Mineral Catalysts .....	18
2.4.2 Transition Metal Catalysts .....	20
2.5 Scope of Work .....	22
Chapter 3: Synergistic Behavior Among Biomass Biopolymers .....	23
3.1 Materials and Methods .....	26
3.1.1 Generation of Pyrolysis Bio-oil .....	26
3.1.2 Characterization of Bio-oil via Gas Chromatography and Mass Spectroscopy .....	28
3.1.3 Thermal Analysis of Biomass Pyrolysis .....	29
3.2 Results and Discussion .....	31
3.2.1 Thermogravimetric Analysis .....	31
3.2.2 Analysis of Non-Condensable Gases .....	35
3.2.3 Bio-oil Analysis .....	38
3.3 Summary .....	44
Chapter 4: Transition Metals as <i>in situ</i> Catalysts for Cellulose .....	45
4.1 Materials and Methods .....	47
4.2 Results and Discussion .....	51
4.2.1 Proximate Analysis .....	52
4.2.2 Residual Gas Analysis .....	52
4.2.3 Gas Chromatography Mass Spectroscopy Analysis of Pyrolysis Bio-oil .....	57

4.3 Summary .....	66
Chapter 5: Coupling Materials Informatics and Transition Metal Catalysts .....	67
5.1 Pyrolysis Product Yields .....	70
5.2 Bio-oil Quality.....	72
5.3 Non-Condensable Gas Formation .....	72
5.4 Summary .....	74
Chapter 6: Transition Metals as <i>in/ex situ</i> Catalysts for Cherry Pits .....	75
6.1 Experimental Methods and Materials .....	76
6.1.1 Catalyst Preparation.....	77
6.1.2 Pyrolysis and Bio-oil Generation .....	77
6.1.3 Bio-oil extraction and GC-MS Analysis .....	78
6.1.5 Biochar Ultimate Analysis.....	79
6.2 Results and Discussion.....	80
6.2.1 Product Yields .....	80
6.2.2 Pyrolysis Bio-oil Composition .....	81
6.2.3 Biochar Composition.....	84
6.2.4 Non-Condensable Gas Formation .....	85
6.3 Summary .....	88
Chapter 7: Clay Minerals as <i>in situ</i> Catalysts for Cherry Pits .....	89
7.1 Experimental Materials and Methods .....	90
7.1.1 Production of Pyrolysis Bio-oil .....	90
7.2 Results and Discussion.....	90
7.2.1 Thermogravimetric Analysis .....	91
7.2.2 Impact of Biomass-Clay Pyrolysis on Product Distribution .....	91
7.2.3 Influence of Clay on Bio-oil Composition .....	94
7.3 Summary .....	97
Conclusions.....	99
Appendix A.....	I
Appendix B .....	IX
Appendix C .....	XVI
Appendix D.....	XIX
References.....	XXII

## **Executive Summary**

Anthropogenic climate change is driving the need for renewable and carbon free/neutral technologies to offset and replace traditional fossil fuels. One category of viable fossil fuel alternatives is biobased fuels – hydrocarbons in liquid, solid or gaseous form derived from dedicated crops, agricultural or municipal waste, or animal byproducts. These hydrocarbon fuels benefit from the high energy density of their chemical bonds, potentially reaching levels close to fossil fuels. Additionally, biobased fuels can be used in the existing combustion-focused infrastructure in transportation and power generation. Biobased fuels are carbon neutral (when properly managed) and can be used to sequester atmospheric carbon by generating solid biochars composed of stable graphitic carbon.

While there are numerous routes to generate biobased fuels, this work focuses on thermochemical conversion (specifically pyrolysis) of lignocellulosic biomass. Pyrolysis utilizes high temperatures under atmospheric pressure and anoxic conditions to devolatilize biomass and generate bio-oils, gases, and carbonized chars. The lack of oxygen prevents the biomass from combusting. Lignocellulosic biomass represents an underutilized resource. The United States generates hundreds of millions of tons of crop residues per year, which are typically left to decompose and return carbon (largely in the form of carbon dioxide) back to the atmosphere. The majority of this carbon is recycled between plants and atmosphere, and by converting these crop residues into biofuels, that carbon can be stored and used before returning to the carbon cycle.

The generation and use of liquid bio-oils derived from thermochemical conversion of lignocellulosic biomass has not seriously challenged the dominance of fossil fuels. These bio-oils are hampered by the formation of tar compounds that impart high acidity, viscosity, and instability,

which typically require substantial upgrading. The added cost of further refining and upgrading the bio-oils into biofuels has prevented lignocellulosic biofuels from widespread adoption. Part of this upgrading cost involves the use of rare or expensive catalysts which require recovery and recycling.

This work successfully reduced the formation of tar compounds during pyrolysis by utilizing *in situ* and *ex situ* catalysts to promote devolatilization and remove oxygenated functional groups. The catalysts used fall into two groups: transition metals and clay minerals. Both have demonstrated their effectiveness as catalysts for various thermochemical processes and benefit from widespread abundance translating to low costs. Because of their availability, these catalysts can be used once and do not require recharging or recycling. Additionally, this work has demonstrated the potential for the solid biochar to act as a water remediation tool.

Transition metals and clay minerals used in low quantities (<5% of biomass sample by weight) increased dehydrogenation and deoxygenation, and improved the oxygen/carbon ratios of bio-oils. Specifically, the use of *in situ* zinc reduced the overall bio-oil oxygen concentration without sacrificing yield. *Ex situ* manganese promoted high quantities of hydrogen and carbon dioxide in the non-condensable gas while retaining alcohol functional groups in the oil. Copper demonstrated an ability to promote devolatilization at earlier temperatures and reduced high molecular weight compounds. The clay montmorillonite promoted alkene (unsaturated) compounds and benzene derivatives in the bio-oil, and generated high quantities of H<sub>2</sub> gas. Attapulgite and illite clays reduced the fatty acid content and oxygen content of the bio-oils.

The transition metal and clay mineral catalysts have a varied impact biomass devolatilization, and their use can be tailored to the desired outcomes, depending on the specific issues of the biomass.

## **Biographical Sketch**

Andrew Hubble completed his Bachelor of Science degree in Mechanical Engineering with a concentration in power production, utilization, and forecasting at the Rose-Hulman Institute of Technology in 2011, and he completed a Master of Science degree in Mechanical Engineering at Tufts University in 2015. In the College of Agriculture and Life Sciences (CAL S) at Cornell University, Andrew received a degree for Master of Science in Biological and Environmental Engineering with a concentration in bioenergy and integrated energy systems in 2020, and received his Doctor of Philosophy (Ph.D.) with the same focus in 2022.

## **Acknowledgements and Dedication**

I would like to extend my sincere thanks to Cornell University for giving me the opportunity to further my academic career, and to Dr. Jillian Goldfarb for the guidance and financial support to make this possible. Although the work contained in this thesis is designed to highlight my efforts, this project was a collaborative effort between myself, Dr. Goldfarb, my committee, our collaborators at Boston University and Queen Mary University of London, and the entire team in the EME2 laboratory, without whom none of this would have been possible.

Additionally, I would like to thank my committee members Dr. Jefferson Tester, Dr. Emily Ryan, and Dr. Johannes Lehmann for their continued guidance and support both in and out of academia. I would also like to thank Zoe Pollard and Madeline Karod for their research expertise and patience in sharing a laboratory with me.

Finally, I would like to thank my family and friends outside of the university for all their support and love throughout this process.

Portions of this work were supported by the National Science Foundation under grant number 1933071, the Eppley Foundation for Research, and the President's Council of Cornell Women. This work made use of the Cornell Center for Materials Research Shared Facilities which are supported through the NSF MRSEC program (DMR-1719875).

## List of Tables

Table 2.1	Pyrolysis processes and approximate yields	4
Table 2.2	Composition of various lignocellulosic biomasses	8
Table 2.3	Hemicellulose composition across various biomasses	11
Table 2.4	Estimated monolignol linkage types for hardwood and softwood	15
Table 2.5	Clay minerals for use as catalysts	20
Table 2.6	Transition metals for use as catalysts	21
Table 3.1	Biomass constituent mixtures	26
Table 3.2	Proximate analysis of individual components and their mixtures ( $\pm$ one standard deviation)	31
Table 3.3	Actual and expected biochar yields	34
Table 3.4	Non-Condensable gas evolution of pure biopolymers	36
Table 3.5	Percent difference between observed and expected gas evolution via eqn. 3.3, positive values indicate synergistic (non-additive) behavior with enhanced gas evolution	37
Table 3.6	Bio-oil yield for pure components and mixtures with estimated furan and phenol concentrations	40
Table 3.7	Weight percent of biochar formed versus predicted from pyrolysis of pure polysaccharides and mixtures	43
Table 4.1	Percent change of metal uptake on cellulose (by mass)	48
Table 4.2	Percent change of copper and nickel uptake on cellulose	49
Table 4.3	Group and batch experimental pyrolysis matrix	50
Table 4.4	Proximate analysis of metal impregnated filter papers	52
Table 4.5	Average biochar, bio-oil, and bio-oil water yields at 600°C ( $\pm$ one standard deviation where $n > 2$ , otherwise error reported as percent difference between duplicate trials.)	58
Table 4.6	Group 1 bio-oil compound yields expressed as percent change in chromatogram area versus pure cellulose (negative indicates decrease in yield versus cellulose)	59
Table 5.1	Representative reactions for catalyst material informatics	68

## List of Figures

Figure 2.1	Linked Organics (Left), Decomposed (Right)	3
Figure 2.2	Batch Reactor	6
Figure 2.3	Fluidized Bed Reactor	7
Figure 2.4	Cellulose: $\beta$ -1,4-linked $\alpha$ -D-glucopyranose	9
Figure 2.5	$\alpha$ -D-glucopyranose in (A) Haworth-Projection (B) Chair Conformation (C) Stereochemical View	9
Figure 2.6	Hemicellulose monomer classification	12
Figure 2.7	Monolignols	14
Figure 2.8	Long-range lignin structure	15
Figure 2.9	Lignin Structures	16
Figure 2.10	2:1 Layered montmorillonite (Left) and 1:1 layered kaolin (Right)	19
Figure 3.1	Pyrolysis tube furnace setup	27
Figure 3.2	Representative derivative thermogravimetric mass loss curves of polysaccharide mixtures showing observed data versus expected mixture behavior as calculated via Eqn. 3.2	33
Figure 3.3	Pyrolysis gas evolution for individual biomass constituent compounds	35
Figure 3.4	Pyrolysis gas evolution for selected biomass mixtures (additional combinations available in Appendix A)	38
Figure 3.5	GC Chromatograms of bio-oil for individual biomasses	39
Figure 3.6	Cellulose and lignin bio-oil chromatogram	41
Figure 4.1	Pyrolysis tube furnace setup	51
Figure 4.2	Carbon dioxide (dashed) and hydrogen (solid) evolving for group 1 impregnated cellulose filter papers	53
Figure 4.3	Methane (dashed) and ethane (solid) evolution for group 1 impregnated cellulose filter papers	55
Figure 4.4	Averaged hydrogen gas evolution for batches 2 and 3 impregnated cellulose filter papers	56
Figure 4.5	Bio-oil compound distribution normalized to mass of input cellulose at 600°C and 100mL/min	61
Figure 4.6	Bio-oil compound distribution normalized to mass of input cellulose at 600°C and 200mL/min	63
Figure 4.7	Bio-oil compound distribution normalized to mass of input cellulose at 350°C and 100mL/min	64
Figure 5.1	Product distribution for transition metal catalysts on cellulose	70

Figure 5.2	Bio-oil yield as a function of average activation energy	71
Figure 5.3	Bio-oil oxygen concentration as a function of metal activation energy standard deviation	72
Figure 5.4	Pyrolysis gas production as a function of metal activation energy standard deviation	73
Figure 6.1	Pyrolysis flow diagram and location of transition metals	78
Figure 6.2	Product yields expressed as a weight percentage. *Gas yields calculated by difference	80
Figure 6.3	Oxygen content of bio-oils	81
Figure 6.4	Bio-oil functional group concentrations	82
Figure 6.5	Bio-oil Van Krevelen diagram	83
Figure 6.6	Biochar van Krevelen diagram	84
Figure 6.7	Carbon dioxide formation for in situ (above) and ex situ (below) transition metal catalysts. Pressure normalized to sample mass.	86
Figure 7.1	Dry basis derivative thermogravimetric curves for clay-cherry pit mixtures	91
Figure 7.2	Distribution of product yield for Cherry Pits (CP), Montmorillonite (Mont.), Attapulgit (Atta.), Illite, and Sand	92
Figure 7.3	Relative gas yields comparing clay-catalyzed pyrolysis to non-catalyzed pyrolysis (baseline). Abbreviations: Montmorillonite (Mont), Attapulgit (Atta).	93
Figure 7.4	Distribution of functional groups and structures in bio-oil across cherry pit samples. One compound can contain multiple functional groups or structures.	94
Figure 7.5	Bio-oil a) oxygen and b) fatty acid concentration	96
Figure 7.6	Bio-oil molecular weight	97

## Chapter 1: Introduction

Biomass is one of the oldest and most widely exploited energy sources; throughout much of history, the majority of our energy demand has been in the form of thermal energy through combustion. Thermal energy needs for warmth and cooking could easily be met by sparse agrarian societies using biomass<sup>1</sup>. Low population densities allowed people to harvest virgin biomass from the wilderness, or reuse the leftover waste from farming and ranching. Slowly, more energy-dense fuels were needed as high-power activities became commonplace, and attention turned to fossilized sources like coal and eventually oil. The industrial revolution, urbanization, and the demand for steam power increasingly drove our appetite for fossil fuels. With the widespread adoption of electricity, our energy needs have continued to evolve. An energy source's usefulness is no longer tied only to the heat it produces, but to the ability to convert that heat into electricity. The electrical revolution has presented options previously unfathomable, spurring unprecedented growth in almost every economic sector<sup>2</sup>. Our dependence on energy-dense fossil fuels, while convenient, is not sustainable. Society's belief in fossil fuel's abundance, and our early naivety of their impact on our planet has come full circle to the conclusion that our dependence on fossil fuels must end.

As energy production shifts increasingly toward renewable sources such as wind and solar, a new set of challenges arise<sup>3</sup>. In contrast to fossil fuels, renewable direct-electric sources contain no inherent capacity to store the energy produced, requiring new systems for storage. A carbon-neutral solution to this storage problem involves leaving the traditional combustion-energy infrastructure in place and rediscovering our original renewable fuel: biomass.

Just as energy-dense fossil fuels displaced raw biomass, newly upgraded forms of biochar and bio-oil are finding their niche in the energy market. There are select instances where raw biomass is still useful, however, the economic value and applicability of biomass as a whole is now tied to improving its energy density. Biofuel's use in mobile applications (or its transportation over long distances) requires a compact form, and its potentially high energy density stored as chemical energy makes it uniquely suited among the renewable options. Actively upgrading biomass is a balancing act between cost and quality; to compete with renewable and non-renewable alternate sources of energy, biomass must be upgraded inexpensively and in bulk. This work seeks to explore and improve the biofuel upgrading processes through pyrolysis, use of catalysts, and generation of secondary products to improve economic viability.

The literature has yet to identify all the appropriate interactions between feedstock biopolymers and catalysts, and this lack of understanding has left room for improvement for biomass pyrolysis. This work seeks to fill those gaps by providing a better understanding of the catalyst's role in primary/secondary pyrolysis, in turn providing a higher quality bio-oil that relies less on downstream upgrading to become a viable biofuel.

## Chapter 2: Background

An advantageous pathway for producing biofuels is thermochemical decomposition, which utilizes high temperatures (and sometimes high pressures) with or without oxygen to break down organic matter<sup>4</sup>. By breaking down this organic feedstock, smaller liquid compounds can be produced for use as fuel, or chemical feedstocks in various industrial applications<sup>5</sup>. Specifically, pyrolysis involves heating biomass to temperatures typically ranging from 400°C to 1000°C in anoxic conditions<sup>6</sup>, and is the main thermochemical process discussed throughout this work.

### 2.1 Pyrolysis

While combusting raw biomass yields significant thermal energy, biomass can be processed into more energy-dense forms through several different pathways. Whereas time-consuming biological approaches tends to be selective and result in large amounts of targeted products, thermal approach require shorter retention times and yield a wide variety of products. Pyrolysis is a thermochemical approach, that devolatilizes the biomass in the absence of oxygen. Figure 2.1 illustrates an example

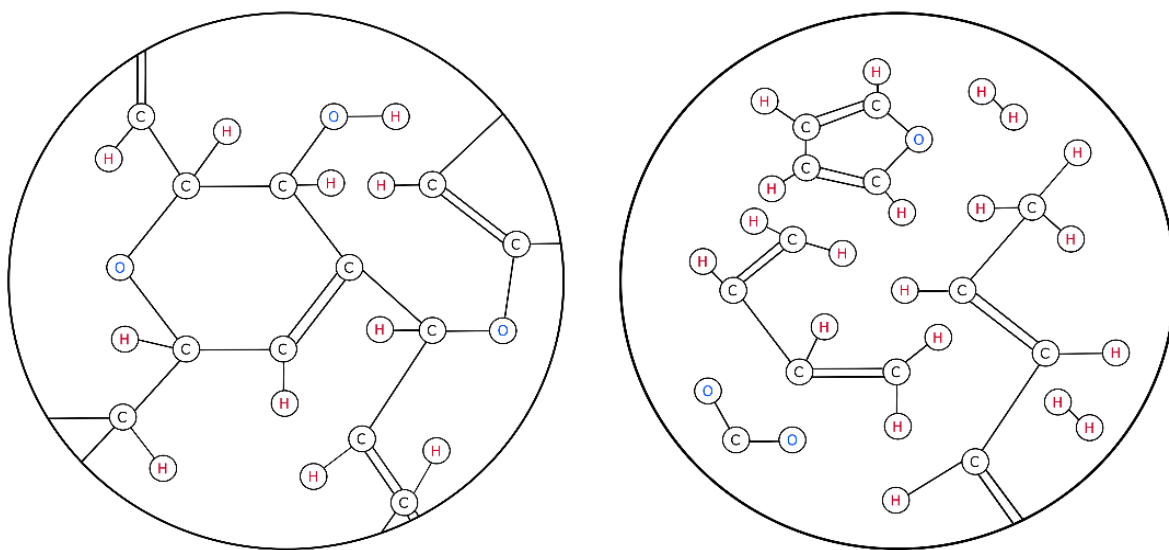


**Figure 2.1** Linked Organics (Left), Decomposed (Right)

of the raw biomass on the (left), and the pyrolytically devolatilized constituents (right). While slow pyrolysis is a mature technology, known for thousands of years, fast and flash pyrolysis have only been studied intensively for the past few decades. The interaction between temperature and residence time ultimately dictates the resultant product forms, as seen in Table 2.1<sup>6</sup>.

Torrefaction is considered a form of mild pyrolysis, as it does not produce the same quality of biochar; it is a precursor to the other forms. Torrefaction is used to generate large amounts of solid char used as a form of bio-coal (charcoal). After torrefaction, pyrolysis can be separated into three distinct types: Conventional (slow), fast, and flash pyrolysis. All three processes produce all three product types (solids, liquids, and gases), but to differing degrees. Slow pyrolysis and torrefaction are the most practiced forms, and are distinguished by low heating rates and long residence times; this combination generally yields a higher percentage of solid char. As fast and flash pyrolysis utilize shorter residence times, higher temperatures, and increased heating rates, the products shift towards liquids and gases. Notably, the bio-oil generated during fast and flash pyrolysis is significantly less viscous when compared to conventional pyrolysis. Fast and flash pyrolysis have

**Table 2.1** Pyrolysis processes and approximate yields

	Temperature (°C)	Residence Time	Heating Rate (°C/s)	Product Yield		
				Solids (wt%)	Liquids (wt%)	Gases (wt%)
<b>Torrefaction</b>	Low <300	Very Long hours	Low <10	80	0-5	15-20
<b>Conventional / Slow Pyrolysis</b>	Medium 400-500	Long min-hours	Low 10	45	30	35
<b>Fast Pyrolysis</b>	Med-High 400-650	Short 0.5-2 sec	High >100	25	50	25
<b>Flash Pyrolysis</b>	Very High 700-1000	Very Short <0.5 sec	Very High >500	12	75	13

become increasingly attractive options, since their liquid yields are high, up to 75% wt.<sup>7</sup>, and liquid fuel is more easily used over a larger range of energy-generation applications when compared to solid fuels. Solid fuels are typically limited to use in a steam cycle, which is effective in static electrical generation. Steam systems require longer lead times to start-up and shut-down, and are not suited well to changing demand. Liquids and gases are better suited to mobile transport in Otto, diesel, and Brayton cycles, and also play a major role in electrical generation when demand-response is an issue.

From an experimental process view, reactor designs are examined to balance advantages and disadvantages for specific scenarios. This is often to optimize a reactor design for a targeted feedstock. While there are innumerable reactor designs and variations, this work focuses on a few of the more common and widely-applicable including: ablative, free-fall, screw, batch, and fluidized bed reactors.

## **2.2 Pyrolysis Reactors**

The equipment needed to perform pyrolysis varies widely depending on the type of pyrolysis and products desired. While there are many components that are required to carry out pyrolysis effectively and efficiently, the reactor chamber is at the heart of the design. Since most of the input energy is expended in the reactor, this is where the physical and chemical transformation takes place. While there are many styles and variations of reactors, this work focuses on a select few common types with distinctive functionality<sup>8</sup>. Perhaps the simplest reactor to both imagine and build is the batch reactor.

### 2.2.1 Batch Reactors

Batch reactors are commonly used in torrefaction, and as the name implies, are not continuous processes. Seen in Figure 2.2, the reactor vessel is usually made up of brick, metal, or concrete, and is essentially a static housing with gas release for collection or venting. An electric or thermal combustion heat source can be used to drive the process, and to maximize heat transfer

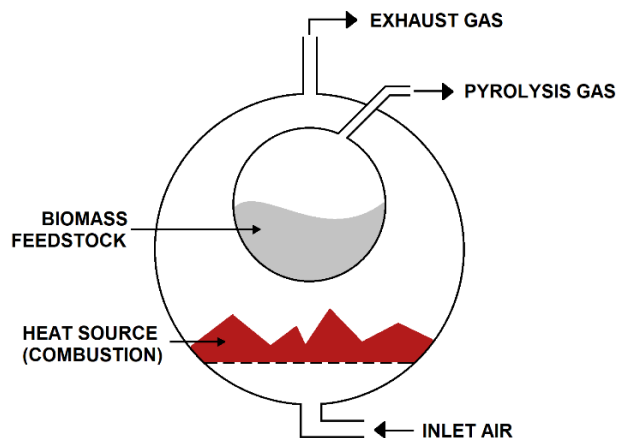


Figure 2.2 Batch reactor

and efficiency, the heat source often surrounds the reactor. Batch reactors tend to operate with long residence times and relatively low heat; the widespread applicability leads to impromptu and under-performing designs which make it difficult to achieve the temperatures needed for fast pyrolysis. The advantage, however, is the low capital and operating costs, and simplicity of operation<sup>9,10</sup>.

### 2.2.2 Fluidized Bed Reactors

While not directly used in this work, fluidized bed reactors (FBRs) will likely represent the eventual industry standard due to their scalability and ability to operate continuously. When developing the fundamental science behind new or improved processes, it is important to remain cognizant of how that knowledge will be implemented. FBRs provide excellent heat transfer rates but are limited by feedstock particle size. Figure 2.3 shows a finely ground feedstock being introduced into the reactor where it is often mixed with a heat transport medium such as sand. An inert gas flows up through the bottom of the reactor until the upward force of the gas and the weight

of the bed are approximately balanced. In this state, the feedstock mixes with the heated medium to reduce the temperature gradient throughout the reactor. Under higher gas flow rates some fine particulates entrained in the gas are swept from the reactor and must be recovered. This can be accomplished with cyclones, and the collected char can either be kept as a finished product, or combusted with the reactor medium and returned to the reactor to offset some or all of the heating load. Fluidized bed reactors are well suited to fast and flash pyrolysis heating rates and can generate large fractions of bio-oil and pyrolysis gas<sup>6,11,12</sup>.

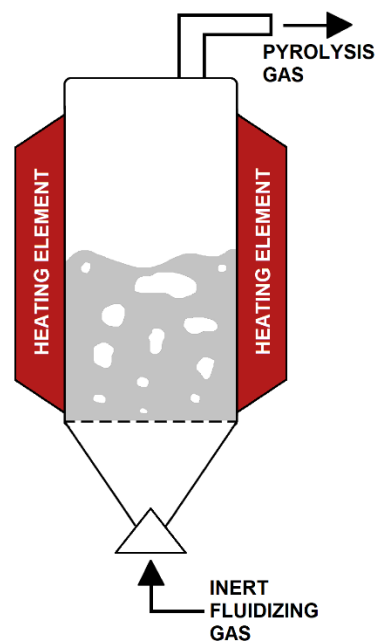


**Figure 2.3** Fluidized bed reactor

A big indicator for the success of fluidized bed reactors is measured by furanic compound production<sup>13-17</sup>, which have become the accepted benchmarks for the next generation of fuels<sup>18,19</sup>, and are one of the metrics used to evaluate the bio-oils produced in this work.

## 2.3 Feedstock Selection

Biomass is incredibly heterogeneous, and its pyrolysis products depend on the feedstock composition. Agricultural waste - the supporting plant matter remaining after the primary product is extracted – presents an opportunity to utilize otherwise wasted material. The bulk of plant matter comprises three major categories: cellulose, hemicellulose, and lignin. Each serve a different role and are found in varying ratios depending on the feedstock. Since the behavior of each category is critical to our understanding of pyrolysis, it is equally critical to understand their structure and

function. Cellulose, hemicellulose, and lignin can be further sub-divided into specific compounds. Despite the chemical complexity of plants, native cellulose, xylose/xylan, and kraft lignin are highly representative of how plant matter devolatilizes.

### 2.3.1 Cellulose

Cellulose is the most abundant single component of plants and is crucial to building and maintaining their structure. Despite being identified over 150 years ago, new discoveries in cellulose structure and function are still being made, and the study of its behavior under extreme conditions is still relatively

**Table 2.2** Composition of various lignocellulosic biomasses

	Composition (% dry weight)		
	Cellulose	Hemicellulose	Lignin
Corn Fiber	12	35	8
Corn Cob	45	35	15
Corn Stover	40	25	17
Rice Straw	35	25	12
Wheat Straw	30	50	20
Sugarcane Bagasse	40	24	25
Switchgrass	45	30	12
Coastal Bermuda Grass	25	35	6

nascent<sup>20-22</sup>. While it is the most abundant component, the proportion of cellulose to other organic matter varies tremendously across the biomass spectrum. Table 2.2 illustrates the relative quantities of cellulose, hemicellulose, and lignin across different agricultural samples<sup>23</sup>. Cellulose is a water-insoluble, strong, and fibrous material responsible for the structure of cell walls. Natural cellulose exists in a single form (cellulose I or native cellulose), although it can be converted to five other known polymorphs<sup>24</sup>.

Figure 2.4 depicts native cellulose, which exists as a homogeneous polysaccharide of  $\beta$ -1,4-linked glucose monomers ( $\alpha$ -D-glucopyranose). As aldehyde sugars are inherently unstable, they form ring structures. However, in understanding their behavior and function, it is important to note that

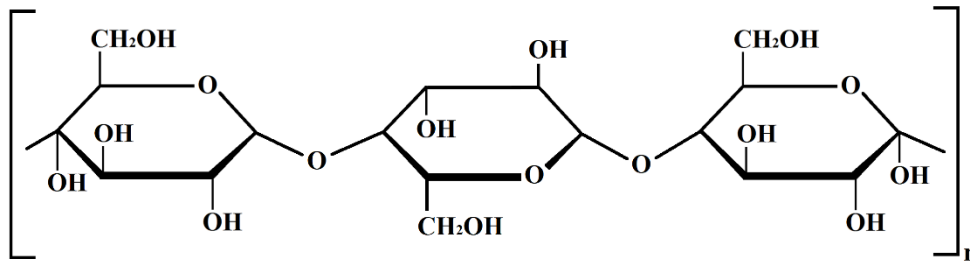


**Figure 2.4** Cellulose:  $\beta$ -1,4-linked  $\alpha$ -D-glucopyranose

unlike aromatic rings, these monomers are not planar. While typically drawn as a Haworth-projection,  $\alpha$ -D-glucopyranose is better represented through the chair configuration illustrated in Figure 2.5.

While native cellulose (cellulose I) is not the most stable form of cellulose, it is preferred by cellular synthesis. The glucopyranose monomers are bound through  $\beta$ -1,4-linkages, with alternating monomers reflected across the horizontal axis. Cellulose chains have a high degree of polymerization. In woody biomass, cellulose is composed of approximately 10,000 glucopyranose units, and cotton cellulose can exceed 15,000 units<sup>25</sup>. It is important to note that while chemically similar to starch, the  $\alpha$ -D-glucopyranose monomers in starch are isotactic. This seemingly small difference makes cellulose robust, water-insoluble, and indigestible to humans, while starch

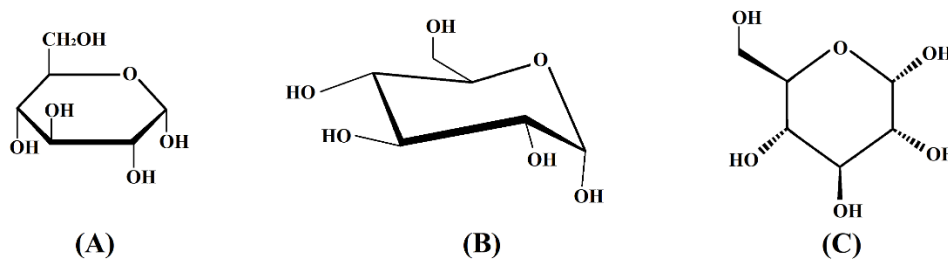


**Figure 2.5**  $\alpha$ -D-glucopyranose in (A) Haworth-Projection (B) Chair Conformation (C) Stereochemical View

displays none of these properties. Since native cellulose is so prevalent in the plant kingdom, and it exists in one dominant form, it makes an excellent candidate for study.

When undergoing thermochemical decomposition, cellulose depolymerizes and forms free radicals at pyrolysis temperatures above 100°C. Up to 300°C, cellulose pyrolysis results in the formation of carbonyl and carboxyl groups, CO and CO<sub>2</sub>, and biochar, a solid carbonaceous residue<sup>26</sup>. From 300-450°C, cellulose's glucose monomers begin to open and dehydrate, forming levoglucosan (a dehydrated glucose ring) and other anhydrides and oligosaccharides<sup>27-29</sup>. Tar compounds (e.g. levoglucosan) formed over this temperature regime result in a liquid bio-oil that is acidic, unstable, and heavily oxygenated<sup>30,31</sup>. Above 450°C, smaller carbonyl compounds such as acetaldehyde, glyoxal, and acrolein form, which are more desirable than large tar compounds from the previous phase<sup>27,32-34</sup>.

### **2.3.2 Hemicellulose**

Plant cell walls contain between 20-30% hemicellulose and hemicellulose is the secondmost abundant polysaccharide following cellulose<sup>35</sup>. Hemicellulose is a structural component, and while similar to cellulose, is generally found as shorter branched chains. Hemicelluloses are mixtures of cellulosic polymers. Just as the relative amounts of cellulose, hemicellulose, and lignin are dependent on the feedstock, the composition of hemicellulose varies across biomass. Hemicellulose derived from softwood is abundant in glucomannans, while hardwood hemicellulose contains mostly xylans<sup>23</sup>. This diversity can be illustrated in Table 2.3<sup>35</sup>, which shows approximate relative concentrations of hemicellulose monomers across different biomasses.

The two monomer classes of hemicellulose are hexose and pentose, which are further defined as five unique monomers (glucose, galactose, mannose, xylose, and arabinose) detailed in Figure 2.6. Just as the cellulose monomers are not planar, hexoses and pentoses are similarly structured. When formed into polymers, hemicellulose is classified into three families (xylans, mannans, and galactans), which are dependent on how the monomers come together. The polymer classes are grouped by the major backbone, which can consist of nearly-pure monomers, or highly intricate mixtures. Xylans typically consist of a  $\beta$ -1,4 - *linked* xylose backbone, with 10-40% of the xyloses containing a side group. Many of the side-group branches are connected with arabinose, which may terminate after a single monomer, or may form longer chains of mixed hemicelluloses. Similar to xylan, galactan polymers are constructed of a  $\beta$ -1,3-*linked* galactose backbone, with arabinose as the most common side-group<sup>35</sup>.

**Table 2.3** Hemicellulose composition across various biomasses

	<b>Composition (% dry weight)</b>			
	Mannose	Galactose	Xylose	Arabinose
<b>Softwood</b>				
Balsam Fir	12.4	1.0	4.8	0.5
Jack Pine	10.6	1.4	7.1	1.4
White Spruce	11.6	1.2	6.8	1.6
<b>Hardwood</b>				
Aspen	2.3	0.8	16.0	0.4
White Birch	1.5	0.6	24.6	0.5
Red Maple	3.5	0.6	17.3	0.5
<b>Agricultural Residue</b>				
Barley Straw	1.3	1.7	15.0	4.0
Corn Stover	0.3	0.8	13.0	2.8
Cotton Gin Trash	1.9	0.1	4.0	2.0
Rice Husks	2.7	0.1	12.3	2.6
Rice Straw	1.6	0.4	13.0	4.0
Sorghum Straw	0.8	0.2	15.0	3.0
Wheat Straw	0.7	2.2	16.9	2.1

Mannans are more heterogeneously arranged than the other polymer structures. Instead of having a consistent nearly-homogeneous backbone, mannans can be subdivided into four types. Of these, mannan is the purest form, containing over 95% mannose, with trace amounts of galactose<sup>36</sup>. Because it has high level of purity, mannan is more similar to xylan and galactan. Mannan is found in vegetable ivory<sup>37</sup>, orchid tubers<sup>38</sup>, and coffee beans<sup>39</sup>. Glucomannan is constructed of a random sequence of mannose and glucose, nearly always favoring mannose. Specifically, hardwood glucomannan contains no side groups and typically has a mannose-to-glucose ratio of 1:1 to 2:1, while softwoods have side groups and display mannose-to-glucose ratios of 3:1 to 4:1. Galactose side groups are spaced every 15 to 30 mannose units. Galactomannan can be found in legumes and guaran, and consists of a mannose-glucose backbone, with a respective ratio between 1:1 and 5:1. Distinguishing itself from glucomannan, galactomannan contains galactose side groups spaced every second mannose unit, yielding a much denser branching chain. Galactoglucomannan, as the name suggests, combines glucose and galactose with the mannose backbone. It has a lower degree of polymerization than glucomannan, but is otherwise similar. Galactose side groups are attached to both mannose and glucose monomers<sup>35</sup>.

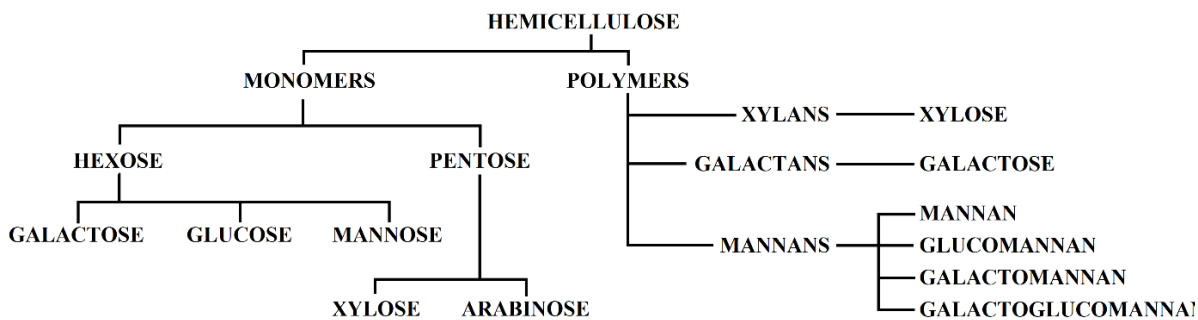


**Figure 2.6** Hemicellulose monomer classification

Hemicellulose decomposes at lower temperatures as compared to cellulose. It is very reactive above 100°C, and is a large driver of furan production<sup>40-44</sup>, often considered a desirable product for the integrated biorefinery<sup>45</sup>. The most abundant hemicellulose, xylan<sup>42,43</sup>, yields eight main products while undergoing thermal decomposition: water, methanol, acetic acid, formic acid, propionic acid, hydroxyacetone, acetoin, and furfural<sup>46</sup>.

This thesis focuses on the monomer and polymer forms of the same hemicellulose: xylose and xylan, respectively. Xylan is the most abundant hemicellulose and is prevalent across hardwoods and agricultural residues<sup>47</sup>. Utilizing different forms of the same hemicellulose allow for a deeper understanding of not just how the sugar chemistry affects thermochemical decomposition, but what effect the forms have on this outcome.

### **2.3.3 Lignin**

When compared to cellulose and hemicellulose, lignin is incredibly complex and comprises diverse structures. Lignin accounts for 10-25% of most plant matter mass and represents an even higher percentage for woody biomasses. While lignin is present in agricultural waste, wood pulping is one of the most significant sources of lignin waste. While lignin also exists in the cell walls, it serves as a higher-degree of support for vascular tissue, and is highly resistant to biodegradation.

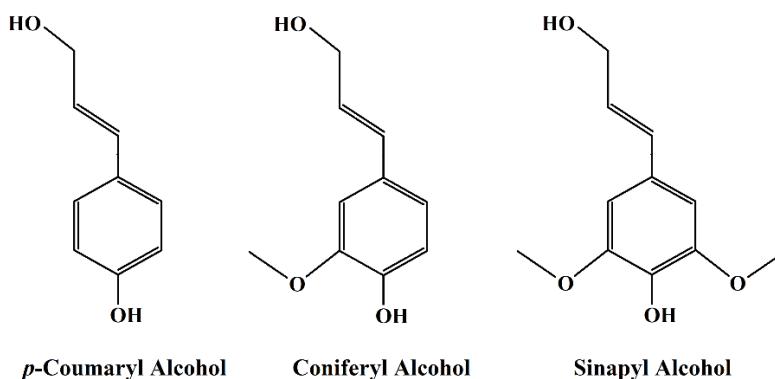


**Figure 2.7** Monolignols

Despite lignin’s modern role in waste valorization, lignin has a previously complicated past with energy. Much of the coal that has powered our society stems from lignin and the naturally slow carbonization it has undergone over millions of years. The Carboniferous period spanned about 60 million years and ended over 300 million years ago. During this time trees began to compete in an arms race to out-grow each other for access to the sun; lignin and its rigid structure was central to this massive growth explosion. Coupled with their underdeveloped root systems, these new fast-growing pencil-thin trees toppled at a staggering rate and began to litter the forest floor. At the same time, lignin’s structure was so new that there were no microbes that could break the tough carbon bonds and decompose the fallen trees. For nearly 60 million years the trees were piled and sequestered beneath each other. The pressure transformed those trees into peat, and eventually over time, into coal<sup>48</sup>.

One of the reasons microorganisms were delayed in developing the tools needed to break lignin down stems from lignin’s cross-linked and seemingly unordered nature. Even today the exact structure of protolignin (untreated lignin from plants) is unknown<sup>49,50</sup>. The structure of lignin is believed to be a combination of the three monolignols depicted in Figure 2.7<sup>50</sup>, with the long-range

order seen in Figure 2.8<sup>50</sup>. These monolignols are cross-linked through a series of linkage types, which vary across sources, and are listed in Table 2.4<sup>49</sup>. To complicate matters, the cross-linking between monolignols exhibit no predictable pattern, and the monolignols themselves often appear fragmented, which raises further questions about our understanding of lignin structures<sup>50</sup>.

**Table 2.4** Estimated monolignol linkage types for hardwood and softwood

Linkage Type	Estimated Percentage (%)	
	Softwood	Hardwood
$\beta - O - 4$	45-50	60
5 - 5	18-25	5
$\beta - 5$	9-12	6
4 - O - 5	4-8	7
$\beta - 1$	7-10	7
$\beta - \beta$	3	3

Although lignin is defined by its monolignols and linkage types, in an experiment lignin is often separated into model compounds. Figure 2.9 illustrates some examples of these model compounds<sup>49</sup>. These compounds are available, and since they are functionally different, can provide insight into the interactions between each other and the cellulose and hemicellulose compounds.

Eugenol is similar to the monolignol coniferyl alcohol with a notable difference; the functionalized alkyl chain (which can serve as a target for dealkylation reactions) has the double bond moved to

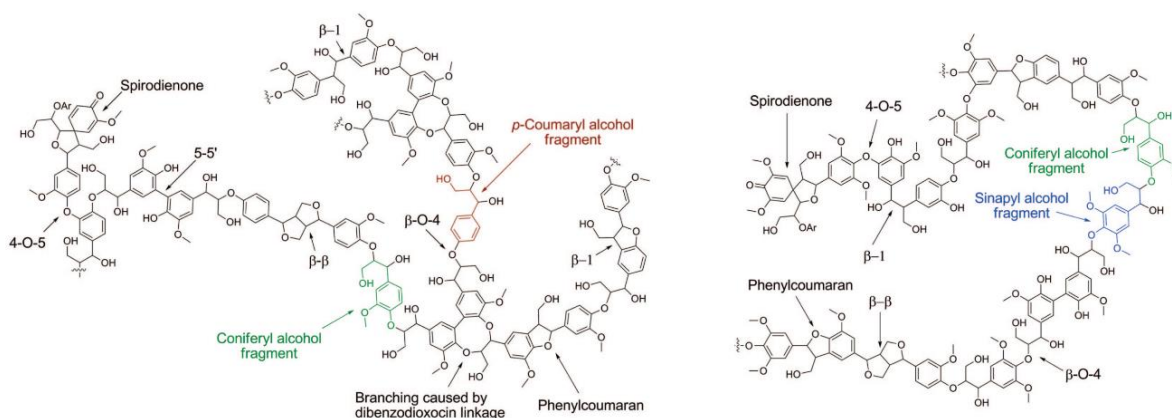


**Figure 2.8** Long-range lignin structure

the end. Additionally, eugenol contains the guaiacol aromatic ring prevalent throughout the lignin structure, and therefore serves as the most representative complex of lignin. Studies on eugenol are ubiquitous and the literature provides a comprehensive baseline for our understanding of eugenol's behavior<sup>51</sup>.

Conversely, while eugenol serves as the model monolignol,  $\beta$ -aryl ether represents the most common linkage type:  $\beta$ -O-4.  $\beta$ -aryl ether embodies 45-50% of  $\beta$ -O-4 linkages in softwood and 60% in hardwood, seen in Table 2.4.  $\beta$ -aryl ether has been a focal point in the literature and is well studied and understood<sup>52</sup>. From an experimental viewpoint, disentangling lignin's complex and highly variable structure, and understanding how these components interact and contribute to the chemistry of thermal decomposition is a field of research on its own. This thesis will also examine lignin as a bulk material – supplied as a waste product of the pulping industry and in turn available in sulfonated and low sulfonate forms. This insures representation of a wide variety of linkages and aromatics.

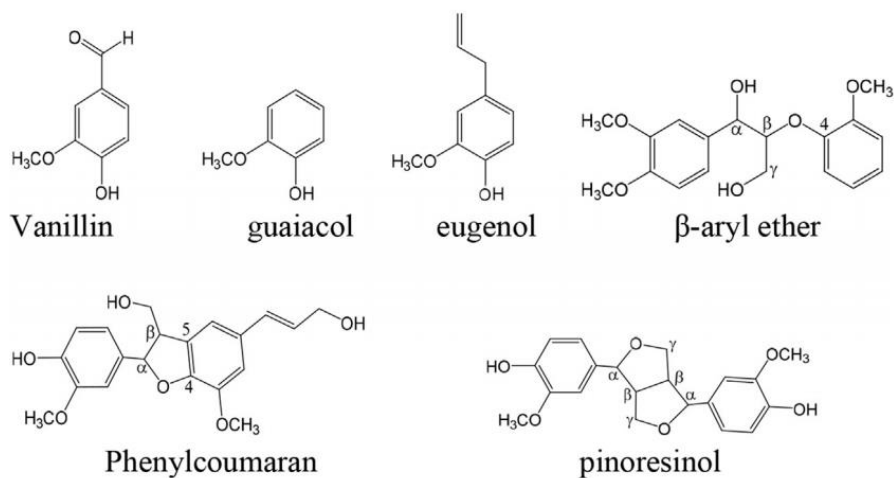


**Figure 2.9** Lignin structures

Lignin devolatilizes at higher temperatures than cellulose or hemicellulose. Extensive cleavage of one of the most prevalent and well-understood linkage types ( $\beta$ -aryl ether or  $\beta$ -O-4) begins around 270°C and peaks at 350-450°C<sup>27</sup>. As the dominant linkage in many lignocellulosic biomasses, scission of  $\beta$ -aryl ether (and similar linkages) yields products that resemble the individual phenolic monolignols<sup>53-56</sup>. Since lignin has a highly aromatic structure, it tends to produce more aromatic compounds upon pyrolysis.

To understand or predict how mixed feedstocks behave during pyrolysis, its necessary to study their individual components: lignin, hemicellulose, and cellulose. Since a biomass pyrolysis industry is not sustainable if it relies only on heavily treated pure biopolymers, it is imperative to understand how these biopolymers interact during thermochemical devolatilization, and how the combination of these biopolymers mimics mixed biomass. This work will examine the synergistic effects of mixing biopolymers to further our understanding of biopolymer interaction.

## 2.4 Catalysts

The current use of thermochemical conversion (specifically pyrolysis) techniques to generate liquid bio-oils from lignocellulosic biomass yields products requiring further processing and conversion before they can be effectively used. The pyrolysis process generates a heterogeneous oil containing oxygenated tar compounds which reduce its energy density and stability, and increase acidity and viscosity<sup>57,58</sup>. Catalysts are commonly used in downstream processes to improve the quality of bio-oils, at great expense<sup>59,60</sup>. Adding additional steps for processing, or relying on rare and expensive catalyst combinations threatens the economic feasibility of an inexpensive pyrolysis-derived lignocellulosic biofuel. Catalysts can be utilized during the

pyrolysis process, and while their current application is limited, these *in situ* catalysts are effective<sup>61,62</sup>. *In situ* catalysts remove or reduce the need for equipment and energy inputs further downstream by utilizing the catalyst to redirect the pathways during the initial bio-oil formation. This work focuses on the *in situ* approach to help demonstrate its viability, reduce operational costs and steps, and explore the effects of catalysts on non-targeted pathways. To reduce reliance on expensive and rare catalysts, this work explores the use of clay minerals and silicates, as well as transition metals as catalysts. These two groups represent a large untapped potential for single-use catalysts and have demonstrated their feasibility as catalysts previously<sup>63-66</sup>.

#### **2.4.1 Clay Mineral Catalysts**

Clay minerals have been successfully used as catalysts in a range of applications including thermochemical treatment of plastic wastes<sup>67</sup>, hydrolysis of cellulose<sup>68</sup>, degradation of organic dyes<sup>69</sup>, and dry reforming of methane<sup>70</sup>. Specifically, aluminosilicates contain high amounts of aluminum, and silicon with lower quantities of magnesium, iron, or calcium. The two most notable forms are 1:1 and 2:1 layered silicates. The structures of both kaolin and montmorillonite seen in Figure 2.10 illustrates the repetitive tetrahedral pattern. Montmorillonite contains two sheets of silicon surrounding a single layer of alumina, whereas kaolin contains only one layer of alumina.

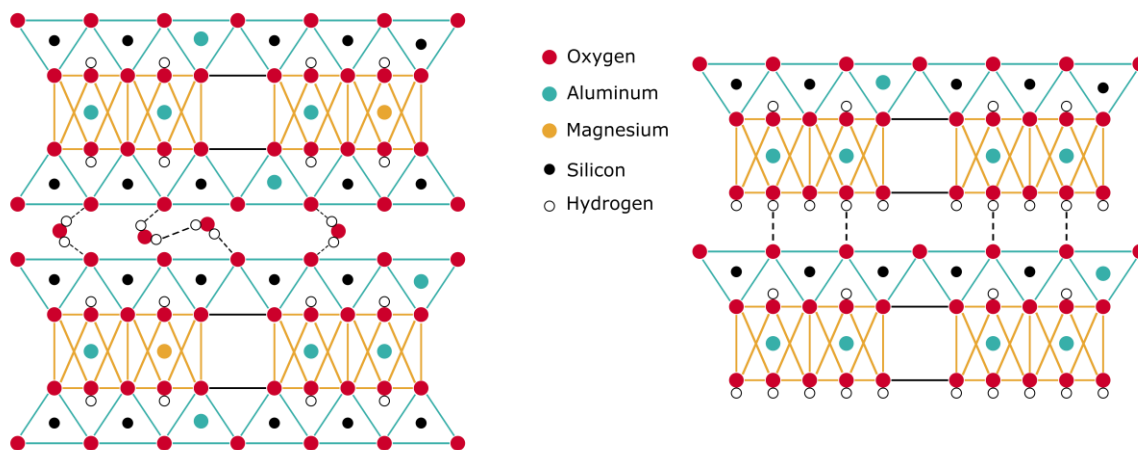


**Figure 2.10** 2:1 Layered montmorillonite (Left) and 1:1 layered kaolin (Right)

These sheets are loosely bonded together and usually contain interstitial moisture<sup>71</sup>. Clay silicates are naturally abundant and inexpensive, and because of this could be utilized once during processing before being discarded. An additional hurdle with expensive or rare catalysts is the desire to recycle them. The recycling of catalysts can be difficult due to the tendency for catalysts to become inactivated during use, due to coking<sup>72</sup>. Many catalysts cannot be filtered out and reused without first removing the coke formation, which adds additional steps and costs. By utilizing clay mineral as single-use catalysts, this problem can be avoided.

This work focuses on five different clay catalysts, detailed in Table 2.5. In order to compare or select the appropriate clay mineral for use, a representative range of classes and cation exchange capacities (CEC) were selected. Sand, while included in this list, represents a control, whereby inert material is added to the system to mimic mass and heat transport effects, without providing exchange site functionality. Measuring the CEC for dolomite is problematic due to the calcium released by dissolution<sup>73</sup>.

**Table 2.5** Clay minerals for use as catalysts

Silicate	Class	Structure	Cation Exchange Capacity (m <sub>eq</sub> /100g)
Sand	Sand	SiO <sub>2</sub>	0
Montmorillonite	Smectite	(Na,Ca) <sub>0.33</sub> (Al,Mg) <sub>2</sub> (Si <sub>4</sub> O <sub>10</sub> )(OH) <sub>2</sub> ·nH <sub>2</sub> O	60-100
Kaolin	Kaolinite	Al <sub>2</sub> O <sub>3</sub> ·2SiO <sub>2</sub> ·2H <sub>2</sub> O	3-15
Illite	Illite	(Na,H <sub>3</sub> O)(Al,Mg,Fe) <sub>2</sub> ((Si,Al) <sub>4</sub> O <sub>10</sub> )(OH) <sub>2</sub>	20-40
Attapulgite	Smectite-Palygorskite	(Mg,Al) <sub>2</sub> Si <sub>4</sub> O <sub>10</sub> (OH)·4(H <sub>2</sub> O)	170
Dolomite	Dolomite	CaMg(CO <sub>3</sub> ) <sub>2</sub>	Unavailable*

\* determination of CEC in samples containing carbonate minerals such as calcite and dolomite is problematic because of the calcium released by dissolution.

## 2.4.2 Transition Metal Catalysts

Fourth and fifth period transition metals have demonstrated the ability to catalyze a wide array of reactions. Transition metals have a long history of use as catalysts. Over the past five decades transition metal catalysts (TMCs) have been used to promote partial oxidation of ethane/methane<sup>74</sup>, and hydrogenation of fatty acids<sup>75</sup> to current novel research utilizing transition metals to promote the degradation of wastewater organics<sup>76</sup>, and the reduction of CO<sub>2</sub> to CO<sup>77</sup>. For their use in promoting the thermochemical conversion of lignocellulosic biomass, TMCs have recently been used to generate specific functional groups, including carboxylic acids, esters<sup>78</sup> and ketones<sup>79</sup>, and are used to synthesize small aromatic heterocycles<sup>80</sup>. Additionally, TMCs have been used to computationally model decomposition reactions of biomass on metal surfaces using density functional theory (DFT)<sup>81</sup>.

The current use of transition metals remains limited in scope. Wang et al. used zirconium and nickel (among others) in the catalytic cracking of oleic acid, a fatty acid found in vegetable and animal fats and oils, into liquid hydrocarbon fuels<sup>82</sup>. While the use of transition metals decreased the overall bio-

**Table 2.6** Transition metals for use as catalysts

Transition Metal	Oxidation States
Chromium	+2, +3, +6
Cobalt	+2, +3
Copper	+1, +2
Iron	+2, +3
Manganese	+2, +3, +4, +7
Nickel	+2, +3
Palladium	+2, +4
Zinc	+2
Zirconium	+3

oil yield, there was a sharp increase in the aromatics and alkanes produced. Furthermore, on a per gram oil yield basis, the catalyst-derived bio-oils showed higher calorific values, lower acid contents, and lower oxygen in the bio-oils. While the use of transition metals successfully improved the bio-oil, this case remains limited in scope to oleic acid as the feedstock. Understanding how oleic acid affects the thermal decomposition of a mixed biomass feedstock, or how any constituent material affects the overall biomass blend, is fundamentally critical.

The range of applications of transition metal catalysts in promoting or altering hydrocarbon chemistry is extensive, however the mechanisms at play are poorly understood, and therefore are not widely adapted to highly complex systems such as thermochemical conversion of heterogeneous biomass. This work explores the use of the transition metals outlined in Table 2.6 and have been selected due to varying levels of availability and expense, as well as an initial deterministic comparison of the metal's effects on select decomposition reactions.

## 2.5 Scope of Work

While substantial work in the literature has identified and solved many of the problems associated with catalytic upgrading of pyrolysis bio-oils, several key concepts remain elusive which are addressed in this work.

The primary goal of this research is to demonstrate the viability of inexpensive catalysts to promote higher quality bio-oil formation by reducing tars. These tar compounds are acidic, contribute to viscosity, and have lower energy density. The central causes to these problems are both the physical size of the tar compounds, and their oxygen content. By using catalysts to promote cracking, we demonstrate the generation of a higher-quality bio-oil is possible, without the addition of costly and complex downstream processes. This work uses both clay minerals and pure transition metals as catalysts unique in this application and separates the effects of these catalysts on primary and secondary pyrolysis.

Additionally, the behavior of lignocellulosic feedstocks is largely unpredictable. A large portion of the literature is dedicated to pure biomass components (such as cellulose, xylan, or pectin), and the interaction between these components has been largely unexplored. This work demonstrates the importance of biopolymer interaction by proving the synergistic effects between these compounds can drastically alter the devolatilization behavior of the biomass and highlights how these interactions can be exploited to select for bio-oil furans or phenols or generate larger quantities of hydrogen.

### **Chapter 3: Synergistic Behavior Among Biomass Biopolymers**

Lignocellulosic plant matter is primarily comprised of polysaccharides and polyphenols of three major component classes: cellulose, hemicellulose, and lignin. While the pyrolysis of each of these constituents individually is well studied<sup>83-86</sup>, the behavior of individual components is not necessarily an accurate representation of how the biomass behaves as a whole during pyrolysis. As such, we must understand to what extent biomass building blocks interact during pyrolysis to promote or suppress product formation. This will allow for better selection of biomass feedstocks and blends to enable upstream tuning of downstream products formed. Each of these polysaccharides devolatilizes at different temperatures owing to their varying compositions, structures, and degree of polymerization, and each produces different products upon pyrolysis. Understanding how these constituents interact during pyrolysis, and to what degree they promote or inhibit devolatilization, is key to understanding what products can be expected from different feedstocks. If these components do not interact, the products would simply be a summation of their individual parts. Interaction between polysaccharides could promote favorable compound formation, or aid in the reduction of non-desirable tar or heavily oxygenated compounds.

Previous studies indicate that blends of cellulose, hemicellulose, and lignin show both additive and non-additive (synergistic) behavior<sup>87,88</sup>. Additive blends are those where the components devolatilize according to their individual behavior, such that their kinetics can be described as the weighted sum of the mixtures' parts, and the products evolved are similarly a weighted average. Much like an ideal gas mixture, an additive blend is one where the individual components do not "see" each other, and therefore do not interact. In non-additive (synergistic) reactions, one species assists another in devolatilizing, often at lower temperatures than individual components, or

prevents the devolatilization of the other. Devolatilization can be hampered either via direct inhibition of the process, or an antagonistic effect. Xue *et al.* pyrolyzed cellulose and starch up to 900°C to observe changes in mass loss regimes and activation energy<sup>89</sup>. Cellulose and starch have identical monomers but differ in linkage types in the polymer structure ( $\beta$ -aryl ether vs.  $\beta$ -O-4). Even this minor difference in linkage type among otherwise identical biomasses revealed non-additive behavior: mixtures with at least 50% starch content promoted cellulose devolatilization at lower temperatures. This non-additive behavior is a promising indication of synergistic interaction where a component devolatilizing at lower temperatures can effectively catalyze compounds typically devolatilizing at higher temperatures. Understanding how the relative composition of incoming feedstock affects the products is a critical step in redesigning the biorefinery.

Liu *et al.* blended cellulose, hemicellulose (xylan), and lignin in various quantities and pyrolyzed said mixtures up to 800°C<sup>90</sup>. An analysis in changes of derivative thermogravimetric (DTG) curves yields experimental mass loss peaks which differ from the experimental additive scheme. The constituents – in the presence of one another – changed the bulk mixture behavior and either raised (cellulose and hemicellulose) or lowered (hemicellulose and lignin) the peak reaction temperature. Lowering peak reaction temperature through biomass blending could reduce the economic barriers to biomass pyrolysis at an industrial scale by reducing energy input. Such blending can also be used to tune downstream product distribution; for example, in Liu *et al.*'s work, hemicellulose and lignin containing mixtures showed lower furfural yield and fewer C=O containing functional groups such as ketones and aldehydes in the pyrolysis bio-oil than cellulose containing mixtures. However, Liu *et al.* do not report pyrolysis results for lignin individually in this work. Without a pure lignin baseline, it is difficult to quantify synergistic reactions. The near-linear decrease in

functional groups could be attributed directly to the decreased quantity of hemicellulose and not any interaction<sup>90</sup>.

In contrast, Chen and Kuo torrefied cellulose, hemicellulose, and lignin blends up to 300°C, with little evidence of synergistic effects. The mass loss regimes observed indicated that the combined effects are solely additive, and that little or no promotion of devolatilization exists across species<sup>91</sup>. It is likely that the low-temperature range over which torrefaction occurs does not produce synergistic effects, as lignin is only in the initial stages of decomposition and cellulose has just begun ring-opening and levoglucosan production.

Many studies utilize DTG curves to represent total devolatilization reactivity. While DTG is informative of the degree of synergistic effects related to mass loss rates and peak temperatures (indicative of overall reaction kinetics<sup>92</sup>), it does not ultimately reveal the effect on the biochar, bio-oil, and gas products formed during pyrolysis, which is at the heart of feedstock decision-making. To complement DTG analysis, we can use gas chromatography-mass spectroscopy (GC-MS) to identify major bio-oil components, and residual gas analysis (RGA) via mass spectroscopy to identify the non-condensable gas formed during pyrolysis in real-time. This chapter explores the potential synergistic effects between cellulose, xylan (hemicellulose polymer), xylose (hemicellulose monomer), and lignin to enable an improved understanding of how biomasses behave during pyrolysis and the potential to tune the quantity and quality of pyrolysis products based on feedstock composition.

### 3.1 Materials and Methods

Four individual biomass constituents: cellulose (MP Biomedicals microcrystalline cellulose powder, minimum 97% pure, 162.14 g/mol), xylan (TCI xylan from corn core, minimum 95%

**Table 3.1** Biomass constituent mixtures

Mixture	Cellulose (wt %)	Xylose (wt %)	Xylan (wt %)	Lignin (wt %)
1	50	---	---	50
2	50	---	50	---
3	50	50	---	---
4	---	50	---	50
5	---	50	50	---
6	---	---	50	50
7	33	---	33	33
8	33	33	---	33

pure), xylose (Alfa Aesar D-(+)-xylose, >99% pure, 150.13 g/mol), lignin (Sigma Aldrich low sulfonate content alkali lignin, density 1.3g/mL) were used (as received) individually, and as mixtures in the weight ratios given in Table 3.1. Mixtures were fabricated by weighing the individual components to the 0.1 mg on a Shimadzu Analytical Balance directly into a clean glass vial and vortex mixing to ensure homogeneity.

#### 3.1.1 Generation of Pyrolysis Bio-oil

Approximately 2.5 grams of each sample was weighed into a porcelain combustion boat and inserted into a 2-inch diameter quartz tube furnace (MTI single heating zone GSL-1100X). A nitrogen gas generator (Parker Balston Model N2-04) supplied the inert atmosphere necessary for pyrolysis, with an Omega mass flow controller (FMA-5500) delivering 100 mL/min of N<sub>2</sub> (<0.1% O<sub>2</sub>). We purged the tube furnace and subsequent cold traps for 10 minutes before heating began to ensure an inert atmosphere. The furnace temperature was ramped at 10°C/min from ambient to 110°C and held for 30 minutes remove residual moisture. The temperature was then raised to

600°C at 10°C/min and held for 60 minutes, at which point the furnace was allowed to cool to 80°C under N<sub>2</sub> to ensure no oxygen infiltration into the system. 600°C was selected as the pyrolysis temperature due to the large body of existing literature at this condition, and the high degree of biomass conversion<sup>93–95</sup>. The biochar sample was weighed to determine the mass fraction of char recovered (solid yield).

The setup downstream of the tube furnace, illustrated by Figure 3.1, includes a set of four glass cold traps (to collect condensable bio-oils), the capillary for the residual gas analyzer (RGA, to analyze non-condensable gases), and finally a water trap after which the residual pyrolysis gas was vented into a fume hood (not shown). Transfer lines from the furnace to the cold traps were maintained at 250°C using heating tape, (Omega model FGH101-040L; Staco Energy variable transformer model 3PN1010B) to prevent bio-oil condensation in the lines to the cold traps (not shown). The cold traps were suspended in vacuum flasks surrounded by a dry ice and glycol mixture. The first two cold traps in series condensed all of the bio-oil; the second two traps served as additional protection for the RGA (Extorr XT300M with Pfeiffer HiCube 80 Eco Vacuum). The RGA analyzed the non-condensable gases in real time via a 40µm inner diameter silica glass capillary. Mass to charge (m/z) ratios for four gases were monitored: hydrogen (m/z = 2), methane

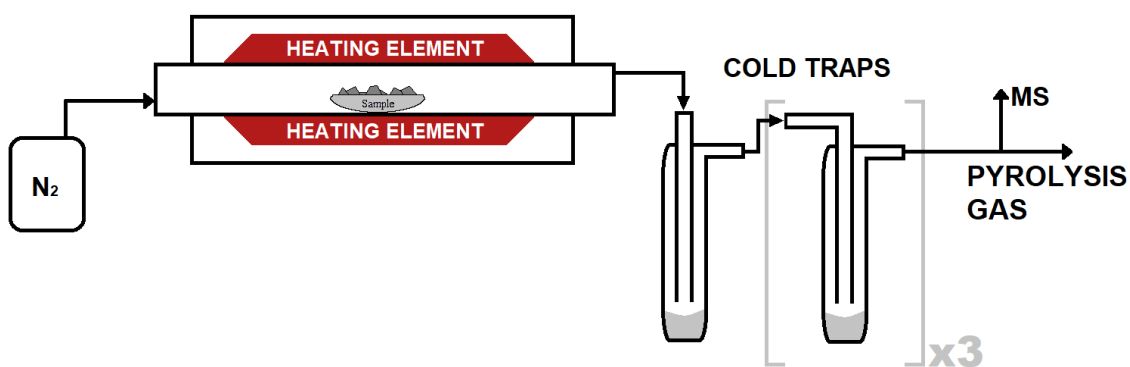


**Figure 3.1** Pyrolysis tube furnace setup

( $m/z = 15$ ), ethane ( $m/z = 27$ ), and carbon dioxide ( $m/z = 44$ ). Due to the overlap of spectra peaks, secondary peaks for methane ( $m/z=15$ ) and ethane ( $m/z=27$ ) are used in this analysis<sup>96</sup>.

### **3.1.2 Characterization of Bio-oil via Gas Chromatography and Mass Spectroscopy**

The glass cold traps used for bio-oil collection were weighed at the beginning of the experiment, after bio-oil collection, and after bio-oil extraction. The difference in weight between collection and baseline represents the bio-oil generated (including the aqueous phase), and the difference between extraction and collection determines the amount of recoverable bio-oil. To extract the bio-oil, 5 mL of dichloromethane (DCM) was added to the second cold trap and used to rinse the glassware of as much bio-oil as possible. This DCM and bio-oil solution was transferred to the first cold trap, and another 5 mL DCM was used to rinse the first trap. The resulting mixture contained 10 mL DCM and a known quantity of bio-oil weight (by difference).

Before analyzing the bio-oil, the water produced during pyrolysis was removed by drying 1mL of dissolved oil over approximately 0.1 g of anhydrous magnesium sulfate (AMS) (Fisher Scientific) in a 1.5 mL polypropylene centrifuge tube. The empty centrifuge tube weight, and weight with AMS were both recorded. The centrifuge tube was filled with the (DCM + bio-oil) solution to a total volume of approximately 1.2 mL. The total weight was recorded. The tube was shaken by hand for approximately four minutes, then centrifuged for two minutes. Any water previously in the oil, now bound to the AMS, was separated to the bottom of the centrifuge tube. Water generated during these experiments was less than 1% of the pyrolysis bio-oil, by weight. The bio-oil was pipetted out and placed into a new centrifuge tube for storage (weighed before and after). The old centrifuge tube with the remaining AMS and water was weighed immediately, and represented the

mass of the tube, hydrated AMS, and residual organics. The tube was left uncapped in the fume hood for several days to evaporate any residual bio-oil and DCM, over which time it was weighed 2-3 more times until the weight stabilized to determine an approximate bio-oil water content.

The dried bio-oil was analyzed via gas chromatography-mass spectroscopy (GC-MS, Shimadzu GCMS-QP2020 with AOC-20s Autosampler). 0.2 mL of the dehydrated bio-oil was diluted with 0.5 mL DCM prior to injection. The oven temperature was set to 40°C, and the sample was injected at 250°C onto a Shimadzu Crossbond 30m long, 0.25 mm ID column, with a flow of 1 mL/min helium and a split ratio of 15:1. The oven was held at 40°C for 5 minutes before ramping at 5°C/min to 150°C and holding for 5 minutes. The oven was ramped again at 1.75°C/min to 250°C and held for 10 minutes. Interface and ion source temperatures were 250°C and 230°C respectively. A solvent cut time of 6 minutes was set on the mass spectrometer, after which time it was run in scan mode from 15 to 400 m/z using electron ionization. Peaks with slopes  $\geq 1500$ , and durations  $\geq 2$  seconds on the resulting chromatogram were isolated and analyzed. Compounds were identified by spectra through the internal NIST library and a series of marker compounds were confirmed with calibration solutions.

### **3.1.3 Thermal Analysis of Biomass Pyrolysis**

In addition to pyrolyzing samples in the tube furnace, approximately 10 mg of each biomass (pure compounds and mixtures) was analyzed on a TA Instruments Discovery series 650 thermogravimetric analyzer (TGA). The same run was used for proximate analysis and to construct pyrolysis derivative thermogravimetric (DTG) curves. In step 1 of the TGA run, samples were heated under nitrogen to 110°C and held for 30 minutes to drive off moisture. In step 2, samples

were pyrolyzed by heating to 900°C at a rate of 10°C/min and held for 60 minutes at 900°C. This pyrolysis step represents the mass loss of volatile matter, and the mass at the end of this step was used to calculate the DTG curves. Following this step, samples were exposed to dry air and heated to 950°C and held for an additional 15 minutes (mass loss attributed to fixed carbon; residual inorganic mass is loosely termed “ash”). During the TGA run, the mass of the sample is collected every 0.5 seconds, which allows for the construction of a derivative thermogravimetric (DTG) curve showing the mass loss profile of the sample, and the temperature range where the majority of the volatile matter is lost, as well as providing information for a proximate analysis. The mass loss converted at any time  $t$ ,  $X(t)$ , during the pyrolysis step was determined via Equation 3.1:

$$X(t) = \frac{m_{dry} - m_t}{m_{dry} - m_{pyr}} \quad (3.1)$$

Where  $m_{dry}$  is the mass after the sample is held at 110°C (at the start of pyrolysis),  $m_t$  is the mass at any time,  $t$ , during the pyrolysis TGA step, and  $m_{pyr}$  is the residual mass left at the end of the 60 minute pyrolysis at 900°C. DTG curves were constructed by plotting  $dX/dt$  versus temperature.

## 3.2 Results and Discussion

Proximate analysis for the individual and mixed biomasses are presented in Table 3.2. Since all biomass components were purchased at high purity, as expected negligible ash was observed.

Lignin and lignin containing mixtures presented higher fractions of fixed carbon.

**Table 3.2** Proximate analysis of individual components and their mixtures ( $\pm$  one standard deviation)

Pyrolysis Feedstock (Mixtures are equal mass)	Volatile Matter (wt % dry basis)	Fixed Carbon (wt % dry basis)
Cellulose	97.4 $\pm$ 1.3	2.6 $\pm$ 1.3
Xylan	56.8 $\pm$ 4.9	43.2 $\pm$ 4.9
Xylose	82.7 $\pm$ 1.5	17.3 $\pm$ 1.5
Lignin	82.1 $\pm$ 3.2	17.9 $\pm$ 3.2
Cellulose + Lignin	70.5 $\pm$ 2.2	29.5 $\pm$ 2.2
Cellulose + Xylan	86.7 $\pm$ 2.0	13.3 $\pm$ 2.0
Cellulose + Xylose	90.0 $\pm$ 1.9	10.0 $\pm$ 1.9
Xylose + Xylan	80.4 $\pm$ 2.1	19.6 $\pm$ 2.1
Lignin + Xylan	64.9 $\pm$ 0.2	35.1 $\pm$ 0.2
Lignin + Xylose	63.8 $\pm$ 3.5	36.2 $\pm$ 3.5
Cellulose + Xylan + Lignin	68.5 $\pm$ 0.2	31.5 $\pm$ 0.2
Cellulose + Xylose + Lignin	69.1 $\pm$ 1.8	30.9 $\pm$ 1.8

### 3.2.1 Thermogravimetric Analysis

Representative derivative thermogravimetric (DTG) curves for five mixtures and the individual polysaccharides are plotted in Figure 3.2 (additional DTG curves available in Appendix A). Each of the five mixtures are compared directly to a predicted outcome (labeled as *expected*). To predict the expected (additive or non-synergistic) behavior, individual properties were weighted by mass fraction and the weighted fractions added together. Equation 3.2 depicts the general formula where  $P_{expected}$  is the property of interest of the mixture (e.g. amount of hydrogen formed, mass loss rate, furans produced, etc.),  $x_i$  is the mass fraction of each polysaccharide in a mixture,

$$P_{expected} = \sum_{i=1}^n x_i P_i \quad (3.2)$$

according to Table 3.1, and  $P_i$  is the quantity that results from pyrolysis of the individual component.

If two biomasses are co-pyrolyzed and do not interact, then the outcomes – in either gas evolution, bio-oil formation, or mass loss rates – should be an additive (non-synergistic) function of each pure component's contribution to the mixture. If the two biomasses interact by promoting or suppressing devolatilization, then the DTG curves will diverge. In Figure 3.2, the combination of cellulose and lignin resulted in a depressed peak mass loss rate, and a slight shift to a higher temperature. In the cellulose-lignin case, the mass remaining after pyrolysis is close to the prediction. The cellulose and xylan mixture exhibits similar behavior to the predicted case, however with a slightly increased peak mass loss rate. The increase in the peak mass loss rate at elevated temperatures translates to a reduction in the effectiveness of pyrolysis at lower temperatures for this mixture. Cellulose is the likely driver for this, as it overpowers the xylan which tends to devolatilize at lower temperatures. The decrease in low temperature devolatilization hints at an overall reduction in mass loss, resulting in greater solid biochar yield.

Additionally, Figure 3.2 shows cellulose devolatilizing in a single large peak, whereas xylan, xylose, and lignin undergo a longer, multi-step pyrolysis. Of the compounds analyzed in this work, cellulose is the simplest and most uniform in its construction. Single chains of glucose monomers behave uniformly when evenly heated, depolymerizing and devolatilizing together within a small temperature window<sup>97,98</sup>. In contrast, lignin is highly polymerized with a variable structure. Some

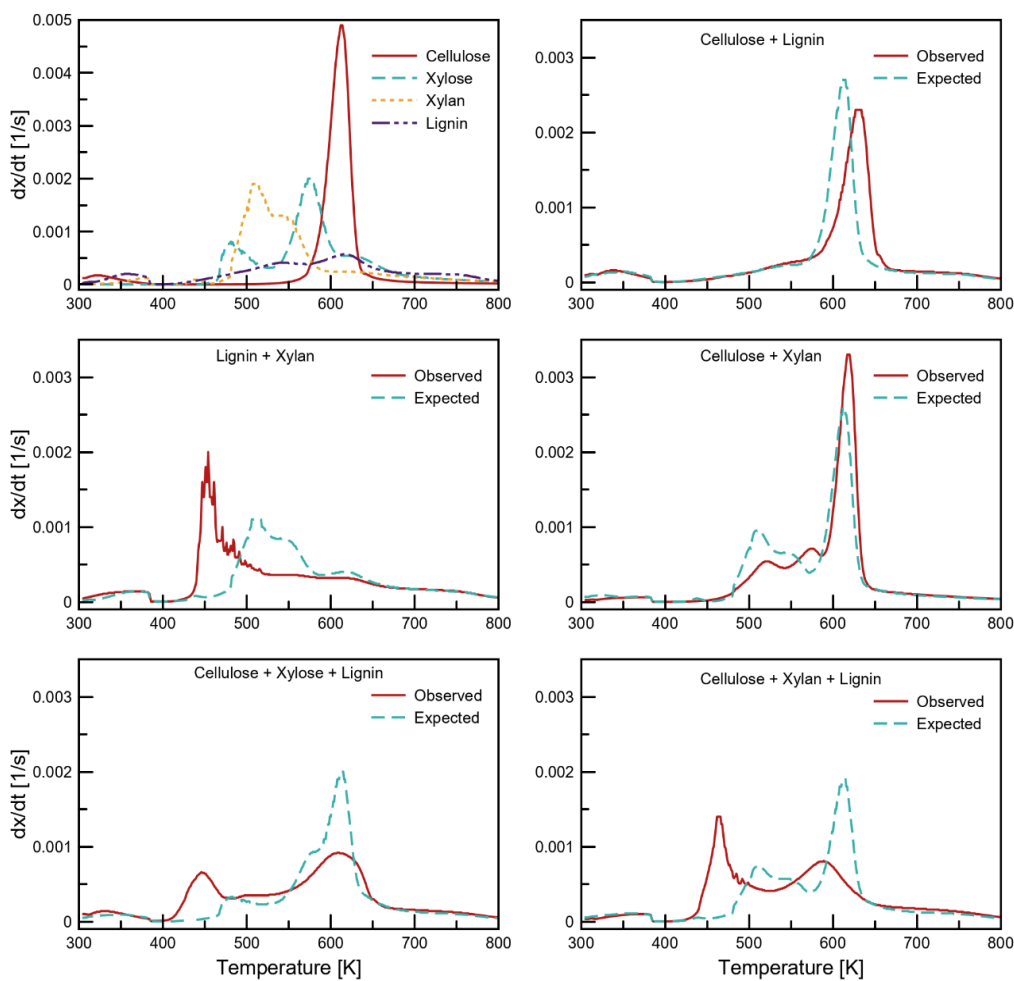


**Figure 3.2** Representative derivative thermogravimetric mass loss curves of polysaccharide mixtures showing observed data versus expected mixture behavior as calculated via Eqn. 3.2

components of lignin may begin to pyrolyze at relatively low temperatures, while others are only affected at high temperature. This variability gives a much longer devolatilization time, and spreads the mass loss over a wider temperature range<sup>26,99</sup>. Hemicelluloses, such as xylan, behave somewhere in the middle of cellulose and lignin. Hemicelluloses tend to have long single-chain backbones like cellulose, but contain branching structures like lignin. These branched structures undergo scission and are removed from the backbone (completely or in part) where they break down and behave differently<sup>26,100</sup>. Xylose, as a monomer, would be expected to devolatilize in a manner similar to cellulose. However, the dual-peak nature of xylose may be indicative of several

mechanisms. Huang et al. proposed several reaction pathways for the breakdown of xylose. These independent peaks could be competing dominant parallel pathways, or a delay in a single pathway – where the reaction is carried partway, but requires sufficiently high temperatures for the next steps, resulting in a lag in the volatilization behavior<sup>101</sup>.

The largest differences between expected and observed thermal behavior are seen in the lignin and xylan containing mixtures in Figure 3.3. The peak mass loss rate for the lignin and xylan mixture increases considerably at lower temperatures compared to the predicted profile. In addition, each cellulose containing mixture saw a drop in biochar yield compared to the expected as seen in Table 3.3. This drop indicates more biomass was converted into oil and gas. Lignin/hemicellulose mixtures generated 12-19% more biochar than expected. The increased devolatilization indicates synergistic effects between the two compounds. The total mass loss is governed by the area under the DTG curve, and normalized to the mass of the sample; this total area is equal to 1. A shift in the peak from right to left (or the more area at the lower end of the spectrum) equates to increased conversion at lower temperatures, improving the energy efficiency of the conversion process.

Mixtures containing xylan (or xylose) with lignin had significant reductions in the peak temperature, and saw concentrated devolatilization over narrower temperature ranges. Lignin and hemicellulose individually devolatilize over a wider thermal

**Table 3.3** Actual and expected biochar yields

	<b>Actual Biochar (wt%)</b>	<b>Expected Biochar (wt%)</b>	<b>Percent Change (%)</b>
Cellulose	17.82	--	--
Xylan	18.89	--	--
Xylose	17.90	--	--
Lignin	58.40	--	--
Cellulose + Lignin	38.50	38.11	-1.01
Cellulose + Xylan	19.77	18.36	-7.16
Cellulose + Xylose	20.16	17.86	-11.41
Xylose + Xylan	34.31	38.65	12.63
Lignin + Xylan	33.83	38.15	12.77
Lignin + Xylose	15.45	18.40	19.06
Cellulose + Xylan + Lignin	33.26	31.70	-4.69
Cellulose + Xylose + Lignin	34.47	31.37	-8.99

range than cellulose, however when lignin and hemicellulose are mixed, their devolatilization becomes concentrated at low temperatures. In contrast, cellulose containing mixtures either raised the peak temperature, or suppressed devolatilization at lower temperatures. Cellulose devolatilizes over a narrow and elevated temperature range and tends to dominate when mixed with one other biomass. However, mixtures containing all three biomass types benefitted from devolatilization at lower temperatures. When cellulose is mixed with two biomasses, its effects are suppressed.

### 3.2.2 Analysis of Non-Condensable Gases

Non-condensable gases offer insight into the pyrolytic devolatilization pathways. Figure 3.3 displays the evolution of the pyrolysis gas from all four individual biomasses and highlights the outlier: lignin. Lignin is composed of approximately 4.9% hydrogen by weight<sup>102</sup>, whereas cellulose, xylose, and xylan have 6.2 wt%, 6.0 wt%, and 5.3 wt% respectively. While all four raw

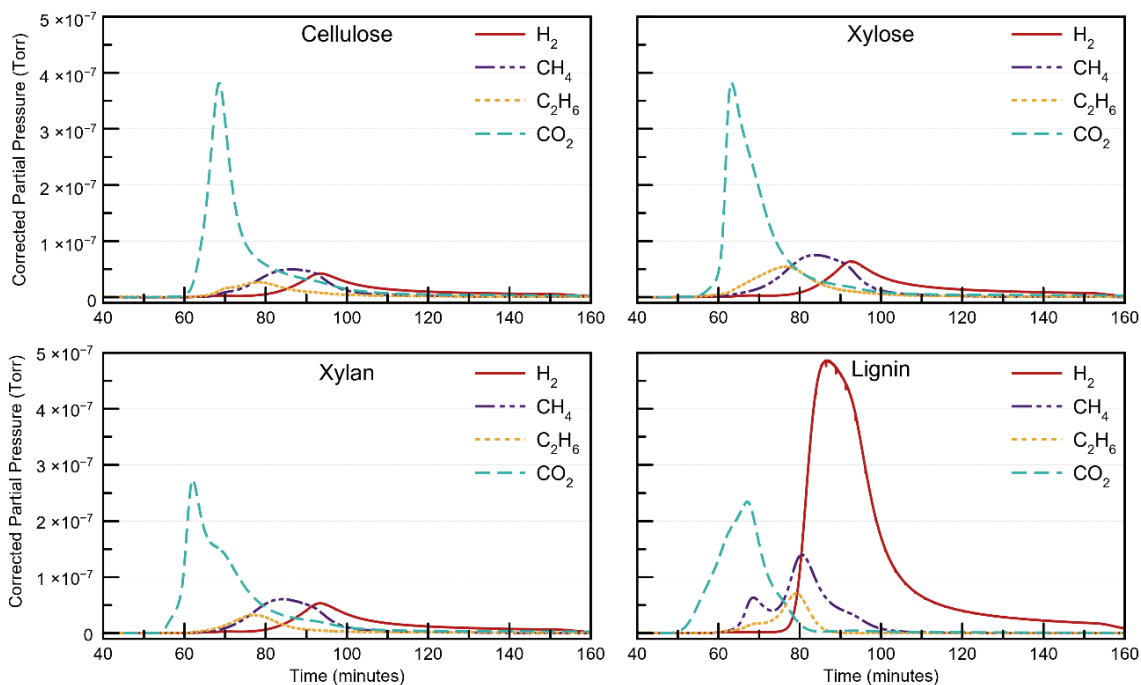


**Figure 3.3** Pyrolysis gas evolution for individual biomass constituent compounds

polysaccharides contain roughly similar amounts of hydrogen, lignin produces nearly ten times the amount of hydrogen gas, seen in Table 3.4.

**Table 3.4** Non-Condensable gas evolution of pure biopolymers

	Partial Pressure (Torr)			
	H <sub>2</sub>	CH <sub>4</sub>	C <sub>2</sub> H <sub>6</sub>	CO <sub>2</sub>
<b>Cellulose</b>	1.1E-06	1.1E-06	6.0E-07	3.9E-06
<b>Xylose</b>	1.6E-06	1.7E-06	1.1E-06	4.4E-06
<b>Xylan</b>	1.4E-06	1.3E-06	6.1E-07	3.7E-06
<b>Lignin</b>	1.0E-05	2.1E-06	7.3E-07	3.4E-06

This presents a potential for greater errant functional groups, which when further reacted are a source of hydrogen gas<sup>103,104</sup>. The greater removal of hydrogen leads to more C-C and C-O bond preservation/formation, favoring biochar over liquid bio-oil generation. All samples produce similar quantities of carbon dioxide over the reaction time, seen in Table 3.3 (peak temperature of 600°C is reached at 90 minutes), and the peak evolution for each of the four gases occurs at approximately the same time. Carbon dioxide is driven from the samples before the bulk of hydrogen gas is released/formed, and methane is largely formed before ethane during cellulose, xylose, and xylan pyrolysis although in lower amounts.

Four gases (hydrogen, carbon dioxide, methane, and ethane) were tracked for all 8 mixtures. Gas generation increased above the expected values in 31 of 32 cases, seen in Table 3.5. The percent increase of each gas over the expected value is given by equation 3.3.

$$Percent\ Increase = \frac{Gas_{observed} - Gas_{expected}}{Gas_{expected}} \times 100\% \quad (3.3)$$

Independent of the type of polysaccharides co-pyrolyzed, increased gas generation is a strong indicator of enhanced devolatilization and minimized (re)condensation of devolatilized compounds. Therefore, pure biomass constituents produce larger amounts of condensed phases (biochar and bio-oil) fractions than mixtures, which favor non-condensable gas formation.

**Table 3.5** Percent difference between observed and expected gas evolution via eqn. 3.3, positive values indicate synergistic (non-additive) behavior with enhanced gas evolution

<b>Pyrolysis Feedstock (Mixtures are equal mass)</b>	<b>Hydrogen (%)</b>	<b>Methane (%)</b>	<b>Ethane (%)</b>	<b>Carbon Dioxide (%)</b>
<b>Cellulose + Lignin</b>	58	24	90	55
<b>Cellulose + Xylan</b>	55	39	38	42
<b>Cellulose + Xylose</b>	26	18	8	16
<b>Lignin + Xylan</b>	71	32	101	80
<b>Lignin + Xylose</b>	68	22	35	66
<b>Xylan + Xylose</b>	15	5	-21	13
<b>Cellulose + Xylan + Lignin</b>	101	40	126	75
<b>Cellulose + Xylose + Lignin</b>	103	38	73	67

Only ethane production in the xylan + xylose scenario produced less than expected amount of any gas (in this case ethane), where the xylan and xylose mixture otherwise remained close to all the predictions. Since these are the monomer and polymer form of the same sugar, this is likely due to the xylan readily depolymerizing into xylose, generating a rather homogeneous mixture without much opportunity for synergism to occur.

The cellulose + xylose mixture generated the second-lowest increase in non-condensable gases over the expected value. Xylose (already in monomer form) and cellulose (which depolymerizes at relatively low temperatures likely again form a somewhat homogenous mixture, whereby their rapidly released gases escape the matrix with little time for heterogeneous reactions. A subset of the gas evolution can be seen in Figure 3.4. The presence of lignin in a mixture drives peak mass loss to lower temperatures and increases the overall hydrogen generation. This suggests that lignin-containing mixtures are desirable for applications where high biochar or high non-condensable gas yields are desirable, such as solids for soil amendments<sup>105</sup> or hydrogen gas for ammonia production<sup>106</sup>. However, the gas evolution in lignin-containing mixtures does not follow the expected additive prediction. Significant increases in both carbon dioxide and hydrogen gas

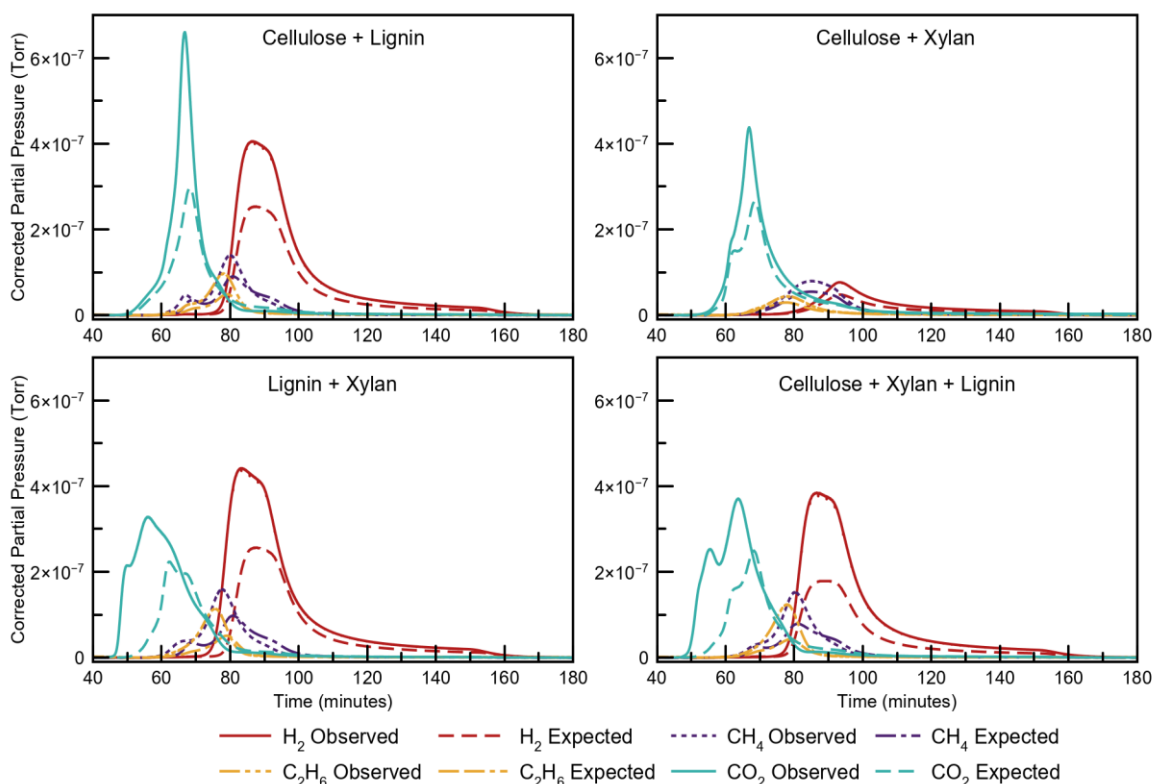


**Figure 3.4** Pyrolysis gas evolution for selected biomass mixtures (additional combinations available in Appendix A)

production across all lignin-containing mixtures indicate that the presence of lignin spurs devolatilization and potentially breaks the lignocellulosic components into smaller non-condensable compounds.

### 3.2.3 Bio-oil Analysis

The bio-oil results were normalized to the amount of raw biomass loaded in the pyrolysis boats. To enable a comparative analysis between all three outputs (biochar, bio-oil, and pyrolysis gas), decreases or increases in yield are important in determining how the other product yields should respond. All biomasses were analyzed individually – seen in Figure 3.5 – and used to develop

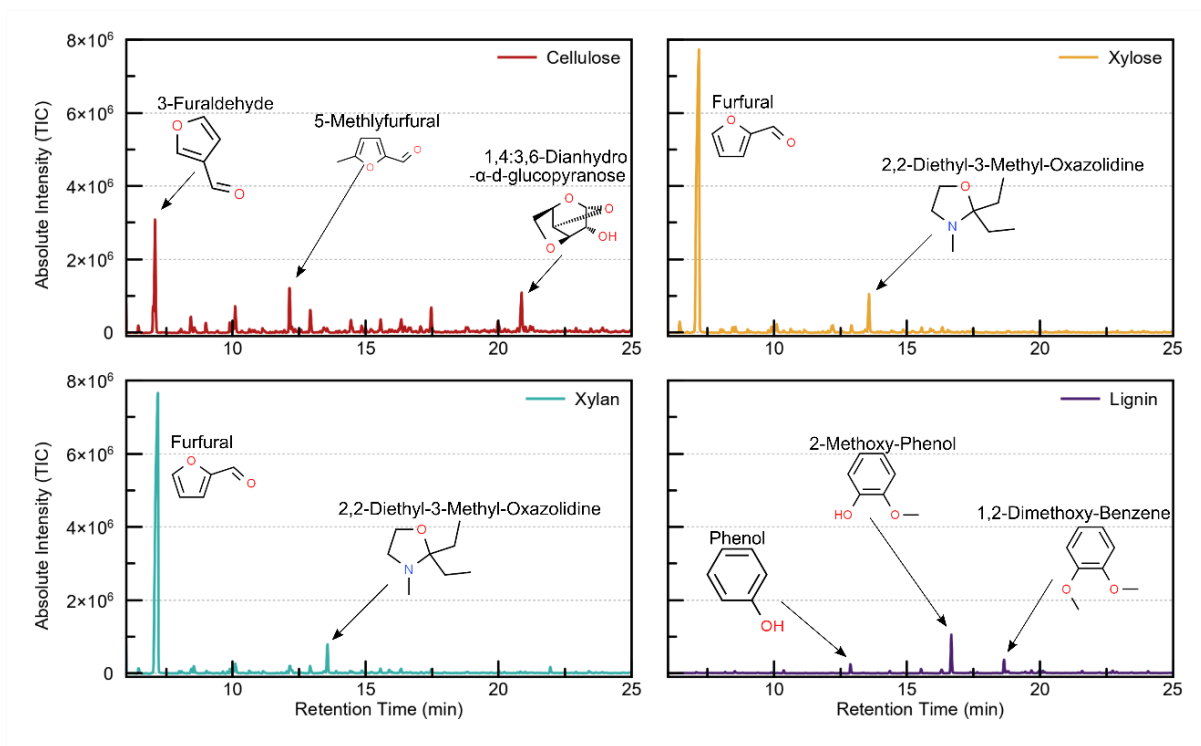


**Figure 3.5** GC Chromatograms of bio-oil for individual biomasses

expected chromatograms based on relative concentrations of the most abundant compounds of the mixtures outlined in Table 3.1.

Lignin – having the least amount of volatile matter with a complex long-range structure – produced the least amount of bio-oil as seen in Table 3.6. The lignin-derived oil contained more phenolic compounds, which agrees with the literature<sup>107</sup>. Given the high content of C6s in lignin's structure, the decomposition favored ethyl group cleavage. Xylose and xylan are known to produce high concentrations of furfural<sup>43,108</sup>, which is confirmed by this work. Xylose, xylan, and cellulose individually produced similar amounts of oil in this study (outlined in Table 3.6). Cellulose

**Table 3.6** Bio-oil yield for pure components and mixtures with estimated furan and phenol concentrations

	Oil Yield (wt %)	Oil Expected (wt %)	Percent Change (%)		Actual ( $\mu\text{g/mL}$ )	Expected ( $\mu\text{g/mL}$ )	Percent Change (%)
Cellulose	53.1	---	---	Furans	35,504	---	---
				Phenols	26,109	---	---
Xylose	55.7	---	---	Furans	86,321	---	---
				Phenols	2,726	---	---
Xylan	51.8	---	---	Furans	96,919	---	---
				Phenols	3,267	---	---
Lignin	23.3	---	---	Furans	264	---	---
				Phenols	69,997	---	---
Cellulose + Lignin	33.1	37.9	-12.6	Furans	20,791	27,625	<b>-24.7</b>
				Phenols	50,068	29,974	<b>67.0</b>
Cellulose + Xylose	50.4	54.2	-7.0	Furans	51,890	64,881	<b>-20.0</b>
				Phenols	5,630	6,473	<b>-13.0</b>
Cellulose + Xylan	52.1	53.5	-2.7	Furans	65,206	102,206	<b>-36.6</b>
				Phenols	6,593	6,482	<b>1.7</b>
Lignin + Xylose	34.4	39.4	-12.7	Furans	7,323	64,580	<b>-88.7</b>
				Phenols	41,578	13,856	<b>200.1</b>
Lignin + Xylan	37.2	37.4	-0.5	Furans	4,068	51,517	<b>-92.1</b>
				Phenols	28,915	13,508	<b>114.1</b>
Xylose + Xylan	53.6	53.6	0	Furans	91,908	85,486	<b>7.5</b>
				Phenols	8,078	4,216	<b>91.6</b>
Cellulose + Xylose + Lignin	35.6	43.9	-18.9	Furans	13,241	54,273	<b>-75.6</b>
				Phenols	31,768	17,191	<b>84.8</b>
Cellulose + Xylan + Lignin	38.8	42.5	-8.8	Furans	16,706	62,485	<b>-73.7</b>
				Phenols	52,431	17,569	<b>198.4</b>

produces the widest array of compounds and is responsible for most of the higher molecular weight compounds which elute beyond a retention time of 20 minutes.

Figure 3.6 highlights the top ten chromatogram peaks for the cellulose and lignin mixture, and compares them to the expected (additive, non-synergistic) behavior. (Additional chromatograms

available in Appendix A) The dashed lines in Figure 3.6 (referred to as zones) group similar compounds based on retention time. Zone one predicted a significant generation of 3-furaldehyde due to the cellulose. However, the cellulose-lignin mixture formed cyclopentenone in addition to 3-furaldehyde, which had not been present in either the cellulose or lignin cases individually. Additionally, the amount of generated 3-furaldehyde and cyclopentenone combined is only half of the expected 3-furaldehyde amount – the formation of these smaller aromatics was suppressed by the presence of lignin. In contrast, zone 8 generated over 2.5 times the expected 2-methoxy-phenol. The interaction of cellulose and lignin produced more 2-methoxy-phenol than four times as much lignin would have produced on its own. Devolatilizing cellulose may re-condense on the lignin surface, forming tar compounds, and preventing the devolatilization of low molecular weight compounds. The increase in phenols potentially stems from cellulose increasing the scission of the oxygen linking individual monolignols, such as  $\beta$ -O-4 which composes more than half of all lignin

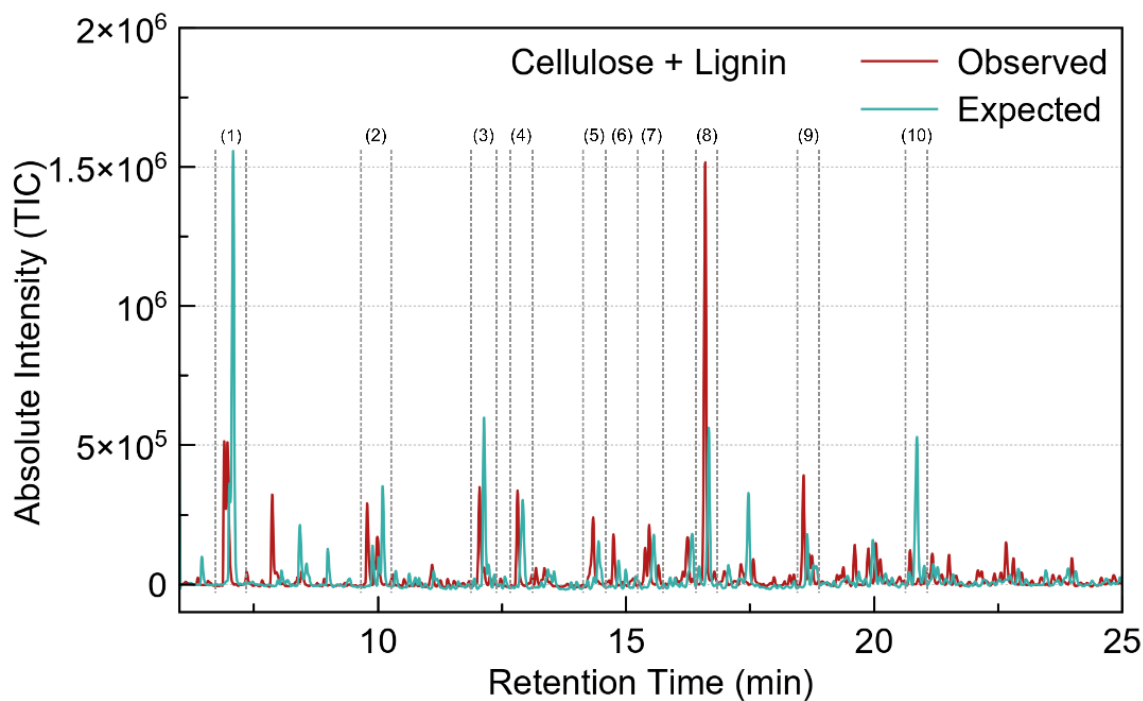


**Figure 3.6** Cellulose and lignin bio-oil chromatogram

linkage types<sup>50</sup>. Another significant improvement in the cellulose-lignin mixture was the suppression of the undesired tar compound 1,4:3,6-Dianhydro- $\alpha$ -d-glucopyranose (glucopyranose) in zone 10, which formed only 1/6 of the expected amount.

The most prevalent compounds were identified and semi-quantitatively analyzed. A 50% reduction in peak area translates to 50% lower yield. In all cases except xylose + xylan, total pyrolysis bio-oil yield was less than expected. This, in part, corresponds to the non-condensable gas increase seen for the mixtures, in which xylose + xylan was the only mixture to not see significant increases in overall gas production. The non-synergistic behavior of xylose + xylan is likely due to the mixture being the most homogenous.

Bio-oil compounds were split into two major category classes: furans and phenols. Lignin, being a strong phenol generator, led to greater-than-expected concentrations of phenols largely at the expense of furans (highlighted in red in Table 3.5). In all cases except xylose + xylan, furan production was depressed, potentially contributing to the overall decrease in bio-oil formation and increase in non-condensable gases. While the mechanism of increased phenol generation is not well understood, the mixture of compound classes does not appear to be promoting devolatilization at the expense of biochar formation. Table 3.6 highlights the biochar formation during each trial. Species containing cellulose resulted in an increase in biochar over their non-cellulose containing counterparts.

Overall, lignin-containing mixtures produce more non-condensable gases, more biochar, and less bio-oil than mixtures that do not contain lignin (seen in Table 3.7), suggesting that the increased phenols are not derived at the expense of the solid or gas phases but are a result of the depressed

**Table 3.7** Weight percent of biochar formed versus predicted from pyrolysis of pure polysaccharides and mixtures

	<b>Biochar Produced (wt %)</b>	<b>Biochar Expected (wt %)</b>	<b>Percent Change (%)</b>
Cellulose	17.8	---	---
Xylose	18.9	---	---
Xylan	17.9	---	---
Lignin	58.4	---	---
Cellulose + Lignin	38.5	37.9	1.5
Cellulose + Xylose	19.8	18.3	8.1
Cellulose + Xylan	20.2	18.2	10.6
Lignin + Xylose	34.3	38.5	-11.0
Lignin + Xylan	33.8	38.1	-11.1
Xylose + Xylan	15.5	18.3	-15.8
Cellulose + Xylose + Lignin	33.3	31.6	5.2
Cellulose + Xylan + Lignin	34.5	31.3	10.3

oil generated. The degree of changes to the biochar, bio-oil, and non-condensable gas yield and composition indicates synergistic (non-adaptive) behavior of the polysaccharides. Strong synergistic behavior was seen across polysaccharide classes, where the least synergistic behavior was observed in the mixture containing two forms of the same hemicellulose (xylose and xylan). Mixtures across classes (e.g. hemicellulose and lignin, or cellulose and lignin) promoted non-condensable gas generation and suppressed bio-oil formation. Selecting feedstocks high in lignin may help produce low quantities phenol-rich bio-oil. While lignin produces high amounts of biochar, mixtures containing cellulose produce more biochar than expected. Feedstocks selected to produce biochar soil for amendments benefit from a well-diversified feedstock, balancing the increased yield from lignin and increased synergy from cellulose.

### 3.3 Summary

The selection of biomass feedstocks for pyrolytic conversion to biobased fuels plays an important role in the composition of non-condensable gases, biochar, and bio-oil produced. To aid in the selection of biomasses to better target desired products, an understanding of the synergistic interactions between constituent polysaccharides is required. Biomass polysaccharides undergoing pyrolysis exhibit synergistic behavior, promoting non-condensable gas evolution and suppressing the formation of furans. Lignin-containing mixtures promote hydrogen gas formation, by potentially favoring C-C and C-O bonds to generate increased biochar over bio-oil yield. Additionally, lignin-containing mixtures promote phenols in bio-oil, likely formed through greater oxygen scission of the monolignol linkages. Cellulose-containing mixtures result in increased biochar yield possibly through condensation of tar compounds on the biochar surface. These findings suggest that cellulose, xylan, xylose, and lignin synergistically interact with each other, generating different concentrations of compounds than would be expected by a summation of their individual parts. However, this work is limited to examining the behavior of these constituent biopolymers as independent molecules, and not when linked together as is the case with real-world biomass. In nature, the cellulose, hemicelluloses, and lignin would all be interwoven and connected/bonded together, which would have further impact on the synergistic behavior. If possible, future studies should examine these biopolymers in their linked state, however in designing the experimental matrix, removing one biopolymer without altering the structure or linkage between the other two presents a challenge.

## Chapter 4: Transition Metals as *in situ* Catalysts for Cellulose

The renewable fuels literature is replete with explorations of pyrolysis bio-oil upgrading through chemical and thermal means, such as high pressure and catalytic transformations<sup>109–111</sup>. These catalysts are often used downstream in a fixed/fluidized bed over which products pass. For example, second-generation cellulosic biofuels, such as those from agricultural residues, are improved by nanoparticles such as ruthenium-based catalysts to increase yields of hexitol, sorbitol and isosorbide, and tungsten-based catalysts for improving ethylene glycol production, and metal formates to improve catechol<sup>112–115</sup>. When included during pyrolysis, catalysts have the ability to promote the devolatilization of biomass and help reduce larger compounds to smaller, more desirable ones<sup>116–119</sup>. Additionally, catalysts can lower reaction pathways' activation energy; reducing the energy demand for the conversion process helps make the system more energy efficient<sup>120</sup>. Among the array of potential catalysts, transition metals are attractive options as they are relatively inexpensive and useable in many forms when compared to other pre-formed catalysts<sup>121,122</sup>. When used *in situ*, rather than as a separate downstream upgrading step to improve products after formation, metal catalysts can steer product formation in real-time.

Previous experimentation with *in situ* transition metal catalysts utilized chromium(III) in a closed heated batch container to enhance the conversion of glucose to 5-Hydroxymethylfurfural (HMF)<sup>123</sup> – a desirable biorefinery feedstock, which can be readily converted into petrochemical end products<sup>45</sup>. Bali achieved HMF yields of over 70%. This high conversion rate was achieved through a mechanism whereby glucose coordinates to the active metal species – the chromium (III) – in the presence of 1-ethyl-3-methylimidazolium chloride ionic liquid. Glucose then undergoes mutarotation to the  $\beta$ -glucopyranose anomer, and finally forms HMF. The effectiveness

of chromium (III) is likely due to the low substitution rate across the first row of transition metals. The low substitution is caused by the high crystal-field stabilization energy of the ion forms, resulting in high activation energies required to achieve reaction intermediaries<sup>123,124</sup>.

Additionally, similar work using sulfated metal oxides has shown transition metals to be effective catalysts. The duality of containing both Lewis and Brønsted acid sites is likely the root of the enhanced catalytic activity<sup>125</sup>. These acid sites produce an activated complex with the biomass and form carbocations during initiation, and continue throughout the chain propagation phase<sup>126</sup>. Each broken C-C bond has the potential to generate a new carbenium ion, which can desorb and form alkenes or alkanes, or interact with the reactant<sup>127</sup>. Shao et al. utilized sulfated TiO<sub>2</sub> nanosheets to bolster the conversion of fructose to ethyl levulinate in ethanol and fructose to HMF in dimethyl sulfoxide<sup>128</sup>. Lu et al. found high rates of oligomer and primary pyrolysis product reduction, and increases in light furans when reacting cellulose with SnO<sub>2</sub> and ZrO<sub>2</sub><sup>129</sup>.

The existing literature has investigated a handful of metal catalysts in conjunction with biomass undergoing thermochemical conversion, however not all possible metal catalysts have been investigated, and no unifying understanding yet exists. The knowledge of these discrete studies is not yet full enough to develop a general understanding of how metals affect biomass during thermochemical conversion. Additionally, many common and potentially useful transition metals have been excluded from consideration. This work identifies a wider array of potential transition metal catalysts that positively impact the pyrolysis of cellulose. The use of transition metals as *in situ* catalysts reduces the number of downstream upgrading steps and reduces the energy input required to form the end product. Additionally, if common and inexpensive transition metal

catalysts can be identified as effective catalysts, the need to recharge and recycle 100% of the metals is not as pressing. Cellulose, used as a model biomass compound, is one of the most abundant biopolymers, whose properties have been well researched and are understood. The effects of transition metals on cellulose reaction rates are measured based on thermogravimetric analysis (TGA); the production of non-condensable gases analyzed via residual gas analyzer mass spectroscopy (RGA); changes in bio-oil characterized through gas chromatography-mass spectroscopy (GC-MS). By incorporating transition metals directly into cellulose pyrolysis, the aim is to: (1) reduce the formation of large tar compounds in the bio-oil, (2) increase small stable aromatic hydrocarbon production in the bio-oil, and (3) Initiate thermal degradation of cellulose at lower pyrolysis temperatures. From a fundamental standpoint, this work may open new lines of inquiry into the development of catalysts for pyrolysis biofuel upgrading by understanding key reactions promoted or curtailed by the use of transition metals. In addition, heterogeneous biochar-catalyst composites – made by pyrolyzing metal-impregnated biomass – are emerging as catalysts for downstream biorefinery applications<sup>130</sup>, as well as functionalized adsorbents<sup>131–133</sup> and even support for wound dressings<sup>134</sup>.

## **4.1 Materials and Methods**

Six metal acetate compounds were procured from Sigma Aldrich: Iron(II) [Cat:339199, 95%], silver [Cat:85140, ≥99%], manganese(II) [Cat:221007, ≥99%], copper(II) [Cat:341746, 98%], nickel(II) [Cat:244066, 98%], and zinc [Cat:383058, ≥98%] and were used as received. A wet impregnation method with cellulose was selected to ensure uniform distribution of metals within the biomass matrix.

Cellulose filter paper (GE Whatman Grade 40, Cat:1440-090) was soaked in 50. mL of 0.05 molar metal solutions made with Milli-q water (18.2 m $\mu$ -cm/25°C) for one hour. Additionally, a blank set was introduced, where the cellulose filter paper was soaked in only the Milli-q water with no metal. Five sets of the blank and each metal-cellulose impregnation were created: one for TGA analysis (replicate 1A), and four for furnace pyrolysis (1B-1E). A hole punch was used to generate approximately 3mg cellulose disks from the 1A replicate for TGA analysis. To ensure enough sample was available for analysis post-pyrolysis, two filter paper sheets were run simultaneously in duplicate (replicates 1B&1E and 1C&1D). Samples were dried at room temperature for three days. Both acetate and metal are adsorbed by the cellulose filter paper, and to determine the metal uptake the acetate component must be accounted for. The adjusted metal uptake on the filter papers is expressed as a percent change in Table 4.1. With five filter papers of each type generated, two are paired together to ensure enough sample, and this process is repeated for a duplicate run to ensure the accuracy of measurements. Papers ‘B’ and ‘E’ are run simultaneously and are compared to papers ‘C’ and ‘D’ to confirm the accuracy of biochar, bio-oil, and pyrolysis gasses generated. Throughout this section, where applicable/feasible, results are presented as the average  $\pm$  one standard deviation with three or more trials, or as the average  $\pm$  a percent difference between duplicate trials. TGA and proximate analysis were run as duplicates from a single filter paper (‘A’).

**Table 4.1** Percent change of metal uptake on cellulose (by mass)

	<b>Replicate 1A (%)</b>	<b>Replicate 1B (%)</b>	<b>Replicate 1C (%)</b>	<b>Replicate 1D (%)</b>	<b>Replicate 1E (%)</b>	<b>Average <math>\pm</math> STDEV</b>
<b>Silver</b>	2.9	3.3	2.5	2.8	2.9	2.9 $\pm$ 0.24
<b>Iron(II)</b>	2.3	1.4	1.1	1.3	1.2	1.5 $\pm$ 0.42
<b>Copper(II)</b>	1.7	1.4	1.1	1.2	1.1	1.3 $\pm$ 0.22
<b>Manganese(II)</b>	2.0	1.6	1.3	1.4	1.5	1.6 $\pm$ 0.24
<b>Nickel(II)</b>	1.8	1.6	1.3	1.4	1.3	1.5 $\pm$ 0.19
<b>Zinc</b>	2.0	1.7	1.4	1.5	1.4	1.6 $\pm$ 0.23

The metal uptake on cellulose filter paper represented an average 1.7% increase in mass, with all except one sample remaining within two standard deviations. The outlier, silver, can be explained: silver complexes with a single acetate, whereas the rest of the metals pair with two. Given the same uptake of mass, a greater portion remaining is silver. The blank samples showed no significant change in mass after soaking in Milli-Q water.

A second and third group of copper and nickel impregnated filter papers (and a new set of blanks) was produced after the original trials of metals in Table 4.1 to examine the effects of changing pyrolysis conditions on these two candidate metals. Copper and nickel were chosen for their observed ability to enhance hydrogen gas production. This set of 24 filter papers were similarly paired to pyrolyze two at the same time to give an additional 3 pyrolysis samples for each metal in duplicates. Replicates 2A&2D, 2B&2E, 2C&2F, 3A&3D, 3B&3E, and 3C&3F were pyrolyzed together. Percent change in mass from metal uptake in the second and third group are recorded in Table 4.2 With an average mass increase of 0.93%, these samples are lower than the first group, but remain within 2 standard deviations of each other. Group 1 reused the metal acetate solution across the 5 replicates: adding back the quantities absorbed. This required preparing samples

**Table 4.2** Percent change of copper and nickel uptake on cellulose

	<b>Replicate 2A (%)</b>	<b>Replicate 2B (%)</b>	<b>Replicate 2C (%)</b>	<b>Replicate 2D (%)</b>	<b>Replicate 2E (%)</b>	<b>Replicate 2F (%)</b>	<b>Average ± STDEV</b>
<b>Copper(II)</b>	0.87	0.96	0.99	0.94	0.98	0.97	0.95 ± 0.04
<b>Nickel(II)</b>	1.11	1.09	1.15	1.13	1.11	1.11	1.12 ± 0.02
	<b>Replicate 3A (%)</b>	<b>Replicate 3B (%)</b>	<b>Replicate 3C (%)</b>	<b>Replicate 3D (%)</b>	<b>Replicate 3E (%)</b>	<b>Replicate 3F (%)</b>	<b>Average ± STDEV</b>
<b>Copper(II)</b>	0.67	0.70	0.71	0.71	0.69	0.69	0.70 ± 0.01
<b>Nickel(II)</b>	0.94	0.98	1.00	0.96	0.96	0.97	0.97 ± 0.02

individually, so in the interest of time, groups 2 and 3 were prepared simultaneously without reusing solution.

Group 1 (outlined in Table 4.1) were all subject to the same pyrolysis conditions: 10°C/min to 600°C for one hour, with 100mL/min of nitrogen purge gas. Groups 2 and 3 included a mix of pyrolysis conditions, including lower final temperatures (Batch 2C&2F and 3C&3F) and higher nitrogen purge rates (Batch 2B&2E and 3B&3E). The differences in pyrolysis conditions are illustrated in Table 4.3.

**Table 4.3** Group and batch experimental pyrolysis matrix

	<b>Group 1</b>	<b>Batch 2A&amp;2D</b>	<b>Batch 2B&amp;2E</b>	<b>Batch 2C&amp;2F</b>	<b>Batch 3A&amp;3D</b>	<b>Batch 3B&amp;3E</b>	<b>Batch 3C&amp;3F</b>
<b>Final pyrolysis temperature (°C)</b>	600	600	600	350	600	600	350
<b>Nitrogen purge gas rate (mL/min)</b>	100	100	200	100	100	200	100

Pyrolysis was conducted as outlined in sections 3.1.1 with few modifications. Batches 2B&2E and 3B&3E were run at 200mL/min of N<sub>2</sub> gas (instead of 100mL/min) to determine the effect of purge gas rate on bio-oil formation. Additionally, the bio-oil collection setup was reworked to increase the condensation surface area by utilizing thinner and longer cold traps (Chemglass schwartz drying tubes). Finally, insulating blocks were wrapped around a 10mm diameter quartz tube, used to pull the pyrolysis gases from the middle of the furnace in order to keep the gases hotter to prevent premature condensation of the bio-oils. The reworked setup can be seen in Figure 4.1.

Impregnated cellulose samples were placed in a porcelain combustion boat in the furnace, and the furnace was purged with nitrogen for 10 minutes before starting, to allow residual oxygen to be

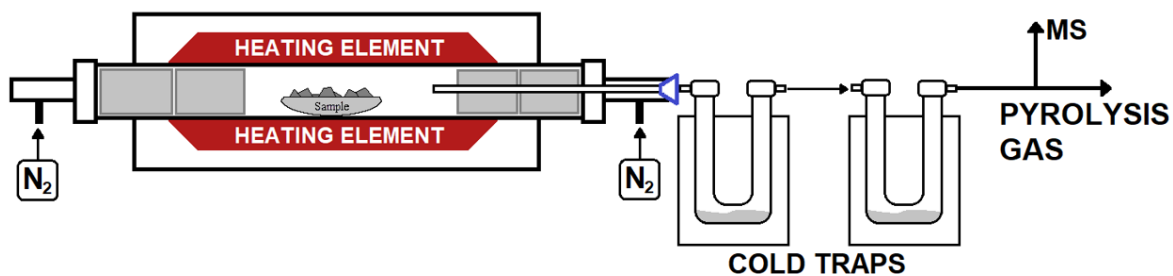


**Figure 4.1** Pyrolysis tube furnace setup

displaced. Samples were heated at 10°C/min to 110°C for 30 minutes to drive off residual moisture before continuing up to 600°C and holding for 60 minutes. Batches 2C&2F and 3C&3F were run to only 350°C for 60 minutes to examine the low temperature formation of bio-oil. The furnace was cooled to 80°C before samples could be retrieved, to ensure that the heated sample was not oxidized. The resulting biochar was weighed to determine the solid yield mass fraction, and the cold traps were weighed and rinsed with 10mL DCM (dichloromethane) to recover the bio-oil. Water is a byproduct of pyrolysis and must be removed from the bio-oil before analysis. The total amount of water generated during these experiments was less than 2% of the bio-oil by weight. After extraction from the cold traps, the bio-oil was diluted and prepared as described in section 3.1.2.

## 4.2 Results and Discussion

The pyrolysis of cellulose with *in situ* metal catalysts yields liquid, solid, and gaseous products. By examining the changes in yield and composition we can determine the extent of the catalysts effectiveness.

### 4.2.1 Proximate Analysis

Batch 1A was used to determine proximate analysis of samples after metal impregnation. While the cellulose filter paper is sold as ashless, the addition of the metal acetates introduces a small quantity of oxidizable material, as seen in Table 4.4. The duplicates are averaged and the percent difference between duplicate runs is given in the last column.

The largest portion of cellulose resides in the volatile matter region, with little remaining as fixed carbon, and ash attributed to the addition of the metal catalysts. This is in agreement with the body of literature surrounding the thermal degradation of cellulose<sup>135,136</sup>.

**Table 4.4** Proximate analysis of metal impregnated filter papers

	<b>Volatile Matter</b> [wt % dry basis]	<b>Fixed Carbon</b> [wt % dry basis]	<b>Ash</b> [wt % dry basis]	<b>Percent Difference Between Duplicate Runs (%)*</b>
<b>Blank</b>	96.43	3.43	0.14	1.13
<b>Silver</b>	96.05	3.01	0.95	0.83
<b>Iron(II)</b>	96.34	2.75	0.91	0.54
<b>Copper(II)</b>	97.11	2.44	0.46	0.47
<b>Manganese(II)</b>	93.91	5.50	0.60	0.41
<b>Nickel(II)</b>	98.42	0.89	0.52	0.48
<b>Zinc</b>	92.46	7.17	0.36	0.85

### 4.2.2 Residual Gas Analysis

Non-condensable gas production (baselined to weight of input cellulose) offers insight to the impact of metal on the cellulose filter paper, as carbon dioxide and hydrogen gas are indicators of pyrolytic activity. Carbon dioxide, being a low-energy state product, confirms that the cellulose is undergoing a transformation, namely devolatilization. Cellulose depolymerizes and forms tar, char, and carbon dioxide when undergoing (initial) pyrolysis<sup>137</sup>. Dehydrogenation is similarly an

indicator, as the formation of hydrogen gas by the scission of C-H bonds leads to increased H<sub>2</sub> formation while preserving C-C and C-O bonds<sup>26,103,138</sup>. Figure 4.2 illustrates the carbon dioxide

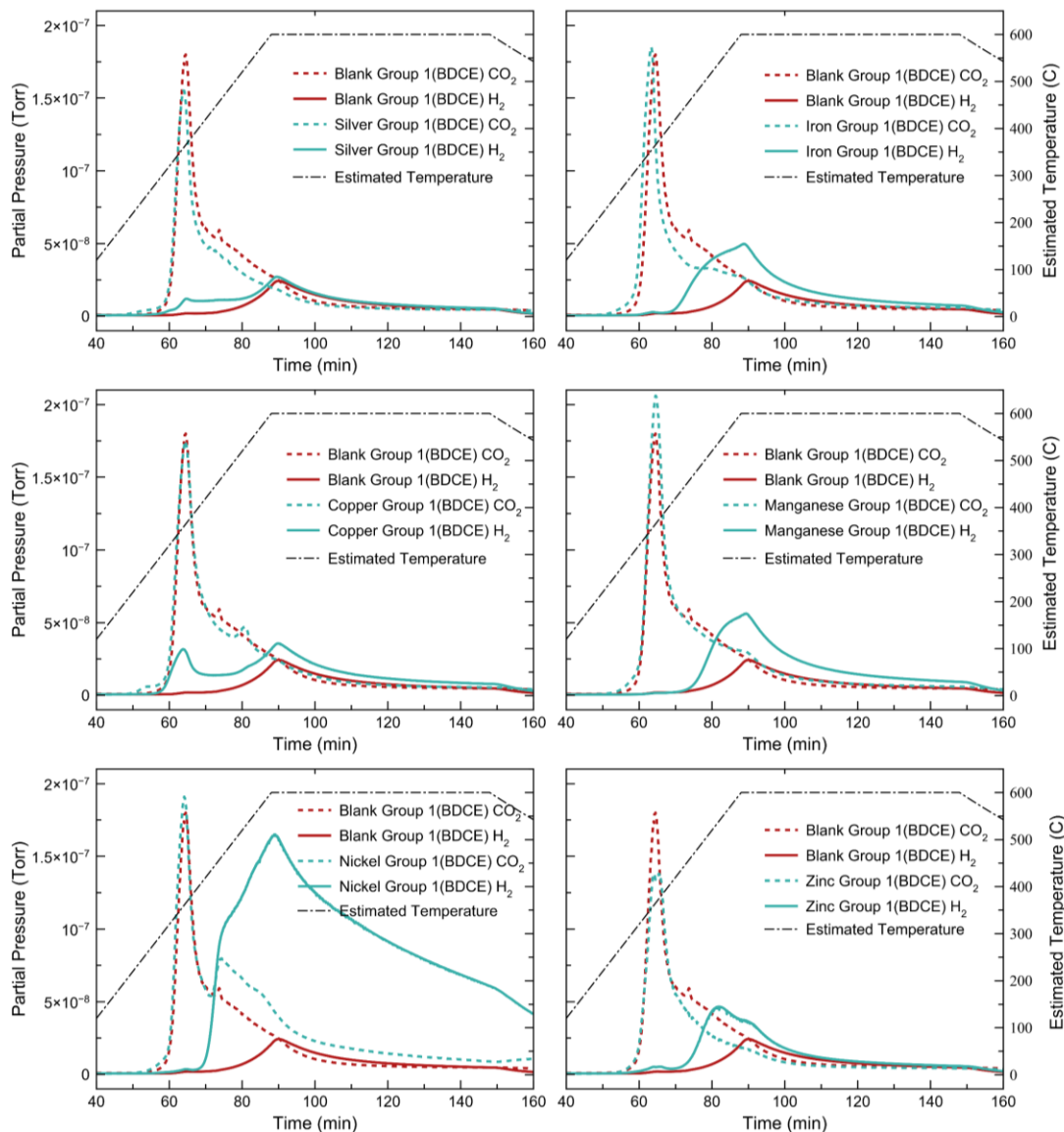


**Figure 4.2** Carbon dioxide (dashed) and hydrogen (solid) evolving for group 1 impregnated cellulose filter papers

and hydrogen formation during group 1 pyrolysis trials (averaged duplicates), with the carbon dioxide gas evolution peaking around minute 65 (at approximately 360°C), and hydrogen between 65 and 90 minutes (360-600°C). While it takes approximately 12 minutes to cycle the whole volume of the furnace and tubing at 100mL/min, gases generated from the sample are quickly

siphoned out of the furnace, and little lag is observed between generation and detection. This is confirmed by hydrogen's response to changing temperatures.

For samples such as silver, copper, and nickel, as the temperature approaches 600°C, hydrogen continues to rise. Once a steady temperature of 600°C is reached, production begins to decrease. The temperature directly drives the hydrogen gas formation. Additionally, when the furnace begins to cool around 145 minutes, the hydrogen gas evolved starts to decrease faster. Were there a significant lag in response and temperature, there would be a corresponding gap in these peaks. The pyrolysis method for each sample in group 1 is the same, with only the metal differentiating the samples. While manganese peaks high and early – when compared to zinc's lower and later production, the differences between same-metal duplicates help highlight the inherent variability. Copper and nickel each produce an additional CO<sub>2</sub> peak between 75 and 85 minutes (470-570°C).

Figure 4.2 also highlights hydrogen gas production for group 1 where again copper and nickel are noted to significantly influence gas production. Nickel produced on average 934% (851.1% and 1017.6% over two runs; data in Appendix B) more hydrogen gas than the blank no-metal baseline. Conversely, while copper produces a comparatively modest 90% (87.6% and 92.5% over two runs; data in Appendix B) increase, a large portion of that production occurs earlier during the pyrolysis process: between 60-65 minutes (320-370°C). This low temperature production may potentially lead to a more efficient thermochemical conversion scheme by reducing processing temperature and therefore energy requirements.

Figure 4.3 highlights methane and ethane production. The inclusion of metals decreased methane production in all cases except for copper, where it was marginally increased. This trend of decreasing methane production leads to a less energy-dense pyrolysis gas (which could be combusted to offset the heating demands of the furnace). A decrease in methane – and gaseous hydrocarbons in general – equates to increased carbon and hydrogen remining in the biochar and/or bio-oil. Where a less oxygenated bio-oil is desired, this increase in carbon and hydrogen favorably

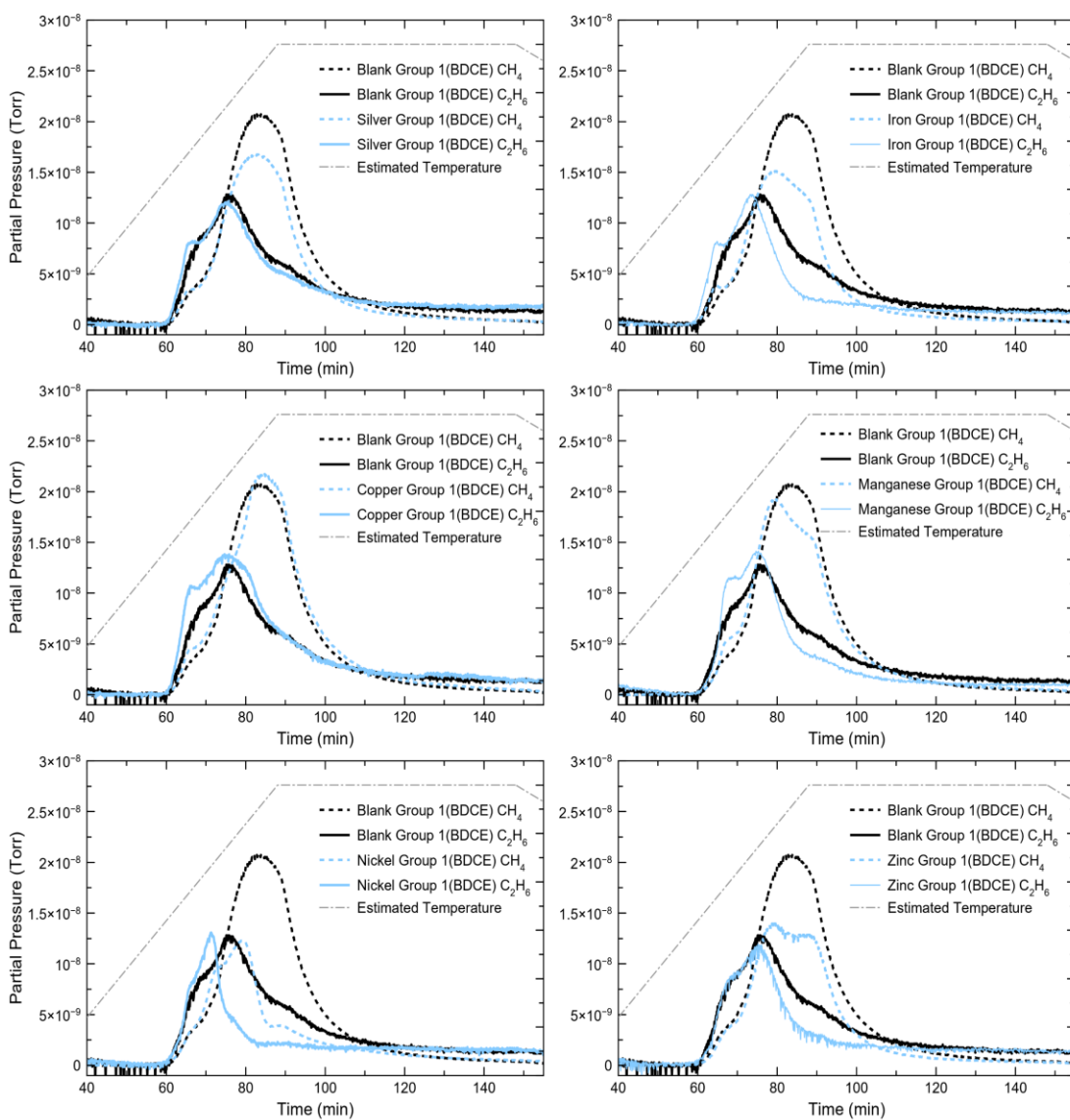


**Figure 4.3** Methane (dashed) and ethane (solid) evolution for group 1 impregnated cellulose filter papers

improves the carbon/oxygen ratio of the bio-oil. The quantity of ethane produced saw little change over all trials, however, copper, manganese and nickel saw slightly earlier formation. This trend to form more ethane at slightly lower temperatures potentially hints at reduced barriers to conversion. Further exploration to strengthen this correlation is required before making definitive assertions.

Because copper and nickel exhibit considerably higher gas evolution than the other metals investigated, both were repeated in experimental groups 2 and 3 with lower final pyrolysis temperatures (350°C reduced from 600°C) and higher purge gas sweep rates (200mL/min up from 100mL/min) to confirm the low temperature production and to determine the extent of tar recondensation on the biochar. Figure 4.4 depicts the hydrogen gas evolution over the three conditions (average of duplicates presented here). Batches 2 and 3 AD (solid lines) were pyrolyzed

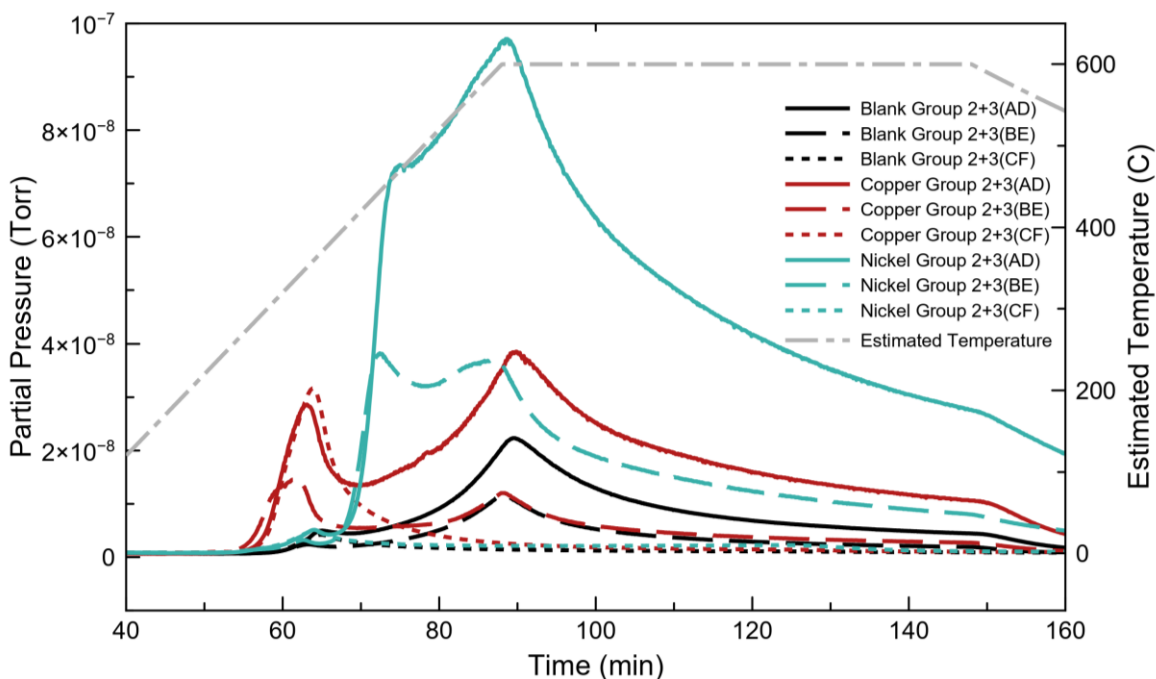


**Figure 4.4** Averaged hydrogen gas evolution for batches 2 and 3 impregnated cellulose filter papers

at the same conditions as group 1 (600°C with 100mL/min N<sub>2</sub> purge). Nickel again produced a larger quantity of hydrogen over the no-metal baseline, increasing hydrogen production 328% (287.7% and 368.4% over two runs; data in Appendix B) over the pure cellulose trial. Although not as high as group 1, this could potentially be attributed to the lower ratio of metal to cellulose. Copper's batch 3A&3D additionally produced more hydrogen when compared to 2A&2D, although crucially both still contain the early peak between 60-65 minutes (320-370°C). The low temperature trials of 2C&2F and 3C&3F (peak temperature of 350°C) produced the same quantity of hydrogen between 55-70 minutes as 2A&2D and 3A&3D (peak temperature of 600°C), confirming copper's ability to catalyze thermochemical conversion at lower temperatures. This is highlighted by the fact that the no-metal baseline cellulose pyrolysis yields approximately 1/10<sup>th</sup> of the hydrogen over the same range. The high sweep rate of 200mL/min for batches 2B&2E and 3B&3E produces a lower hydrogen signal, but it is important to remember that this hydrogen is diluted in twice the nitrogen. If corrected for the increased dilution, copper and nickel effectively generated the same quantity of hydrogen, differentiating by 0.18% and 0.31% respectively. Copper and nickel's carbon dioxide differed by 0.04% and 0.25% respectively. Increasing the sweep gas rate had no significant effect on the gases generated.

#### **4.2.3 Gas Chromatography Mass Spectroscopy Analysis of Pyrolysis Bio-oil**

Bio-oil quantities across samples were normalized to the input mass of cellulose. Table 4.5 shows average biochar, bio-oil, and bio-oil water (limited to trials with final temperatures of 600°C) with standard deviations for the control, nickel, and copper which were run six times over the two groups at the 600°C condition. Percent difference is reported for the remaining values which were run twice. As we can see, the increase in bio-oil yield for the copper and nickel versus the pure cellulose are not statistically significant. The remaining metals were run twice each (in group 1),

**Table 4.5** Average biochar, bio-oil, and bio-oil water yields at 600°C ( $\pm$  one standard deviation where  $n > 2$ , otherwise error reported as percent difference between duplicate trials.)

	Average biochar yield (% wt)	Average bio-oil yield (% wt)	Average bio-oil water content (% wt)
<b>Blank (no-metal)</b>	12.43 $\pm$ 0.55	73.8 $\pm$ 11.7	1.54 $\pm$ 0.47
<b>Copper</b>	14.14 $\pm$ 0.91	78.3 $\pm$ 10.1	1.27 $\pm$ 0.55
<b>Nickel</b>	9.45 $\pm$ 1.68	71.0 $\pm$ 11.4	1.60 $\pm$ 1.16
<b>Silver</b>	13.14 (18.2%)	81.0 (18.8%)	2.11 (37.0%)
<b>Iron</b>	15.13 (2.6%)	76.1 (26.4%)	3.23 (23.3%)
<b>Manganese</b>	15.26 (0.4%)	81.3 (17.4%)	2.84 (28.2%)
<b>Zinc</b>	16.68 (0.5%)	62.9 (33.6%)	3.32 (33.7%)

and as a result have too few data points to accurately draw conclusions. Copper, nickel, and the control however were each run six times over the three groups (excluding the two low temperature batches 2C&2F and 3C&3F where little oil is generated).

Most of the metal catalyst biochar yields increase slightly over the control. These values are reported on a pure-biomass basis and discount the addition of the metals which would further increase the weight of the remaining biochar. An increase in biochar weight could be an indicator of decreased primary devolatilization, or a tendency to favor the recondensing of tar compounds during secondary pyrolysis<sup>139</sup>. Because the bio-oil yields are mixed – some higher than the blank and some lower – there is no blanket consensus on whether the initial devolatilization is significantly affected since there should be an increase in either the oil or gas phases. Instead, if the metals favor tar depositing back on the biochar surface, then a corresponding decrease in tar compounds in the oil would be expected.

The water content of the bio-oils is similarly mixed. Water is an expected byproduct of the pyrolysis process, and with an oxygen-deficient atmosphere, the formation of water requires the oxygen sourced from the biomass itself<sup>140</sup> (in an otherwise dry nitrogen purge stream). An increase

in bio-oil water potentially leads to fewer oxygenated compounds in the gas stream, or fewer oxygenated bio-oil compounds. One of the primary ways oxygen leaves through the gas phase is via CO and CO<sub>2</sub><sup>141,142</sup>. A reduction in oxygen here would correlate to a reduction in carbon. This carbon, when retained in the oil or char, represent an increase in available energy-valuable bonds. A reduction in oxygen in the bio-oil compounds is an improvement, as fewer oxygen atoms equates to an increase in energy density, decreases instability, and reduces acidity. High water contents in the oil however present a problem at scale. Water must be removed before the bio-oil can be stored or used.

Table 4.6 highlights the 11 most prominent bio-oil compounds identified in each sample from group 1 and are represented as a percent change from the baseline (no-metal) cellulose blank. The duplicate runs were averaged to incorporate both sets of data. The individual percent change data can be found in Appendix B. In general, desirable light compounds elute at lower retention times, and are therefore at the top of the table. Heavier tar compounds (*italicized and bolded*) are seen in

**Table 4.6** Group 1 bio-oil compound yields expressed as percent change in chromatogram area versus pure cellulose (negative indicates decrease in yield versus cellulose)

	MW (g/mol)	Ag (%)	Fe (II) (%)	Cu (II) (%)	Mn (II) (%)	Ni (II) (%)	Zn (%)
Furfural	96.08	-27.6	-11.4	-40.5	-9.3	25.4	60.8
2-Propyl Furan	110.15	-14.1	-55.6	-2.8	-61.4	-20.4	-43.8
2(5H)-Furanone	84.07	-0.4	-47.2	-37.7	49.3	19.4	16.5
1-(2-furanyl)-Ethanone	110.11	35.3	-13.5	19.0	-31.7	-2.7	-16.0
3-Hydroxy-2(1H)-Pyridinone	111.10	-48.6	53.9	-38.9	148.2	563.4	-15.0
5-methyl-2-Furancarboxaldehyde	110.11	-26.6	55.9	-31.2	43.1	144.2	151.8
Phenol	94.11	1.4	-28.8	-17.2	-17.6	-13.1	-2.4
3-methyl-1,2-Cyclopentanedione	112.13	-10.3	94.1	8.5	46.7	78.0	23.6
<b><i>Levogluosenone</i></b>	126.11	34.0	-37.3	57.4	-38.4	-1.0	14.3
Heptanal	114.19	-62.2	78.9	-61.8	49.3	190.1	446.8
<b><i>1,4:3,6-Dianhydro-<math>\alpha</math>-D-glucopyranose</i></b>	144.13	-8.0	-24.7	-2.9	-20.3	-16.9	6.7
<b><i>1,6-anhydro-<math>\beta</math>-D-Glucopyranose</i></b>	162.14	11.3	23.7	-31.6	36.9	-37.4	-44.5

the latter half of the table, with the notable exception of heptanal, which while containing an alcohol group, is not nearly as oxygenated as others around it.

Many of the changes to the bio-oil are subtle or lateral – with compounds often being replaced by isomers or congeners. Pure cellulose generates a significant quantity of furfural, which is used in industry as a feedstock to generate other furan derivatives<sup>143</sup>. Furfural – and other light compounds – decreased in prominence with the addition of most metals. Notable exceptions to this are nickel, copper, and zinc.

Nickel bolstered the formation of furfural, 3-hydroxy-2(1H)-pyridinone, 5-methyl-2-furancarboxaldehyde, and heptanal. These four compounds already represent a major fraction of the bio-oil composition, and if isolation of these potential biorefinery feedstock compounds is desired, the addition of nickel would represent a major improvement in yields. In addition, nickel decreased the large undesirable tar compounds levoglucosenone, 1,4:3,6-Dianhydro- $\alpha$ -d-glucopyranose, and 1,6-anhydro- $\beta$ -D-Glucopyranose, which are contributors to bio-oil's generally high viscosity and acidity and low stability<sup>144</sup>. Zinc had a similar effect on the bio-oil as nickel, increasing furfural and heptanal, and decreasing some tar formation (1,6-anhydro- $\beta$ -D-Glucopyranose), although not to the same degree as nickel. Copper, despite the early low-temperature dehydrogenation, increased the quantity of levoglucosenone – a preliminary pyrolysis product indicative of activity, but an undesirable end-product. This makes copper appear undesirable as a catalyst, however given copper's activity at low temperature, group 2 and 3 bio-oil must be examined for a direct comparison.

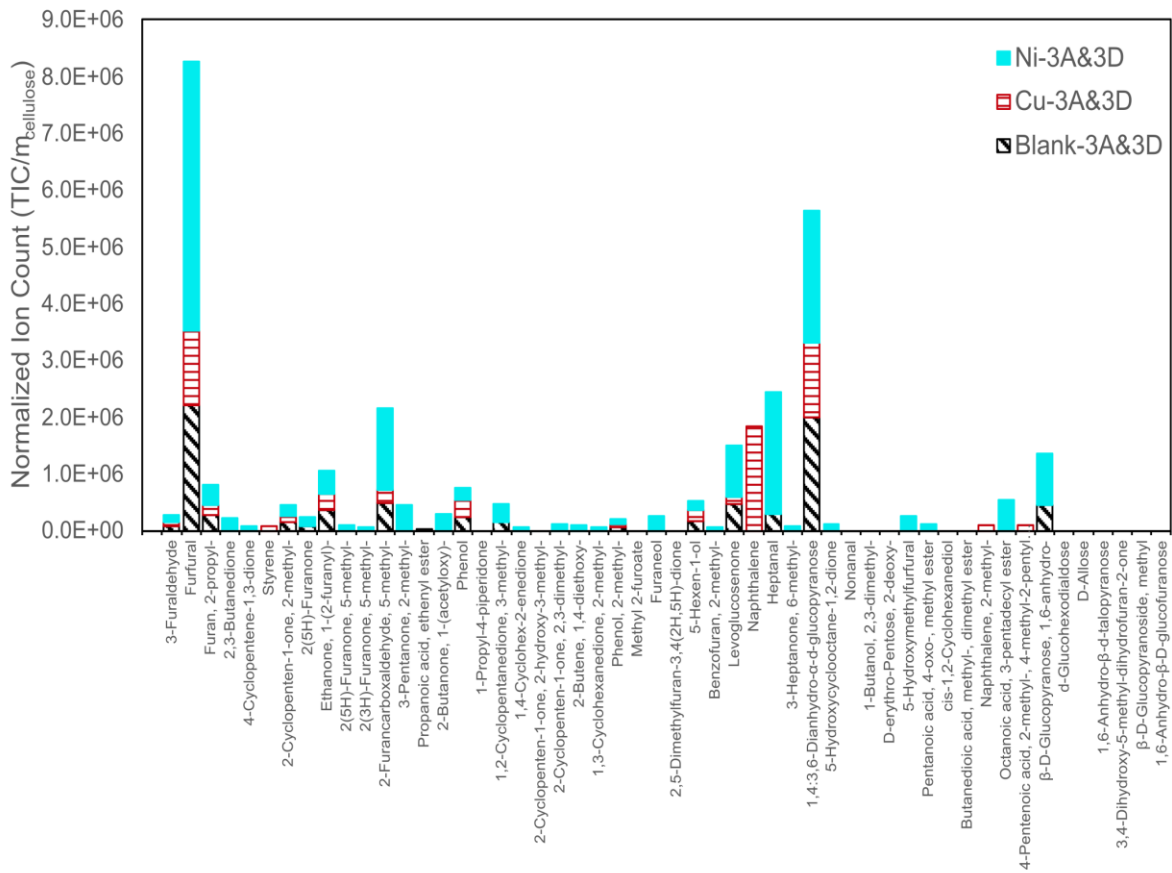
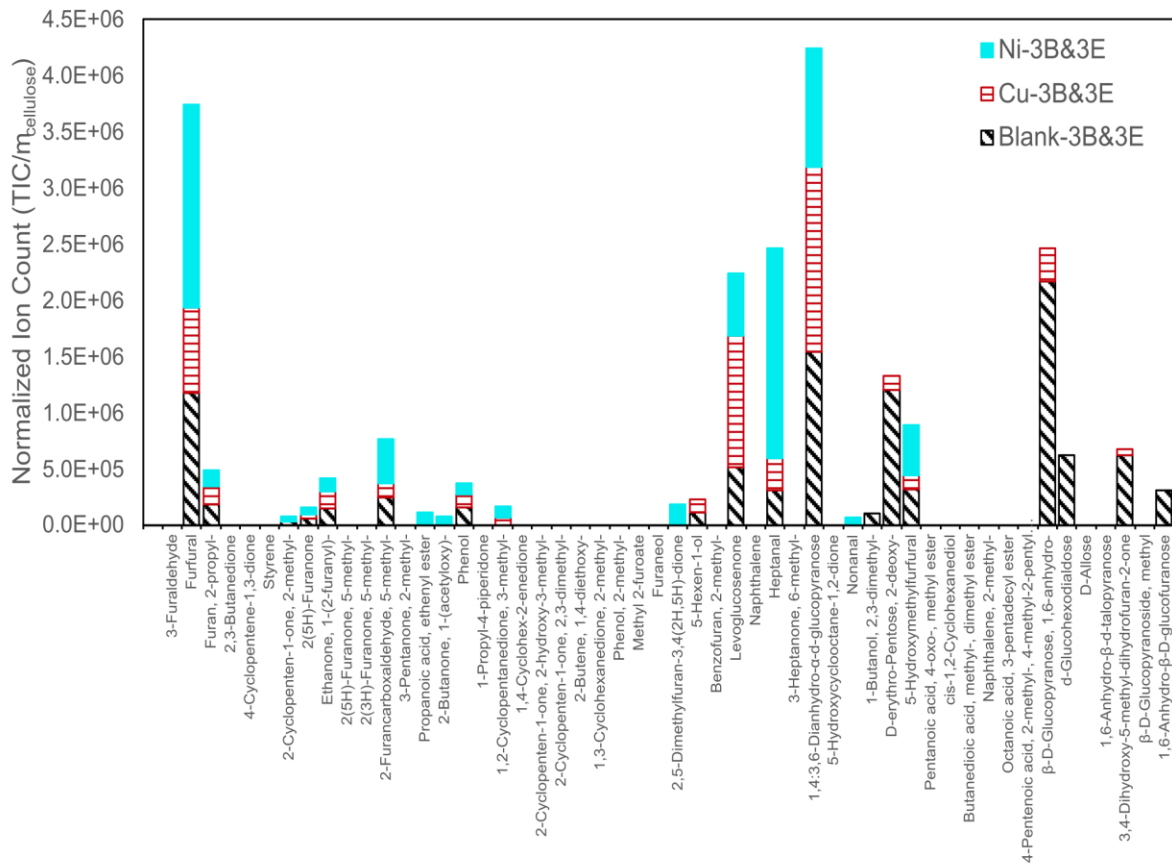


**Figure 4.5** Bio-oil compound distribution normalized to mass of input cellulose at 600°C and 100mL/min

Figure 4.5 illustrates the compound distribution for groups 2 and 3 at 600°C, 100mL/min copper and nickel trials. Looking at large-scale change between these trials, nickel produces a wider array of products (and often in higher quantities) at all retention times. Light aromatics tend to appear at low retention times, with larger undesirable tar compounds eluting at higher retention times. This indicates that nickel’s ability to spur thermal degradation is not limited to any singular region, nor is it likely to be selective during primary or secondary pyrolysis. Nickel enhances the conversion of biomass into oil and gas products, as confirmed by lower amounts of remaining biochar for both high temperature (A&D and B&E) reactions, seen in Table 4.4.

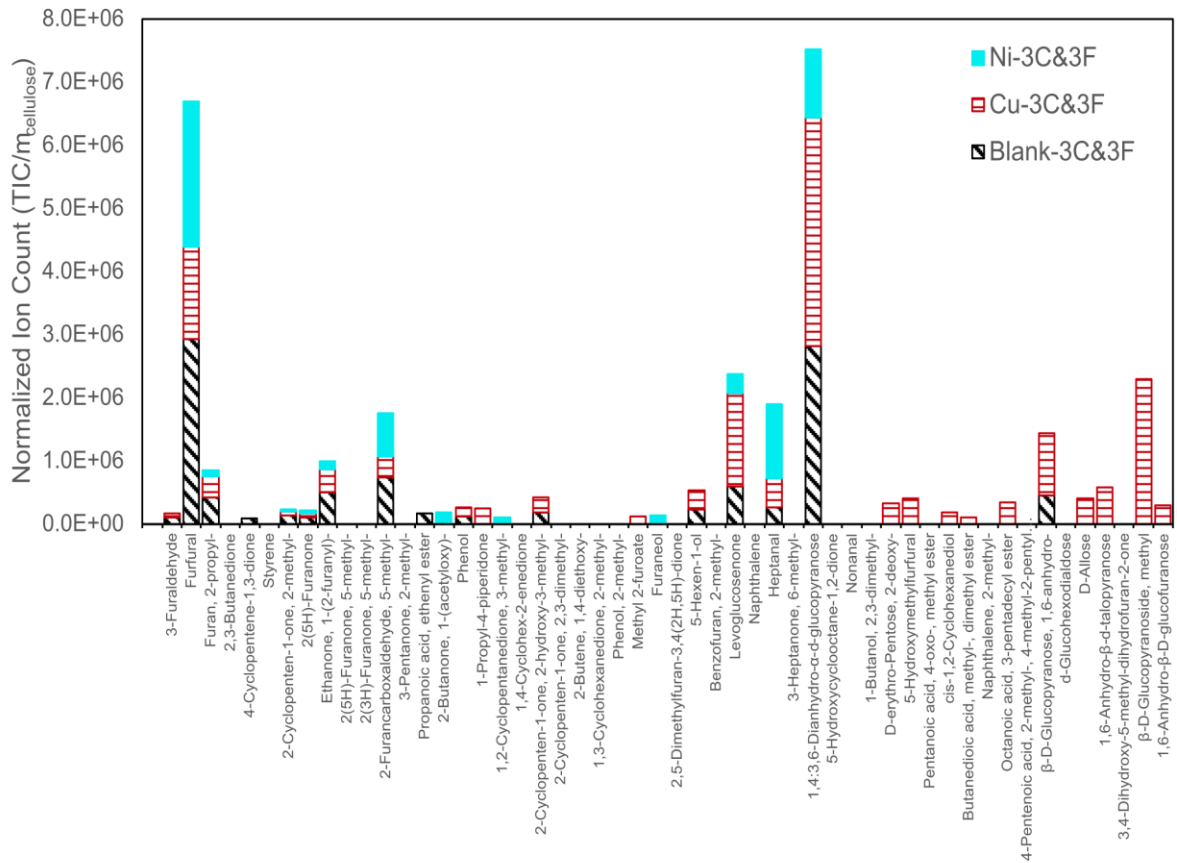
The surface of nickel metal provides a nucleation point for the adsorption and activation of hydrogen, furans, and phenols. This allows the nickel to promote saturation of carbon-carbon double bonds, and assists in the scission of C-O bonds<sup>145</sup>. One of the most efficient methods to form this carbon-carbon bonding is via oxidative cyclization. The nickel likely forms organonickel complexes when reacted with carbon monoxide – a gas produced in abundance during low-oxygen thermal degradation reactions. Organonickel complexes then promote a Pauson-Kahnd reaction: a cycloaddition of alkyne, alkene, and carbon monoxide, forming cyclopentenone derivatives<sup>146</sup>. The effect of nickel on biomass undergoing various thermal degradation schemes has been well studied, however, its role in specific pathways is not as easily identified. This is in part due to its wide effect over the course of thermal degradation, but also the inherent difficulties in isolating the specific pathways themselves<sup>147,148</sup>.

Figure 4.6 highlights the product distribution for groups 2 and 3 at 600°C and 200mL/min of copper and nickel. At higher flow rates, vapors and suspended particulates have little time to react at high temperatures (both heterogeneously at the biochar surface and homogeneously in the gas phase) before being swept from the furnace. With the lower residence time, it might be assumed that nickel and copper would not have ample time to promote reactions, however, nickel produced increased quantities of lower weight aromatics at early residence times, and partially suppressed large heavy weight compounds. An increased flow rate likely prevents recondensation of compounds onto the solid biochar surface, and time-limits heterogeneous gas-char reactions. Copper saw a reduction in the tracked compounds across the board, with a few exceptions. Coupled with no observable drop in total oil yield, this indicated that copper promoted a wider array of compounds at lower concentrations. Peaks between retention times of 23-30 minutes



**Figure 4.6** Bio-oil compound distribution normalized to mass of input cellulose at 600°C and 200mL/min

(corresponding to 5-hexanol, levoglucosenone, heptanal, and 1,4:3,6-Dianhydro- $\alpha$ -d-glucopyranose respectively) saw increases against the baseline. Levoglucosenone and 1,4:3,6-Dianhydro- $\alpha$ -d-glucopyranose are undesirable tar compounds. They represent the first wave of thermal degradation of cellulose and are highly oxygenated and acidic<sup>144</sup>. Closing the mass-balance on bio-oil production becomes progressively more difficult when the products become increasingly diverse. A reduction in observed compounds without a drop in oil yield indicates that a greater number of compounds are produced that do not meet the minimum criteria for detection. This still agrees with copper's ability to break down undesirable tar compounds, but it produces a wider array of new products, instead of generating a homogeneous oil. While at these flow rates



**Figure 4.7** Bio-oil compound distribution normalized to mass of input cellulose at 350°C and 100mL/min

copper does not produce the desired end-products, copper is still promoting the first wave of degradation from cellulose to these primary products.

Figure 4.7 illustrates copper and nickel at low temperatures: 350°C and 100mL/min N<sub>2</sub> flow rate. Without the benefit of high temperatures to activate the devolatilization of cellulose, a catalyst is required. Copper produces the greatest quantity of the large tar compounds, however, while this does not represent an ideal end feedstock, it is an indicator of copper’s effectiveness to promote certain reactions. Coupled with the increase in hydrogen gas production, copper is promoting the conversion of cellulose into the first set of intermediaries – known as the initiation of pyrolysis –

where free radical formation is facilitated by inorganic impurities<sup>149</sup>. However, without the benefit of the final high temperatures, these reactions cannot be carried to completion.

Since the number of reaction pathways in the thermal degradation of lignocellulosic is high, it is unrealistic to assume a single catalyst will be effective at each step. If paired with the right co-catalyst(s) that could take copper's intermediaries and convert them to the final desired products, copper could still play an important role in producing quality bio-oil at potentially lower temperatures.

*In situ* copper and nickel promote thermal degradation of cellulose during pyrolysis. Nickel's ability to increase the variety and quantity of bio-oil compounds, and copper's ability to promote early reactions at lower temperatures make both these metals important options for bio-oil upgrading. The formation of organonickel complexes, such as nickelacycles, are important vehicles for the transformation of organics through carbon-carbon bond formation and carbon-oxygen scission<sup>150</sup>. Meanwhile, copper's variable oxidation states [Cu(0), Cu(I), Cu(II), Cu(III)] allow it to effectively catalyze single and double electron pathway reactions, and its ability to pi-bond can activate terminal alkynes. Copper's affinity to promote click chemistry and carbonylation make it an invaluable tool for improving thermochemical reactions<sup>151</sup>. Future research will investigate complimentary bimetal catalysts, where the beneficial effects of multiple metals could be combined to further improve bio-oil quality.

### 4.3 Summary

This study examines the effects of six pure transition metal catalysts under various pyrolysis conditions to study the products generated and gauge the potential for *in situ* upgrading. The current body of literature presents a narrow scope of specific catalyst-biomass interactions for a limited set of metals. The present work, probing the impacts of six transition metal catalysts, identifies nickel as effective in promoting dehydrogenation and increasing the variety of smaller aromatics while decreasing tar compounds. Copper demonstrates a strong affinity for promoting devolatilization at lower temperature ranges (identified here as 350°C compared to the oft-cited 600°C) to produce larger quantities of the first-stage pyrolysis products. While the addition of copper or nickel alone does not decrease the tar and oxygenated compounds enough to compete with current fossil fuels, this first step potentially decreases the energy barriers – and shapes the pathways – for a more effective biomass to bio-oil conversion.

## Chapter 5: Coupling Materials Informatics and Transition Metal Catalysts

Thus far in our work, the selection of transition metal catalysts was based on two factors: existing previous literature, and whether our experimental design is amenable to its use. Metals available as acetates are soluble in water (to varying degrees) and allow us to soak, then dry the biomass for a consistent impregnation. However, limiting the scope to only these metals risks overlooking well-suited catalysts, and requires testing each individually with minimal indication of how a metal might behave beforehand. Instead, the common trial and error method can be replaced by a materials informatics approach, to identify transition metals and their properties that promote or enhance devolatilization, dehydrogenation, deoxygenation, and/or reduce tar formation.

By adapting existing databases and identifying key metal properties indicative of catalytic activity, we can make predictions about metal catalyst behavior before experimental validation and expand the scope of selection beyond those available as water soluble acetates. In combination with our partners at Boston University, we have identified a large theoretically derived dataset of activation energies of various reactions on metal surfaces produced by Mamun et al.<sup>81</sup>. This list was narrowed down to a set of representative reactions shown in Table 5.1. These are the types of reactions that are expected in thermochemical decomposition of lignocellulosic biomass (and pure cellulose in particular for these experiments), without characterizing the hundreds – if not thousands – of actual pathways. For example, this involves removing excessive oxidation reactions, since the devolatilization is conducted under nitrogen, the only oxygen available is already present in the biomass and cannot constitute a large portion of the reaction pathways.

**Table 5.1** Representative reactions for catalyst material informatics

Number	Reaction
1	$-2.0\text{H}_2\text{O}(\text{g}) + 2.0\text{CO}(\text{g}) + 5.0\text{H}_2(\text{g}) + 2.0^* \rightarrow 2.0\text{CH}_3^*$
2	$2.0\text{CO}(\text{g}) + 1.5\text{H}_2(\text{g}) + ^* \rightarrow \text{CHCO}^* + \text{H}_2\text{O}(\text{g})$
3	$2.0\text{CO}(\text{g}) + \text{H}_2(\text{g}) + ^* \rightarrow \text{CCO}^* + \text{H}_2\text{O}(\text{g})$
4	$\text{CH}_2\text{O}(\text{g}) \rightarrow \text{CH}_2^* + \text{O}^*$
5	$\text{CH}_3\text{CH}_2\text{OH}(\text{g}) + 9^* \rightarrow 2\text{C}^* + 6\text{H}^* + \text{O}^*$
6	$\text{CH}_3\text{CHO}(\text{g}) + 7^* \rightarrow 2\text{C}^* + 4\text{H}^* + \text{O}^*$
7	$\text{CH}_3\text{CO}^* + ^* \rightarrow \text{CH}_3^* + \text{CO}^*$
8	$\text{CH}_3\text{COOH}(\text{g}) + 8^* \rightarrow 2\text{C}^* + 4\text{H}^* + 2\text{O}^*$
9	$\text{CH}_3\text{O}^* + \text{H}^* \rightarrow \text{CH}_3^* + \text{OH}^*$
10	$\text{CH}_3\text{OH}(\text{g}) + 6^* \rightarrow \text{C}^* + 4\text{H}^* + \text{O}^*$
11	$\text{CO}(\text{g}) + 1.5\text{H}_2(\text{g}) + ^* \rightarrow \text{CH}^* + \text{H}_2\text{O}(\text{g})$
12	$\text{CO}(\text{g}) + 2^* \rightarrow \text{C}^* + \text{O}^*$
13	$\text{CO}(\text{g}) + 2.0\text{H}_2(\text{g}) + ^* \rightarrow \text{CH}_2^* + \text{H}_2\text{O}(\text{g})$
14	$\text{CO}(\text{g}) + 2.5\text{H}_2(\text{g}) + ^* \rightarrow \text{CH}_3^* + \text{H}_2\text{O}(\text{g})$
15	$\text{CO}(\text{g}) + \text{H}_2(\text{g}) + ^* \rightarrow \text{H}_2\text{O}(\text{g}) + \text{C}^*$
16	$\text{CO}(\text{g}) \rightarrow \text{C}^* + \text{O}^*$
17	$\text{CO}^* \rightarrow \text{C}^* + \text{O}^*$
18	$\text{CO}_2(\text{g}) + 3^* \rightarrow \text{C}^* + 2\text{O}^*$
19	$\text{CO}_2(\text{g}) \rightarrow \text{CO}^* + \text{O}^*$
20	$\text{COOH}^* \rightarrow \text{CO}^* + \text{OH}^*$
21	$\text{OCH}^* \rightarrow \text{CH}^* + \text{O}^*$
22	$\text{OCH}_2^* \rightarrow \text{CH}_2^* + \text{O}^*$
23	$\text{OCH}_3^* \rightarrow \text{CH}_3^* + \text{O}^*$
24	$\text{OCHOH}(\text{g}) + 5^* \rightarrow \text{C}^* + 2\text{H}^* + 2\text{O}^*$

Additionally, a machine-learning algorithm was employed to fill gaps in the data. Not every reaction was available for each metal, so 80% of the existing data was fed into the machine-learning algorithm, and the remaining 20% used to verify the accuracy of the calculated missing data. The activation energies of the identified reactions were summed across all metals available – not just those included for experimental work – in order to determine the standard deviation of the averaged activation energies. This gives us a standard deviation for each metal, and helps frame how the activation energies compare to the dataset as a whole. Metals with extreme standard deviations (activation energies that are significantly lower or higher than other metals) potentially have high or low binding to the hydrocarbons, potentially deactivating themselves early, or lacking sufficient binding power to become effective catalysts.

By down-selecting this list to include only likely reactions, an overall activation index can be developed. This index sheds insight into how well the catalysts will bind with hydrocarbons, and whether they are likely to deactivate themselves through coking, or lack sufficient binding energy to help the biomass conversion at all.

The activation energies of the selected metals (Cr, Co, Cu, Fe, Mn, Ni, Pd, Zn, Zr) as applied to the representative reactions in Table 5.1 were averaged across all metals and all reactions. An individual metal's average of reaction energies could then be applied to the total group. Those with exceptionally low activation energy might be expected to bind easily with the biomass and catalyze it, but simultaneously run the risk of quickly deactivating<sup>152,153</sup>. Conversely, those with higher-than-average activation energies might never catalyze the reaction at all<sup>154</sup>. Utilizing the same method and experimental setup in chapter 4, nine transition metals were tested on cellulose filter papers. Bio-oil was collected and analyzed via GC-MS, and non-condensable gases were analyzed with the RGA mass spectrometer.

## 5.1 Pyrolysis Product Yields

Initial effects on transition metal pyrolysis are seen through the yield distribution. Figure 5.1 illustrates the quantities of char, bio-oil, and non-condensable gas (by difference) generated under each condition.

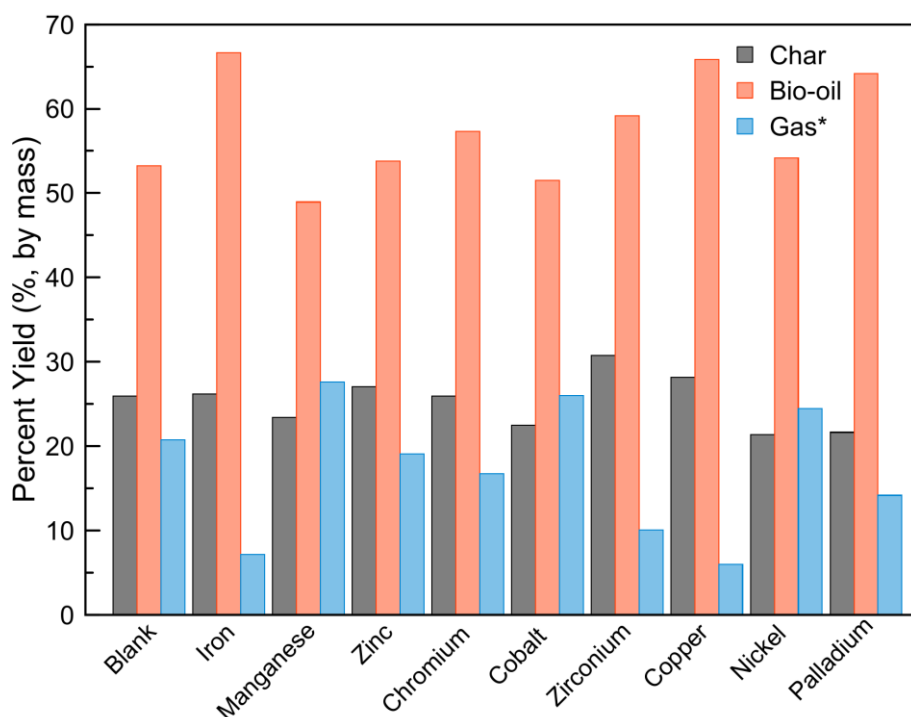


**Figure 5.1** Product distribution for transition metal catalysts on cellulose  
\*Calculated by difference

High yields of bio-oil (50%-70%) are in agreement with previous experiments but show no universal improvement or other trends based on the transition metals used. To examine why some metals generate more oil than others, a comparison against the standard deviation of activation energy is necessary. Figure 5.2 shows the same percent mass bio-oil yields of each metal (as a percent increase against the blank baseline), in line with the metals standard deviation value. If the metals were expected to promote the conversion of solid biomass to liquid bio-oils – and the average activation energy were a good indicator of the metals ability to promote this conversion – then a trend would be expected here. Metals with much lower average activation energy across

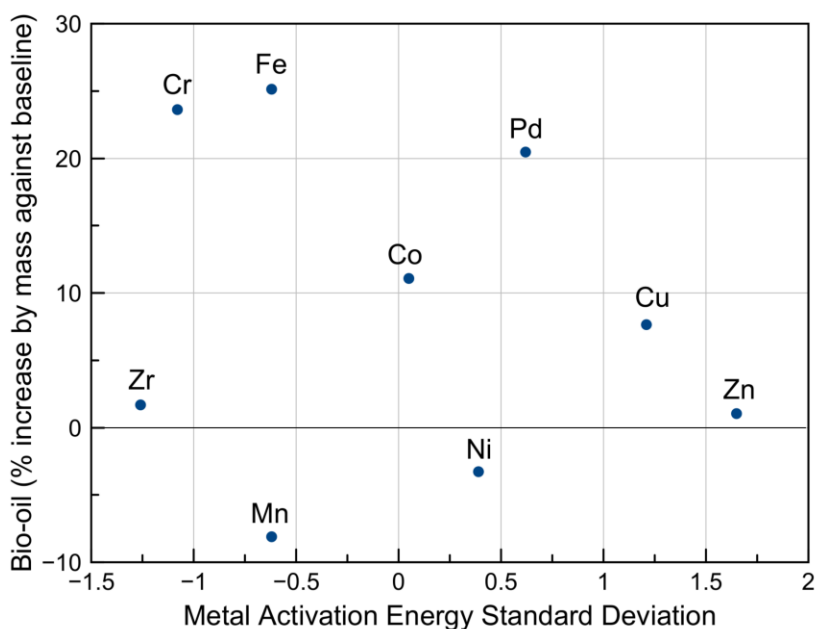


**Figure 5.2** Bio-oil yield as a function of average activation energy

the representative reactions would be expected to generate no or little improvement from the baseline. A negative trend would further indicate that the metals are coking and holding back some material which may otherwise have devolatilized. At the opposite end of the spectrum, high activation energy metals would not have the necessary input energy required to promote the reaction at all. Yield would increase towards the middle of the activation energy plane, however none of these trends are observed here.

However, promoting the increase in oil yield is not the only metric for improvement. The yields may be unaffected, whereas the quality is improved. Additionally, the quality of the product may be a better predictor of non-condensable gas formation.

## 5.2 Bio-oil Quality

A key indicator of pyrolysis bio-oil quality is the presence of oxygenated compounds. Figure 5.3 highlights the quantity of oxygen in each metal-biomass pairing. Similar to the product yield, no obvious pattern is discernable at this level. The oxygen concentration was broken down into ethers, alcohols, ketones, and aldehydes, however again, no clear trend emerges. Average molecular weight does not appear to drive the oxygen content of the bio-oil. While no pattern emerges, six metals (Cr, Fe, Co, Pd, Cu, and Zn) decrease the bio-oil oxygen concentration below the no-catalyst control, improving the quality of the bio-oil.

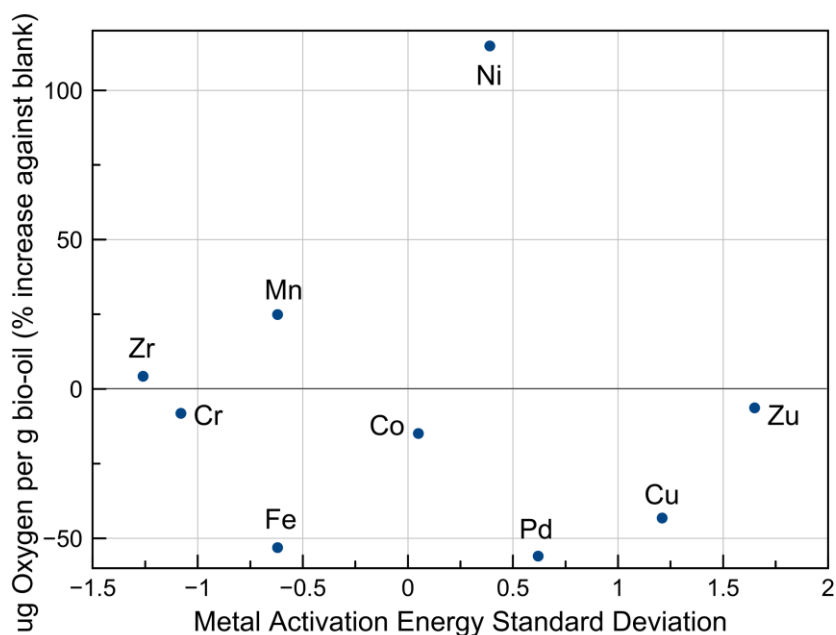


**Figure 5.3** Bio-oil oxygen concentration as a function of metal activation energy standard deviation

## 5.3 Non-Condensable Gas Formation

Non-condensable gas development offers a glimpse into the overall mass balance of the system. If excess carbon, hydrogen, or oxygen is leaving the system through non-condensable gases, then the contents of the bio-oil and/or biochar must adjust to reflect the changes. By comparing the

quantities of gases produced against each metals' overall activation energy, indications for improvement can evolve. Figure 5.4 shows the production of hydrogen, carbon dioxide, and

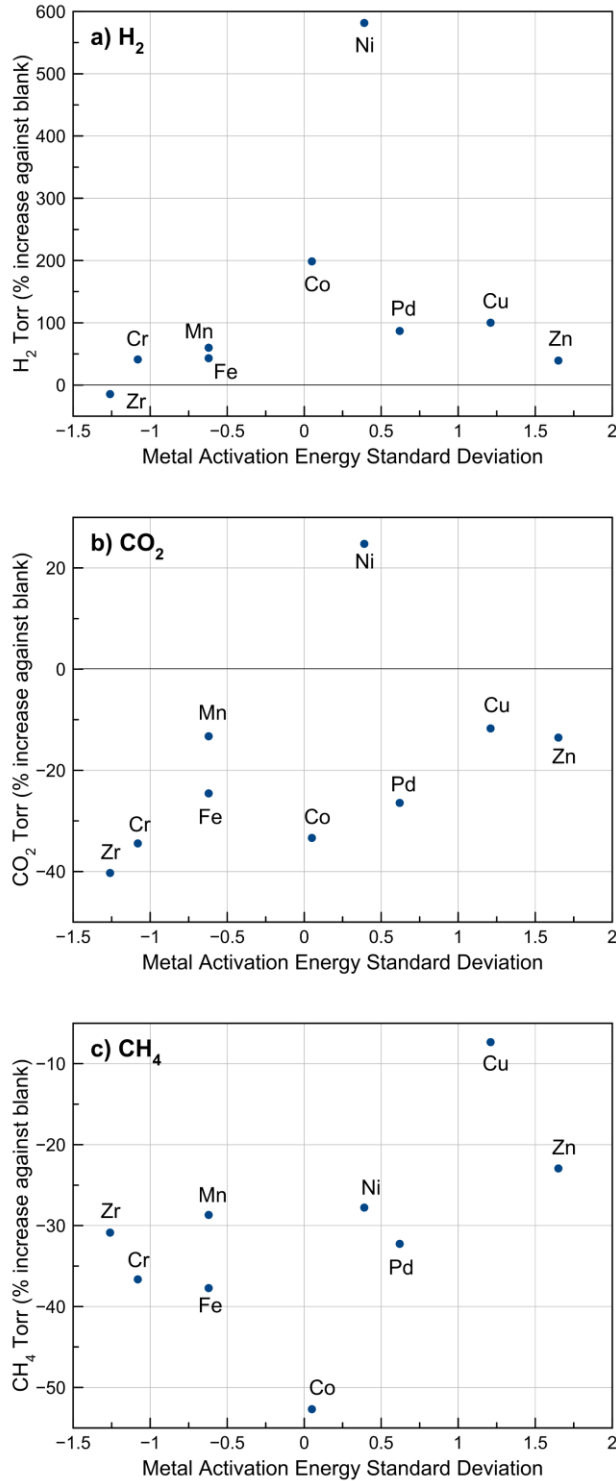


**Figure 5.4** Pyrolysis gas production as a function of metal activation energy standard deviation

methane, ranked to each metals' activation energy. A slight trend starts to emerge with hydrogen production: peaking towards the center of the plot and falling away at the extremes. This initial trend where nickel is a high outlier, indicates that there may be an optimal catalyst activation energy for promoting dehydrogenation.

## **5.4 Summary**

Despite the relationship between a catalyst's activation energy and its ability to promote the representative reactions present in our experimental setup, there is insufficient evidence to link the activation energy index developed here to any of the observed quality improvement indicators. While this does not prove an obvious fundamental link, there are many more determining factors in how a catalyst promotes the devolatilization of biomass to be addressed.

## Chapter 6: Transition Metals as *in/ex situ* Catalysts for Cherry Pits

When transition metals are used in bio-oil upgrading, they are typically not used alone.

Transition metals are often paired with frameworks like zeolites<sup>155–157</sup>, which have their own effect on biomass conversion. This duality adds challenges in separating the combined effects of the metal-zeolite, and the individual effects of the zeolite and metal. Limarta et al. utilized transition metals on various carbon and oxide beds to improve lignin depolymerization<sup>158</sup>, and Li et al. paired transition metals with zeolites to improve the hydrodeoxygenation (HDO) of guaiacol<sup>159</sup>. While the use of the zeolite improved yields over a no-catalyst baseline, this leaves some doubt surrounding the transition metal's role in the process, and broadly what types of reactions are influenced. When transition metals are used by themselves, they are typically utilized in select pathways for the targeted production of chemical feedstock rather than blends of fuel-quality hydrocarbons. For example, Resasco et al. examined the effects of m-cresol over platinum – an important bio-oil component and intermediary, but not representative of the entire bio-oil spectrum<sup>160</sup>. Bodachivskyi et al. started with the representative biomass feedstock cellulose and tracked ethyl levulinate production using metal triflate catalysts. While achieving impressive yields and selectivity of over 70% and 80% respectively<sup>161</sup>, ethyl levulinate represents only one potential product of biomass pyrolysis. The effects of the transition metals on “real” (heterogeneous) biomass thermochemical conversion remain poorly understood. Two important factors in determining a transition metal's effectiveness are its ability to catalyze vapor phase reactions (i.e. reactions happening to lightweight volatiles in the gas stream), and reactions at the solid-vapor interface (i.e. devolatilization, primary decomposition, or the formation of biochar). Recondensation at the solid-vapor phase boundary is responsible for the redeposition of

tar onto the biochar, however fragmenting tar compounds already in the vapor phase have the potential to drastically alter the composition of the recondensing bio-oil<sup>162</sup>.

This chapter explores the effects of two catalyst placement scenarios on biomass pyrolysis: 1) *in situ*, by mixing the biomass and catalyst together directly (through a wet-impregnation pre-treatment) and 2) *ex situ*, using the same pre-treatment method to place the catalyst on a non-reactive substrate (alumina) downstream of the biomass such that the pyrolysis vapors flow over the catalyst at temperature. Pairing data from the pyrolysis products resulting from downstream upgrading (referred to as *ex situ*) and the biomass-catalyst mixture (referred to as *in situ*) can help to untangle the effects of the catalyst on the pyrolysis process to produce bio-oil with a lower oxygen content. To achieve this goal, cherry pits were used as a model biomass feedstock<sup>163–165</sup> because they represent a large untapped potential resource with nearly four million tons produced globally in 2020<sup>166</sup>. In the U.S., cherry pit production reached 400,000 tons annually<sup>167</sup> with the majority processed by a single facility in the Great Lakes region, concentrating the cherry pits in one location<sup>165</sup>. By utilizing concentrated waste streams, the conversion of biomasses into bio-oil via pyrolysis presents a promising valorization route due to reduced transportation cost and increased consistency of feedstock.

## 6.1 Experimental Methods and Materials

American tart cherry pits (*prunus cerasus*) were supplied by the Great Lakes Packing Company in Kewadin, MI, where they are dried onsite at 120 °C for one hour and stored in bulk in grain silos. Once received at Cornell University, the cherry pits were washed with deionized water, dried at room temperature, and ground and sieved to 1-2 mm (with brass ASTM sieves). While it

would be impractical to wash a dry biomass prior to pyrolysis, samples were washed to ensure as homogeneous a sample as possible to enhance reproducibility.

### **6.1.1 Catalyst Preparation**

Four metal acetate compounds (copper, manganese, nickel, and zinc) were sourced from Sigma Aldrich as outlined in section 4.1. with a nearly identical wet impregnation method. The loose cherry pits and alumina fibers (compared to the single-piece cellulose filter paper) necessitated a few modifications. Six grams of cherry pits were soaked in a 50mL milli-q water (18.2 m $\Omega$ ·cm/25 °C) containing 0.05M of each metal acetate for one hour, with an additional 6 g soaked for duplicate pyrolysis runs. Excess water was removed via vacuum filtration, and samples were dried at ambient room conditions for 48 hours. As an experimental control for *in situ* experiments, and to provide sample for *ex situ* experiments, cherry pits were soaked in milli-q water with no metal acetate present. To synthesize the *ex situ* catalysts, 50 mL of 0.05M solutions of the same metal acetates detailed above were contacted with 0.3 grams of alumina oxide wool fibers (Merck 142844-00-6) for one hour. The alumina fibers were dried at ambient conditions for 48 hours, with enough sample produced for duplicate runs of each metal.

### **6.1.2 Pyrolysis and Bio-oil Generation**

The same pyrolysis setup outlined in section 4.1 was used for this work, with the same nitrogen flow rates, heating rates, but with a slightly different oil recovery system. These differences, largely concentrated in the glassware used, helped recover more oil compounds and prevent premature condensation. These differences are highlighted in Figure 6.1 with details on the downstream catalyst placement.

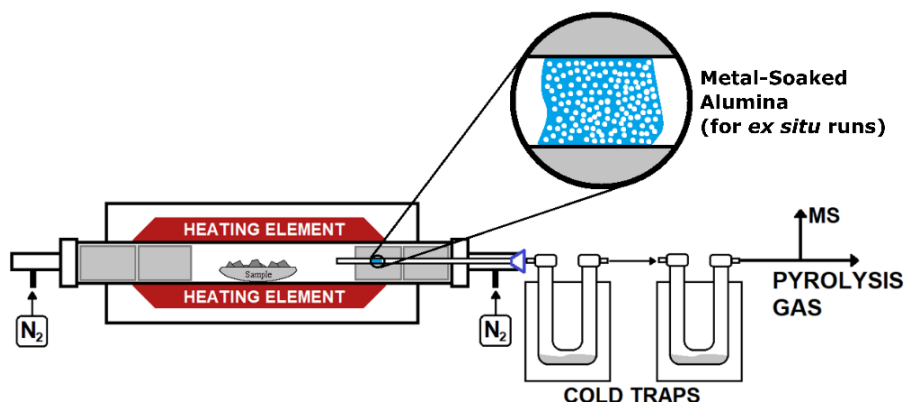


**Figure 6.1** Pyrolysis flow diagram and location of transition metals

For *in situ* catalysis runs, approximately 1.5 grams of wet-impregnated sample was placed in a porcelain combustion boat in the furnace. For *ex situ* catalysis, 1.5 grams of control cherry pit sample (water-soak only) were placed in the porcelain combustion boat, with 0.15 grams of metal-soaked alumina fibers placed in a narrow vapor outlet downstream of the sample in the exhaust gas path. The alumina was set 5 cm back from the outlet to ensure minimal backflow after the pyrolysis gases contacted the alumina, and the alumina was stretched over a 3 cm section of the pipe to ensure the same packing density of the fibers across all runs. The alumina is still contained within the furnace, as seen in the diagram in Figure 6.1, and still experiences the same furnace temperatures as the pyrolyzing sample. The *ex situ* experiments have no direct contact between the biomass solid and catalyst. Only material volatilizing and leaving the biomass sample in the gaseous phase contacts the catalyst.

### 6.1.3 Bio-oil extraction and GC-MS Analysis

Bio-oil was extracted from the cold traps using dichloromethane as outlined in section 4.1, with the same GCMS methodology and instrumentation. However, the GC-MS was calibrated with 26 marker compounds that are common to the pyrolysis of lignocellulosic biomass (detailed in

Appendix C). All peaks were normalized to the mass of biomass feedstock used. Due to the large number of compounds and varied nature of bio-oil composition, calibrating for every compound is infeasible. Instead, the GC-MS was calibrated with the 26 marker compounds identified in supplemental information, utilizing a 5-point calibration with concentrations ranging from 10 PPM to 1500 PPM depending on the compound's relative presence. Approximately 0.02 to 200 mg of each solid compound was weighed on a Sartorius microbalance ( $\pm 0.1 \mu\text{g}$ ) and dissolved in 2.0 mL of DCM ( $\pm 0.1 \mu\text{L}$ ). Bio-oil compounds that were not calibrated for directly were semi-quantitatively analyzed by matching to their closest calibrated neighbor based on mass and number/type of functional groups. Compounds that did not match closely to the calibration list were excluded from the semi-quantitative analysis.

### **6.1.5 Biochar Ultimate Analysis**

The biochars were analyzed in triplicate on a CE-440 elemental analyzer from Extorr Analytical to determine carbon, hydrogen, and nitrogen content directly, with oxygen by subtraction. This method followed ASTM 5373-21. The calibration of the CE-440 analyzer was performed by measuring the carbon, hydrogen, and nitrogen content of 1.8 mg acetanilide ( $\geq 99.99\%$ , Lot# 0240-1121, Exeter Analytical) at 650 °C and 980 °C. This calibration yielded 21.16%  $\pm$  0.08% carbon, 66.30%  $\pm$  2.75% hydrogen, and 7.50%  $\pm$  0.22% nitrogen, representing a measurement accuracy of 0.3%. The calibration factor calculations were performed directly by the CE440 software provided by the manufacturer.

## 6.2 Results and Discussion

The pyrolysis of cherry pits with *in situ* and *ex situ* catalysts yields liquid, solid, and gaseous products. By analyzing the changes in composition of these three phases, we can determine the extent of the effectiveness of both type and location of the catalysts.

### 6.2.1 Product Yields

The effects of *in situ* and *ex situ* transition metal catalysts on product formation are initially captured by the yield of oil, non-condensable gases, and biochar as a percentage of the input mass. This distribution can be seen in Figure 6.2, with downstream or *ex situ* catalytic experiments marked by ‘alumina’. A statistically significant decrease is observed for the bio-oil yield (unpaired two-tailed t-test,  $p = 0.0344$ ) of nearly 8% between the control and metal-containing samples (both *in situ* and *ex situ*). This result is consistent with literature<sup>168–170</sup>, and is likely indicative of the catalysts’ ability to fragment pyrolysis bio-oil compounds into smaller,

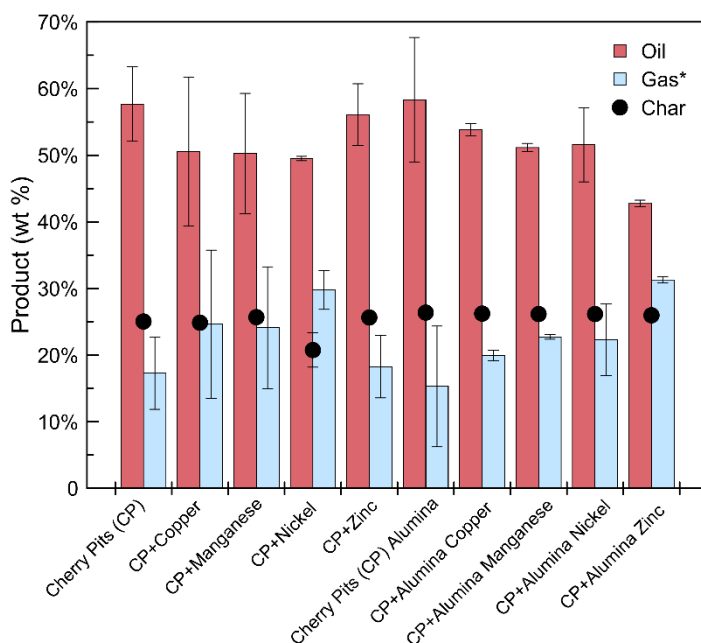


**Figure 6.2** Product yields expressed as a weight percentage. \*Gas yields calculated by difference

non-condensable species that partition into the gas phase. Conversely, the biochar yield remains largely unchanged across samples, except for a *in situ* nickel that shows biochar yields around 25% (error bars are present, but only visible for CP+Nickel). With no statistically significant change in biochar yield (unpaired two tailed t-test,  $p = 0.7140$ ) and limited changes to the yields of oil and gas phases, any catalytic effect must be observed through the chemical composition of each product phase.

### 6.2.2 Pyrolysis Bio-oil Composition

Utilizing GC-MS to identify and quantify the bio-oil compounds allows for the tracing of functional groups as a function of catalyst. With concentrations represented in parts per million, the number of each type of functional group, and concentration of oxygen, hydrogen, and carbon can be calculated. Figure 6.3 highlights the oxygen content of the bio-oil across *in situ* and *ex situ* samples. There is an increasing trend in overall oxygen content with the inclusion of

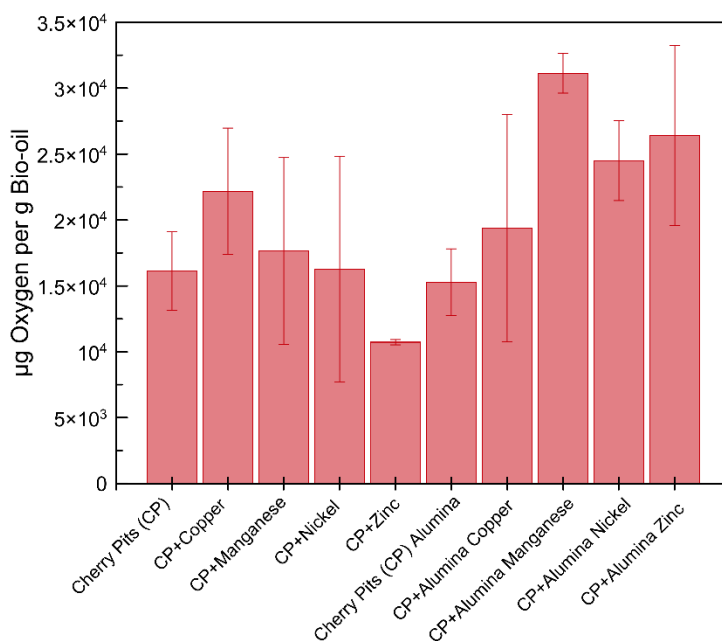


**Figure 6.3** Oxygen content of bio-oils

transition metal catalysts, both *in situ* and *ex situ* with the exception of *in situ* zinc. The value of higher quantities of oxygen is dependent on both their concentrations (relationships to hydrogen and carbon) and what form they take (i.e. functional groups). An initial observation of increased oxygen may seem problematic until it is put into context. Figure 6.4 breaks down the oxygen content of the bio-oils into functional groups. Because the mass of different functional groups changes, comparing on a mass basis overrepresents heavier groups. Instead, the whole number of functional groups was determined.

To generate an improved bio-oil, reducing oxygen-containing functional groups is desirable, with exceptions for fuel-necessary components such as alcohols<sup>171,172</sup>. The relationship of functional groups within the bio-oil remains relatively consistent across all samples. Ethers and alcohols account for the majority of oxygen-containing functional groups, with carboxylic acid representing an almost negligible quantity. Despite the oxygen content, if alcohol-containing

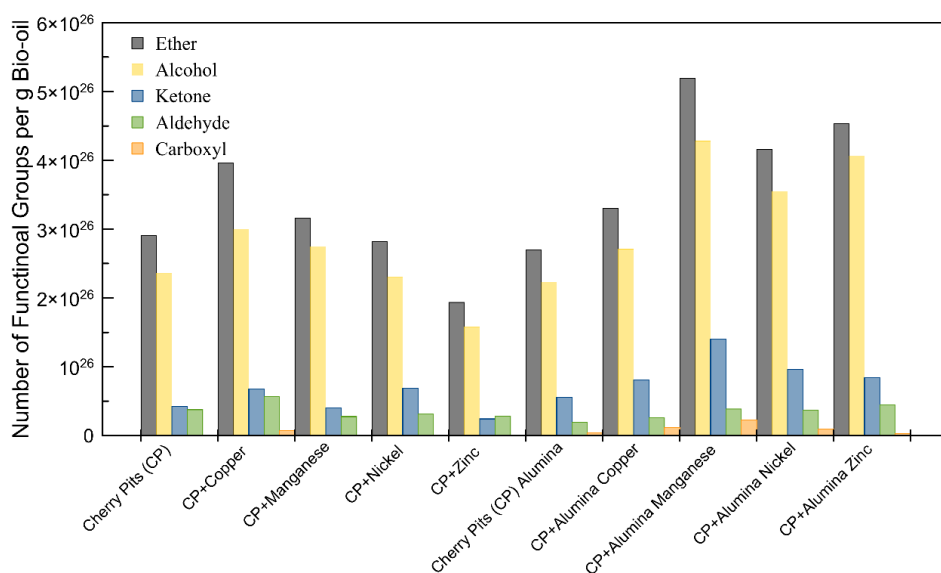


**Figure 6.4** Bio-oil functional group concentrations

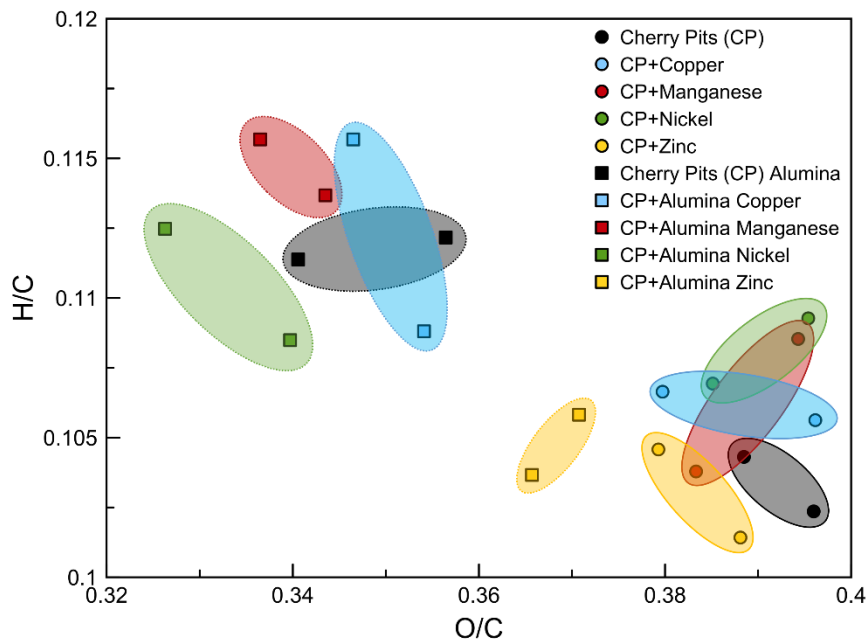


**Figure 6.5** Bio-oil Van Krevelen diagram

compounds are targeted, manganese and alumina generate the highest quantities. Furthermore, placing the oxygen content and functional groups into the context of H/C and O/C ratios provides further insight to the quality of the oil generated. Figure 6.5 illustrates the Van Krevelen diagram for the bio-oil. The Van Krevelen diagram for bio-oil was generated by quantifying the compounds present, and using their total hydrogen, carbon, and oxygen counts to develop the O/C and H/C ratios. This analysis therefore represents the entire composition of the oil and is not limited to functional groups.

Each duplicate set of runs is represented by a pair of circular or square data points, inside a shaded region to show their general trend. All the alumina-metal mixtures (represented by the square data points) have reduced the O/C ratio, and most have improved the H/C ratio. Despite

the increase in oxygen from Figures 6.4 and 6.5, there is an even greater corresponding increase in carbon and hydrogen to offset the oxygen increase.

### 6.2.3 Biochar Composition

With decreased O/C and increased H/C ratios in the bio-oil for alumina-metal catalysts, the changes in the solid biochar phase become important indicators of solid vs. vapor phase interactions. Whereas the alumina-metal catalysts are situated downstream and are poised to catalyze the vapor phase, the direct mixing of biomass and metal (in the no alumina cases) has the potential to alter the biomass to biochar conversion. Figure 6.6 highlights the change in composition of the biochar on a van Krevelen diagram. Unlike in the oil phase, the char is not distributed into ‘alumina’ and ‘no-alumina’ regions, but instead is predominantly separated by the transition metal used.

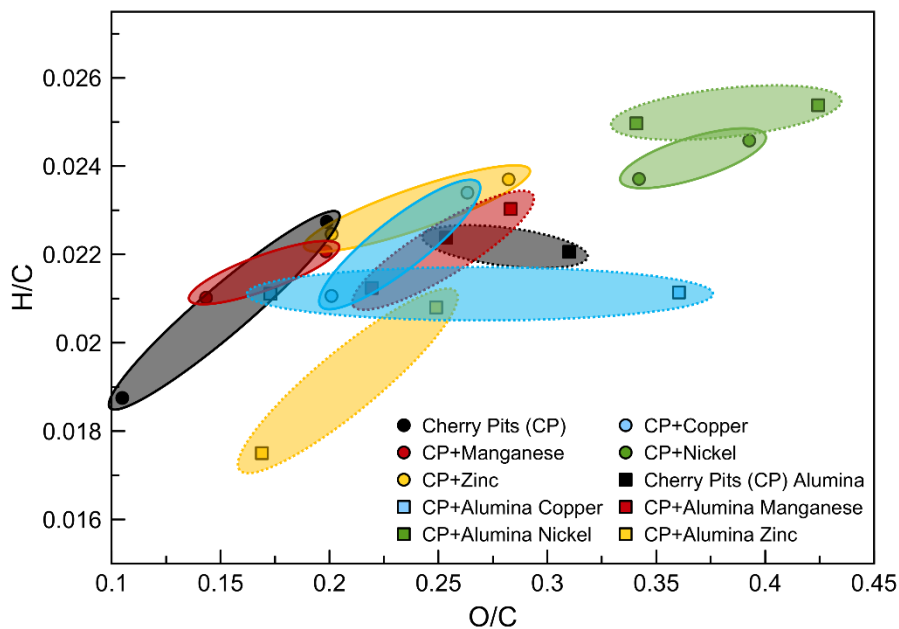


Figure 6.6 Biochar van Krevelen diagram

This indicates that while the alumina influences the oil and gas composition, the effects from the transition metal itself are greater in the resulting biochar. This is expected considering the *ex situ* cases do not allow for the alumina impregnated metal to contact the biochar, and instead affect only the downstream gaseous and bio-oil phases. The samples with *in situ* metals can alter the composition of the biochar, however all the downstream *ex situ* metals would only act on compounds that have entered the gas phase (and have no opportunity to recondense on the biochar). This would indicate that the *in situ* metals' ability to catalyze the overall reaction (in the biochar and bio-oil/gas) is limited when used *in situ*, and has greater opportunity to benefit the resulting oil when placed in the gas stream. The muted effects of the *in situ* metals is potentially due to coking, deactivation, or limits on heat/mass transfer where the metals become unable to interact with the vapor phase.

#### **6.2.4 Non-Condensable Gas Formation**

Carbon dioxide, seen in Figure 6.7, gives a direct measure of oxygen leaving the system.

The *in situ* cases result in mixed outcomes, with nickel generating an increase in CO<sub>2</sub> production by 44%, likely due to the added activity near the 600 °C mark (80-100 minutes). Manganese and zinc see similar increases in CO<sub>2</sub> production (20% and 43% respectively), however copper experiences a slight decrease of 7%. The *ex situ* experiments, where the evolved gas is passed over the alumina-soaked catalyst downstream, yield an altogether larger quantity of CO<sub>2</sub> compared to the *in situ* cases (note the change in axis scaling by nearly an order of magnitude). The inclusion of the alumina oxide – without the addition of transition metals – enhances CO<sub>2</sub> production itself. This is likely due to the improved heat transfer effects on the gas passing through a heated porous material. The alumina possibly provides nucleation sites for the vapor

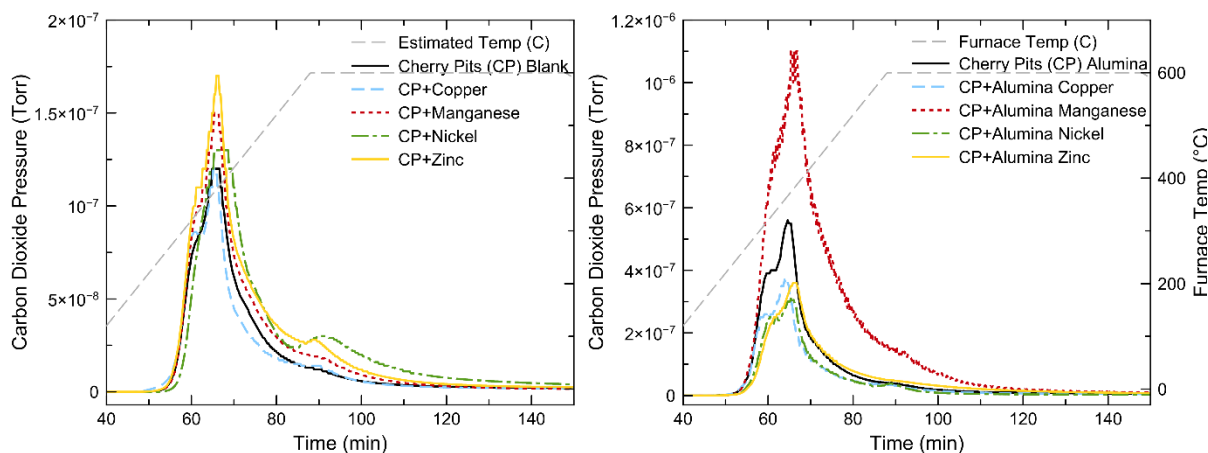


**Figure 6.7** Carbon dioxide formation for *in situ* (above) and *ex situ* (below) transition metal catalysts. Pressure normalized to sample mass.

phase to interact at high temperatures<sup>173</sup>. However, the effects of the inclusion of manganese are magnified greatly by the *ex situ* alumina. Instead of the 20% increase in CO<sub>2</sub> production as seen for Mn versus raw CP *in situ*, the *ex situ* manganese impregnated alumina increases CO<sub>2</sub> production by 148%, or nearly 2.5 times. These trends continue for *ex situ* hydrogen, methane, and ethane, with manganese impregnated alumina generating gases far above the baseline. Various forms of manganese have been used in a wide array of catalytic reactions due to the numerous oxidation states, ranging from the targeting of C-H hydroxylation to assist with the ‘magic methyl effect’<sup>174</sup>, to promoting oxidation of CO waste streams<sup>175</sup>. The concentrations of available oxygen and operating temperature affect the form manganese oxides commonly take as either MnO<sub>2</sub>, Mn<sub>2</sub>O<sub>3</sub>, or Mn<sub>3</sub>O<sub>4</sub><sup>176,177</sup> though more states exist. This variable oxidation state allows manganese to act as either an oxidizing or reducing agent. Despite the inert nature of alumina oxide at temperatures below 1000 °C, some mass loss is expected (manufacturer reports ≤ 5%). Excess oxygen present from the Al<sub>2</sub>O<sub>3</sub> may interact with the manganese to form more productive species than its *in situ* counterpart. Higher oxygen contents and lower temperatures have shown to favor the formation of MnO<sub>2</sub><sup>175</sup> which may account for the difference in activity.

The increased generation of carbon dioxide for the manganese and alumina catalyst is a strong indicator that oxygen is being removed from the bio-oil via decarboxylation, as confirmed by the drop and increase in the O/C and H/C ratio, respectively, in Figure 6.5. By removing the oxygen from the liquid phase, the bio-oil can be fragmented into smaller oil compounds with reduced acidity and instability<sup>178</sup>.

The *ex situ* manganese samples outperform other *ex situ* metals (and *in situ* metals) in the production of hydrogen, methane, and ethane. (Plots of hydrogen, methane, and ethane are available in supplemental information.) Metals used *in situ* generate hydrogen to varying degrees, with copper producing nearly the same amount as the baseline, and manganese, zinc, and nickel producing 50% ( $\pm 6\%$ ), 84% ( $\pm 17\%$ ), 192% ( $\pm 67\%$ ) more hydrogen gas respectively. This increase in hydrogen gas production is advantageous. Hydrogen can be separated and used as its own renewable fuel, either through direct combustion of H<sub>2</sub> gas or fuel cell use<sup>179,180</sup>. Furthermore, this release of hydrogen gas can be indicative of increased fragmentation of the vapor phase, potentially leading to smaller, more desirable, bio-oil compounds (hydrocracking)<sup>181</sup>. Previous studies have shown in other thermochemical reactions, that without a hydrogen donor lignin tends to repolymerize to form more solids via hydrogenolysis of  $\beta$ -O-4 and  $\alpha$ -O-4 bonds<sup>182,183</sup>, adversely affecting bio-oil yield and quality. Additionally, hydrogen can be used in catalytic cracking reactions such as hydrogenation to increase the saturation of compounds, which leads to fuels producing less CO<sub>2</sub> when burned<sup>181</sup>.

### 6.3 Summary

This study examines the effect of using transition metals as catalysts for *in situ* and *ex situ* upgrading to improve the quality of pyrolysis-derived bio-oils. Utilizing transition metal catalysts in both *in situ* and *ex situ* cases demonstrated varying degrees of improvement to bio-oil quality through a deoxygenation mechanism. Specifically, *ex situ* metals lowered the O/C ratio in the bio-oil when compared to *in situ* metals, without drastically altering the composition of the biochar. Manganese-impregnated alumina demonstrated an ability to generate high quantities of pyrolysis gas, specifically H<sub>2</sub>, CO<sub>2</sub>, CH<sub>4</sub>, and C<sub>2</sub>H<sub>6</sub> when placed in the *ex situ* downstream position. By moving the catalyst further from the biomass, an emphasis is placed on improving the vapor phase devolatilization interactions (fragmenting the vapor phase into smaller, non-condensable compounds) instead of heterogeneous surface-gas interactions on the biochar taking place at the solid-vapor interphase. Large, tarry oxygenated compounds that have migrated to the vapor phase (and ultimately recondense in the bio-oil) can be addressed at the same pyrolysis temperature by the *ex situ* downstream catalysts. This gives individual compounds greater opportunity to interact with the catalysts directly, when compared to the bulk biochar and recondensed oil. By limiting when and where these interactions are taking place, we can influence the composition of the bio-oil to a greater degree.

## Chapter 7: Clay Minerals as *in situ* Catalysts for Cherry Pits

The use of clay minerals or layered silicates as biomass pyrolysis catalysts can take many forms and exhibit numerous pathways which provide the desired catalytic effect. The oft-cited cation exchange capacity (CEC) of silicate clays is considered the driving factor of its usefulness<sup>184–186</sup>. Weakly bonded interstitial ions, and ions within the silicate matrices, can be utilized to accept or donate spare electrons to facilitate nearby reactions which might otherwise not occur, or require higher temperatures or input energies<sup>187</sup>. Clay silicates can be treated before use as catalysts to improve or alter their effect. A common treatment for clays is acid washing<sup>188,189</sup>. During acid washing, aluminum (and to a lesser extent magnesium and iron) is removed from the layered matrix, and the natural interlayer cations (such as  $\text{Ca}^{2+}$  and  $\text{Na}^+$ ) are replaced by the freed  $\text{Al}^{3+}$  and  $\text{H}^+$  cations<sup>190</sup>. Additionally, with the weakening of the silicate structure, bends and folds can form to produce mesopores, providing additional physisorption sites<sup>63</sup>. The variability of in charge and physical size of free ions both play important roles in their use. A range of sizes of cations allows for more a specialized fit within exchange sites, ensuring that a variety of reaction pathways have suitable cations to interact with<sup>191</sup>.

Traditionally, the petrochemical industry utilized clay silicates to catalyze cracking and isomerization of petroleum fractions<sup>192,193</sup>, but these were eventually replaced by regenerative zeolites in part due to their thermal stability<sup>194,195</sup>. Ultimately the Lewis and Brønsted acidity was identified as a dominating factor in the catalytic process<sup>196,197</sup>. Brønsted acids have been used to catalyze reactions including the cleavage or formation of esters, ethers, acetals, and cyclic anhydrides<sup>198</sup>. Lewis acids can decompose oligomers<sup>199</sup> (which contribute to tar buildup) and improve the stability of co-catalysts<sup>200</sup>.

To test the effectiveness of silicate clay minerals as *in situ* catalysts, this work utilizes agricultural cherry pit waste (*prunus cerasus*) for the upgrading of pyrolysis bio-oils.

## **7.1 Experimental Materials and Methods**

Cherry pits sourced from the Great Lakes Packing Company were treated and prepared as outlined in section 6.1. To act as the *in situ* catalysts, three layered silicate clays (montmorillonite, attapulgite, and illite) were sourced from Alfa Aesar and Fisher Scientific, and sieved to 150-180  $\mu\text{m}$ . Additionally, apart from a no-clay control, a second control with sand at the same particle sizes and concentration by weight was used. Sand, being unreactive at the temperatures in this experiment, was added to shed light onto the extent to which heat transfer affects the clay-catalyzes pyrolysis.

### **7.1.1 Production of Pyrolysis Bio-oil**

Cherry pits and cherry-clay mixtures were loosely packed into porcelain boats and individually pyrolyzed in a 2 inch electrically heated furnace (MTI) under nitrogen (Parker Balston, >98% purity). Nitrogen was used to purge the system at 100 mL/min, and bio-oil compounds were condensed in dry ice and glycol cold traps for later analysis as outlined in section 6.1.1 – 6.1.2.

## **7.2 Results and Discussion**

The pyrolysis of cherry pits with *in situ* clay mineral catalysts yields liquid, solid, and gaseous products. By examining the changes in yield and composition we can determine the extent of the catalyst's effectiveness.

### 7.2.1 Thermogravimetric Analysis

The devolatilization of cherry pit and clay mixtures at increasing temperatures highlights the minimal role layered silicate clays play in the mass loss regime. Figure 7.1 overlays the mass loss rate of each mixture throughout the pyrolysis process. Little change in either the rate or the peak

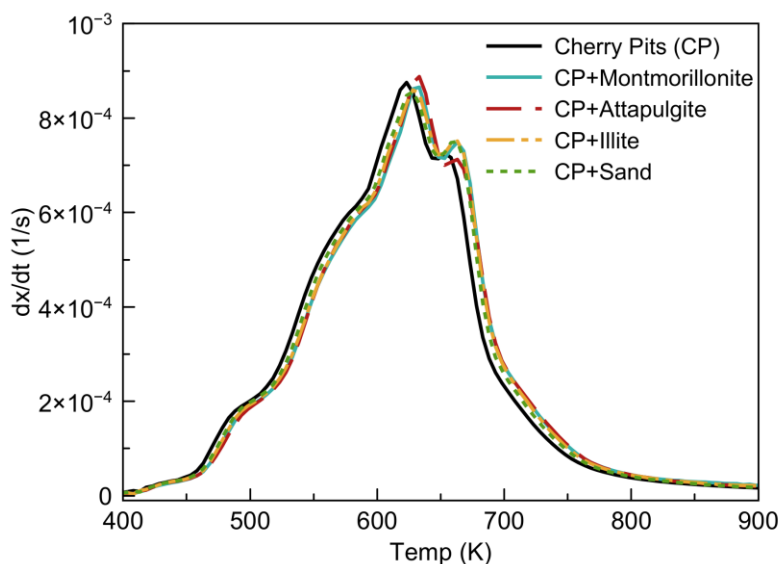


**Figure 7.1** Dry basis derivative thermogravimetric curves for clay-cherry pit mixtures

temperature can be observed, which suggests that the clays do not catalyze the cherry pits by altering the temperature or rate of devolatilization. To understand what effects the clays have on product generation requires scrutiny of the gas and oil phases.

### 7.2.2 Impact of Biomass-Clay Pyrolysis on Product Distribution

Clay catalyzed samples resulted in higher biochar yields, and lower gas yields in three of the four instances. For montmorillonite, attapulgite, and sand, Figure 7.2 shows that less material is lost to the gaseous phase. This leaves more material available to carbonize into biochar or recondense

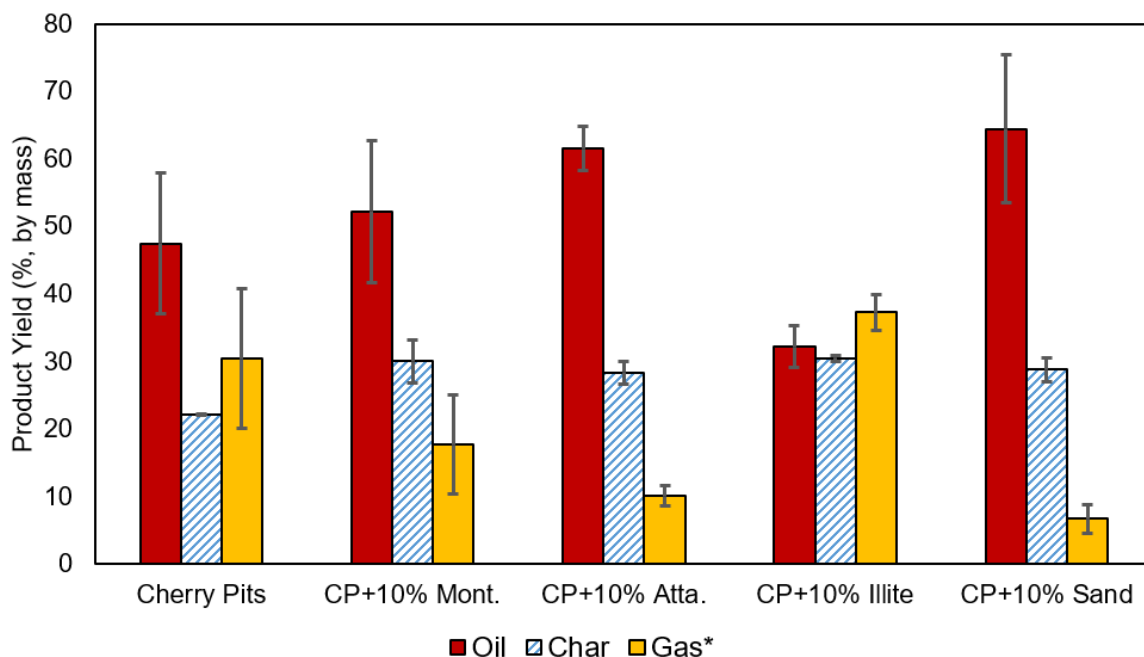


**Figure 7.2** Distribution of product yield for Cherry Pits (CP), Montmorillonite (Mont.), Attapulgite (Atta.), Illite, and Sand

into bio-oil. Typically, maximizing oil yield is an important indicator in the success of the catalysts, however improving the quality of the oil is the penultimate goal. While this work seeks to maximize bio-oil quality and yield, biochar remains an important and useful product as either solid bio-based fuel<sup>201,202</sup>, soil amendments<sup>203,204</sup>, or filtration material in water remediation<sup>205,206</sup>. Sand was used for its lack of chemical catalytic activity to test the heat transfer effects of blending an inactive substance with the biomass. The large change in product distribution indicates sand's strong effect on biochar and non-condensable formation. Previous studies have shown sand to improve graphitization in pyrolyzed sugar<sup>207,208</sup>, with no clear mechanism for the effect.

Despite the decrease in gas evolution for montmorillonite, illite, and sand, the composition and ratio of hydrogen and carbon dioxide reveal how the clay catalysts are affecting the biomass conversion. Figure 7.3 highlights montmorillonite's high hydrogen gas production when compared to the no-clay baseline. This hydrogen production, corresponding decrease in carbon dioxide

formation, and overall reduction in gas formation indicate that montmorillonite promotes dehydrogenation. With less carbon dioxide formation, more carbon is available in the oil and char and may be producing higher degrees of graphitization in the char, or increased alkenes (unsaturated hydrocarbons with C=C bonding) in the bio-oil. Retaining higher degrees of carbon in the oil is beneficial, but depending on how those unsaturated compounds present themselves in the oil phase will ultimately determine the quality of the bio-oil. While illite shows the same trends as montmorillonite (increased H<sub>2</sub> and decreased CO<sub>2</sub> production), illite also produces more gas than the baseline (Figure 7.2). it is therefore not possible to attribute the increase in hydrogen to any change brought about by the catalyst other than a shift in product distribution.

The attapulgite and sand produce both higher hydrogen gas and carbon dioxide (Figure 7.3), however, since the total gas production has decreased substantially, it is difficult to determine the exact of the clay catalyst effect based solely on the gas data.

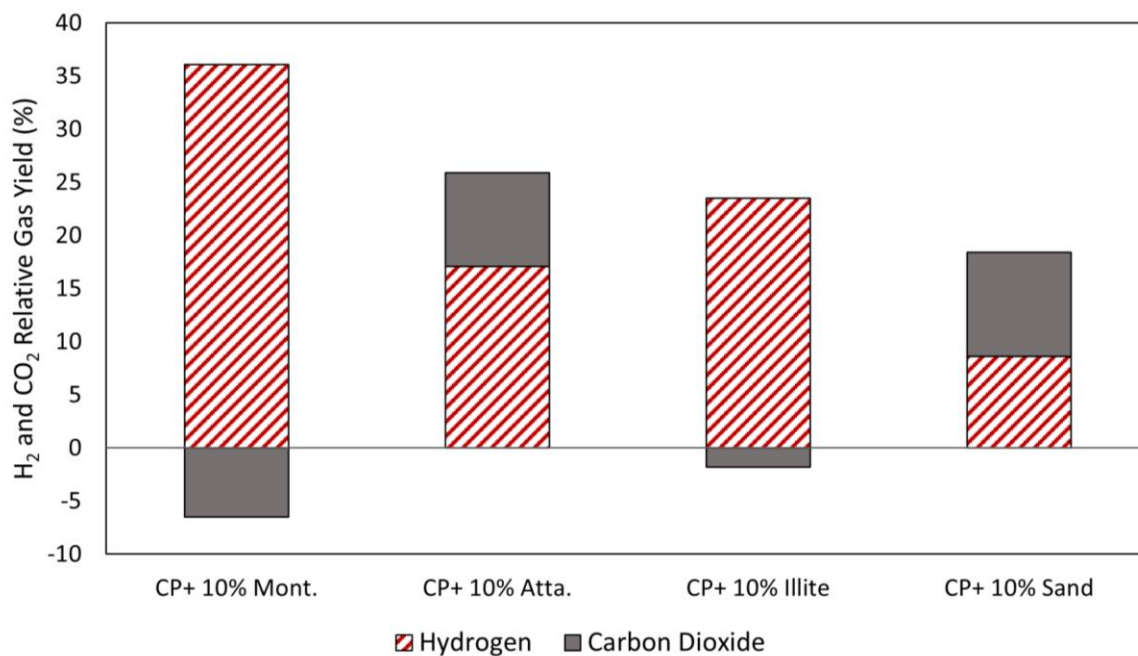


**Figure 7.3** Relative gas yields comparing clay-catalyzed pyrolysis to non-catalyzed pyrolysis (baseline). Abbreviations: Montmorillonite (Mont), Attapulgite (Atta).

### 7.2.3 Influence of Clay on Bio-oil Composition

To gauge the impact of the clays on the bio-oil quality, identified compounds were classified by structure or functional group, with many falling into multiple categories. The results, seen in Figure 7.4, continue to highlight montmorillonite's drastic effects. Coupled with the low CO<sub>2</sub> and high H<sub>2</sub> gas release from section 7.2.2, the bio-oil contains a greater number of alkenes, or unsaturated oil compounds. This results in fewer C-H (~413 kJ/mol) and more C=C bonding (~614 kJ/mol) leading to an increase in fuel energy density, but higher carbon emissions. Additionally, while the removal of many oxygen-containing functional groups within the fuel is desired as they contribute to acidity, increased viscosity and lower stability, alcohol functional groups are beneficial. Ethanol, the most prevalent -OH fuel, is an efficient fuel because the low ratio of C/O reduces the energy density to two-thirds that of gasoline. Montmorillonite increases the number of all

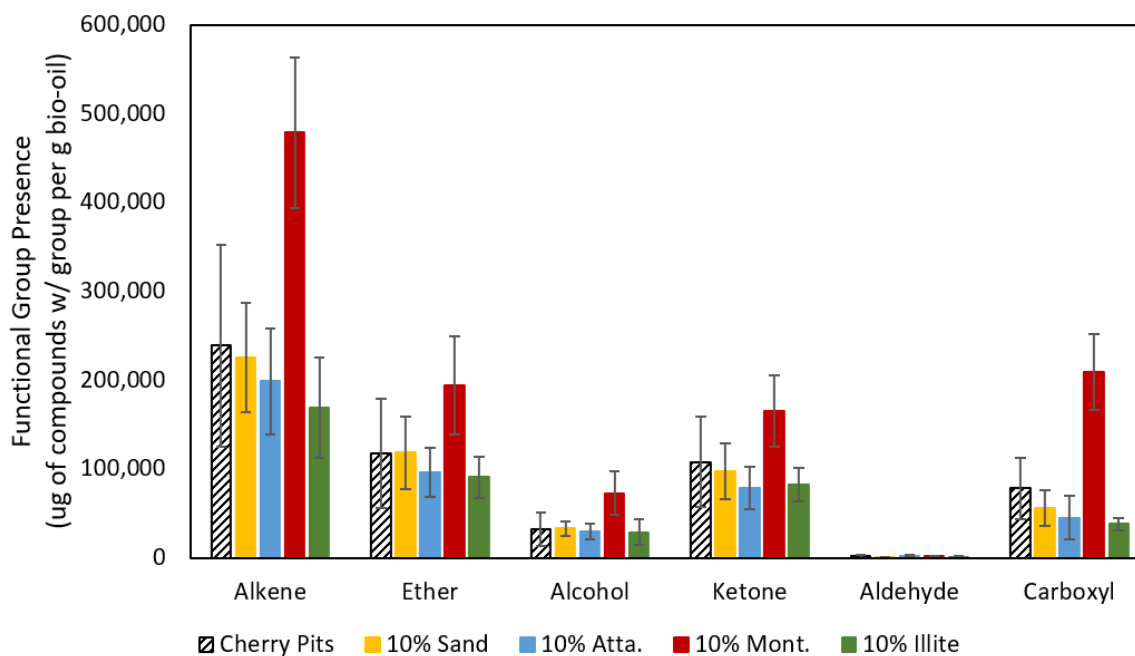


**Figure 7.4** Distribution of functional groups and structures in bio-oil across cherry pit samples. One compound can contain multiple functional groups or structures.

functional groups, excluding aldehydes where the quantities across all samples was comparatively negligible. The C-H bonds near ketone carbonyls tend to be more acidic over their alkane counterparts, contributing to increased corrosive power. The oxygen in ether groups substitutes for a carbon in the compounds structure. Apart from decreasing the energy density, ethers can form peroxides in the presence of oxygen, contributing to both the instability of the fuel, and increased risk of premature combustion. Carboxyl groups, or carboxylic acids, can drastically alter the pH of the fuel. All three of these groups increase polarity and improve solubility in water, which needs to be separated for efficient combustion.

The higher concentration of carboxyl groups in the montmorillonite and cherry pit mix may have influenced the reforming of acids to hydrocarbons. Decarboxylation converts these carboxylic acids into carbon dioxide, which could be a factor in explaining montmorillonite's low CO<sub>2</sub> release<sup>209</sup>. This balance relies on hydrodeoxygenation, which may additionally account for montmorillonite's high H<sub>2</sub> production<sup>210</sup>.

Irrespective of functional group, oxygen is typically used as an indicator of bio-oil quality<sup>211,212</sup>. Figure 7.5 highlights of the cumulative effects of montmorillonite promoting the formation of all functional groups, nearly doubling the amount of oxygen in the bio-oil. In conjunction with The distribution of functional groups outlined in Figure 7.4 and total oxygen in Figure 7.5 are directly tied to the weight of the compounds they are attached to. For example, the relatively high production of carboxyl groups with montmorillonite can be attributed to a higher production of fatty acids in the bio-oil, seen in Figure 7.5 (a full list of the fatty acids can be found in Appendix D). The increased weight of the fatty acids over-represent the carboxyl's role, though it's important

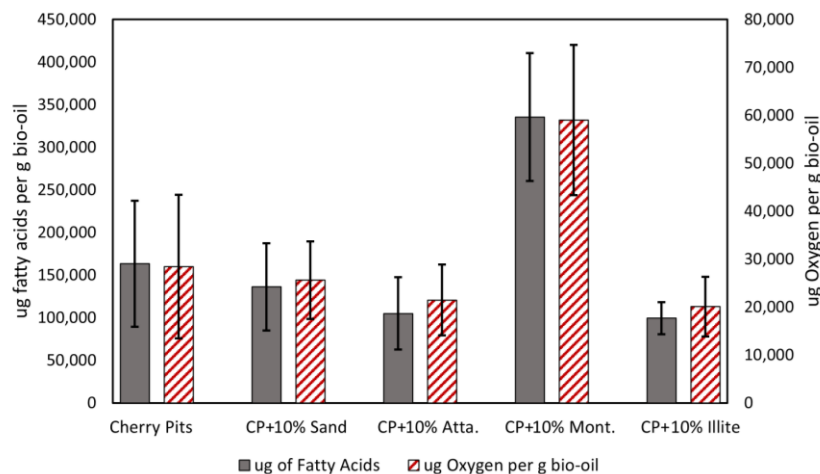


**Figure 7.5** Bio-oil a) oxygen and b) fatty acid concentration

in understanding how the bio-oil can be upgraded to remove these functional groups. The production of fatty acids with montmorillonite is potentially beneficial if the desired product is a biodiesel or biodiesel derivative<sup>213–215</sup>. However, as many industries transition to biofuels by phasing out fossil fuels through “drop-in” transition fuels, biodiesel and long-chain hydrocarbons are ill-suited compared to lighter weight and aromatic oil mixtures<sup>216,217</sup>. Attapulgite, illite, and sand all reduced the number of fatty acids produced and may represent the best option for the “drop-in” renewable hydrocarbon fuels.

In addition to type and quantity of functional groups, the molecular weight of oil compounds is a determining factor of bio-oil quality. Higher weight fuels are more prone to partial combustion and the formation of residues in the combustion chamber<sup>218–220</sup>; reducing the average molecular weight of the oil compounds creates a more combustion-efficient fuel. Figure 7.6 highlights montmorillonite’s drastically higher production of compounds in the 250-300 g/mol range. Many of the fatty acids discussed previously are responsible for this spike. Additionally, montmorillonite generates approximately twice as many compounds in the 100-150 g/mol range – a much more

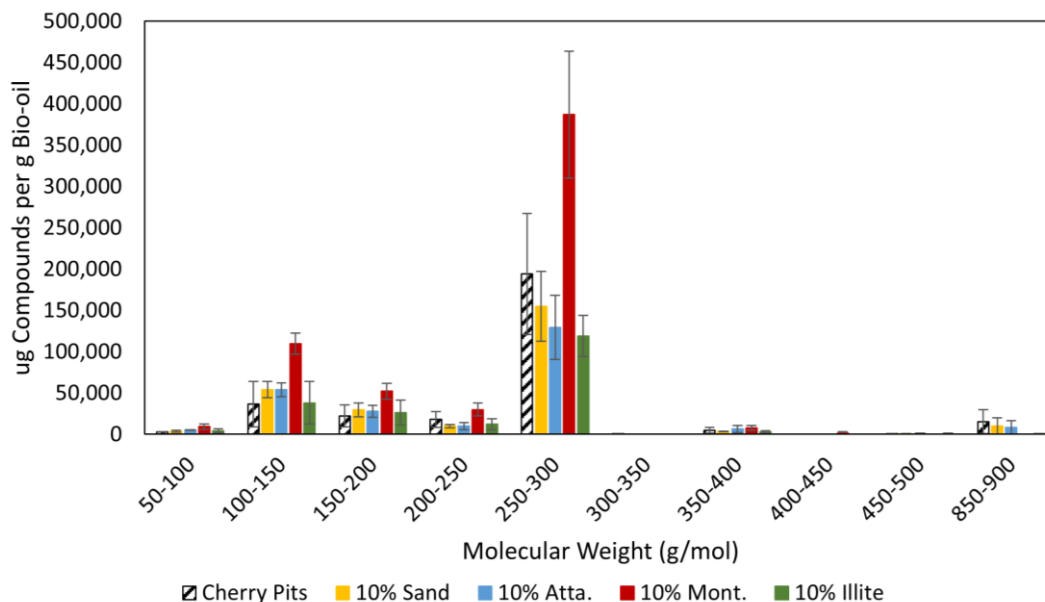


**Figure 7.6** Bio-oil molecular weight

desirable group including benzenes and phenol derivatives. These light aromatics are sought after for their use as fuels<sup>221,222</sup> and starting chemicals for petrochemical industries<sup>223</sup>.

### 7.3 Summary

The current production of thermochemically derived bio-oils from agricultural waste does not substantially address the quality of the oils generated, and the costs of upgrading these oils into usable fuels remains prohibitively high. By upgrading these oils through co-pyrolysis or *in situ* catalytic upgrading, we can drastically alter the composition of the oils in a meaningful way. The inclusion of a 10% mixture of montmorillonite into cherry pits during pyrolysis reduces non-condensable gases lost through the system, decreases saturation to form more energy-dense carbon-carbon bonding, and boosts the generation of a variety of functional groups and light weight aromatics. While some compounds contain beneficial groups (alcohols), others like carboxylic acid pose serious quality control issues. Other clays, such as illite, beneficially reduce unwanted functional groups at the cost of lower yields, and increase non-condensable gas

production. Attapulgite reduced the unwanted functional groups while simultaneously increasing oil yield, but increased compound saturation. Even the addition of sand – unreactive and chemically stable – altered the product distribution through a drastic reduction in non-condensable gas. This is likely due to the increased heat transfer effects sand affords, but the exact mechanism is unknown. Each of these clays has had a unique effect, and through further study it may be possible to select for the desired outcomes by limiting the role the clay silicates play.

## Conclusions

Although the use of lignocellulosic bio-oils to offset our dependence on fossil fuels remains limited, the experiments and analyses in this thesis demonstrate the feasibility of *in situ* and *ex situ* catalytic upgrading with few modifications to the pyrolysis process – and by extension the costs associated with catalyst use. Below are the specific outcomes from this work.

### **1. Catalytic upgrading improves the quality of bio-oil by reducing tar formation.**

When used as *in situ* catalysts, copper and nickel decreased the number of tar compounds present in the cellulose-derived bio-oil at high N<sub>2</sub> flowrate conditions. While this condition might be considered suboptimal when no catalysts are present, the use of catalysts allows for shorter retention times (and higher throughput) without sacrificing bio-oil quality. The beneficial effects are likely due to the high number of oxidation states of copper, and the organic nickel complexes which provide nucleation points for devolatilization reactions to occur.

Manganese, nickel, and copper, when used as *ex situ* catalysts, decreased the O/C and increased H/C ratio of cherry pit bio-oil. The decrease in the amount of oxygen is an indicator of a less acidic and viscous bio-oil, and the higher hydrogen content translates to a more saturated bio-oil, which will produce more water vapor and less carbon dioxide when burned. The change in behavior of the catalysts when moved to the *ex situ* position indicates that these transition metals are more effective at promoting reactions in the vapor phase (or during secondary pyrolysis)

Illite and attapulgite clays reduced the oxygen and fatty acid content of the bio-oil, and montmorillonite promoted the formation of lighter weight compounds (100-150 g/mol) largely in the form of benzene derivatives.

**2. The use of transition metals and clay mineral catalysts can reduce the barriers to pyrolysis devolatilization.**

Apart from the ability to promote devolatilization at the target pyrolysis temperature of 600°C, copper demonstrated a consistent ability to promote earlier devolatilization between 300°C and 400°C. The bio-oil generated at these temperatures contained tar compounds usually not found in cellulose-derived bio-oil until 600°C. By generating these components earlier in the pyrolysis process, copper can be used to generate a crude bio-oil at far lower temperatures, providing biobased fuel makers an option to pyrolyze at less severe conditions.

**3. The location of the catalyst (directly in contact with the solid biomass, or set downstream to act on the vapor phase) plays a substantial role in affecting primary and secondary pyrolysis.**

The difference in behavior of *in/ex situ* catalysts is highly suggestive of how they affect the pyrolysis process. Some *ex situ* catalysts show significant increases in non-condensable gas and bio-oil formation. Since these catalysts are physically removed from the biomass, they cannot be promoting the primary devolatilization and must be promoting secondary pyrolysis, or the re-cracking of tar compounds in the vapor phase. Because the *in situ* catalysts do not see the same degree of non-condensable gas and bio-oil formation, (and they are the same catalysts) they are either unsuited to act on the pyrolysis vapors due to their physical location, potentially become deactivated more quickly through coking, or favorably promote primary pyrolysis when in direct contact with the biomass.

The primary example of this primary vs. secondary effect is *ex situ* manganese. *Ex situ* manganese generated more than double the amount of CO<sub>2</sub>, H<sub>2</sub>, CH<sub>4</sub>, and C<sub>2</sub>H<sub>6</sub> than either the no-catalyst

baseline or the *in situ* manganese trials. Furthermore, all the *ex situ* catalysts lowered the O/C and raised the H/C ratio, suggestive of a more energy dense, less acidic and viscous bio-oil with a higher degree of saturation.

**4. The synergistic behavior and interactions of biopolymers during pyrolysis can be leveraged to beneficially affect and alter the devolatilization process.**

The individual behavior of biopolymers undergoing thermochemical conversion is not additive. The biopolymers do not simply devolatilize without affecting the entire mixture. The use of hemicelluloses (in monomer or polymer form) promotes the devolatilization of lignin at lower temperatures. Derivative thermogravimetric analysis revealed higher than predicted mass-loss peaks for these mixtures below 500°C. Additionally, all lignin containing mixtures saw more hydrogen gas production than could be accounted for by the lignin alone, suggesting the 5- and 6-ring sugars in cellulose and hemicellulose are increasing lignin depolymerization, or vice versa. Potentially the most drastic effect of combining biopolymers comes in the ratio of furans to phenols. Lignin containing mixtures sacrifice furan production in favor of phenols. These deviations from the expected are important to understanding how feedstock selection affects bio-oil and gas products.

The above four outcomes advance our understanding of biomass pyrolysis and the role of catalysts in promoting devolatilization. While the mainstream use of lignocellulosic biobased fuels still lies on the horizon, this work and the field in general continue to move us closer to a viable renewable fuel economy.

## Appendix A

### Supplemental Information for Chapter 3: Synergistic Behavior Among Biomass Biopolymers

Figure A1	Thermogravimetric mass loss regimes for equimass mixtures of lignin+xylose, xylose+xylan, and cellulose+xylose	II
Figure A2	Thermogravimetric mass loss regimes for all equimass mixtures expressed as percent mass loss	III
Figure A3	Thermogravimetric mass loss regimes for all equimass mixtures expressed as $dx/dt$ as a function of time	IV
Figure A4	Pyrolysis gas evolution for biomass mixtures containing xylose	V
Figure A5	Cellulose and xylose bio-oil chromatogram	V
Figure A6	Cellulose and xylan bio-oil chromatogram	VI
Figure A7	Lignin and xylose bio-oil chromatogram	VI
Figure A8	Lignin and xylan bio-oil chromatogram	VII
Figure A9	Xylose and xylan bio-oil chromatogram	VII
Figure A10	Cellulose, xylose, and lignin bio-oil chromatogram	VIII
Figure A11	Cellulose, xylan, and lignin bio-oil chromatogram	VIII

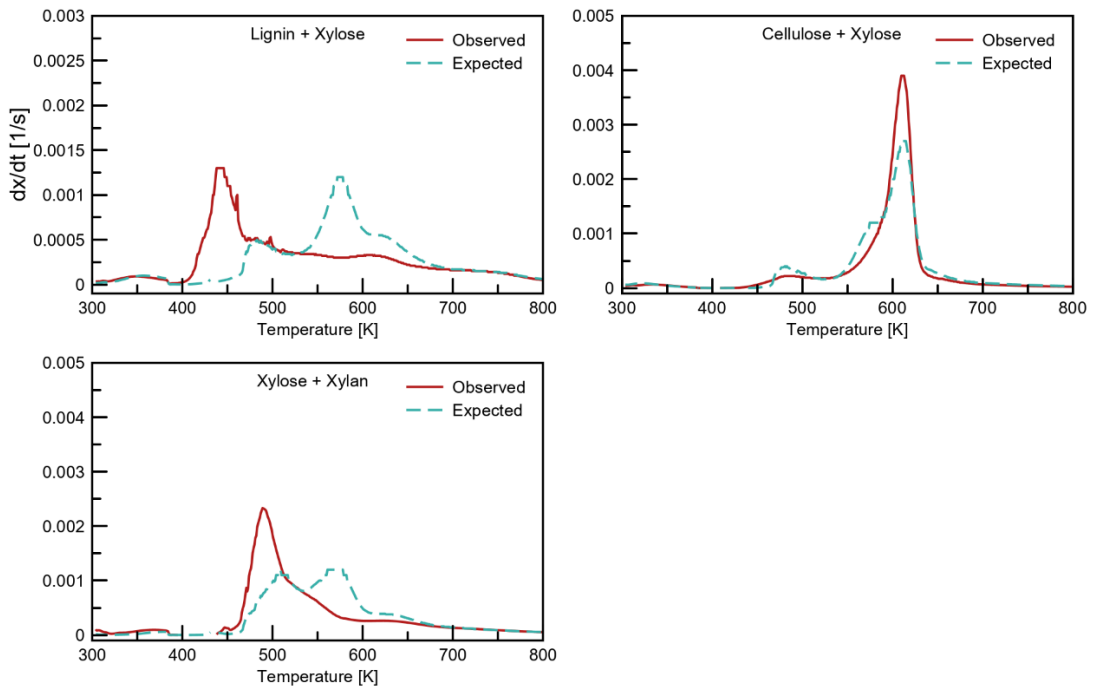


**Figure A1.** Thermogravimetric mass loss regimes for equimass mixtures of lignin+xylose, xylose+xylan, and cellulose+xylose

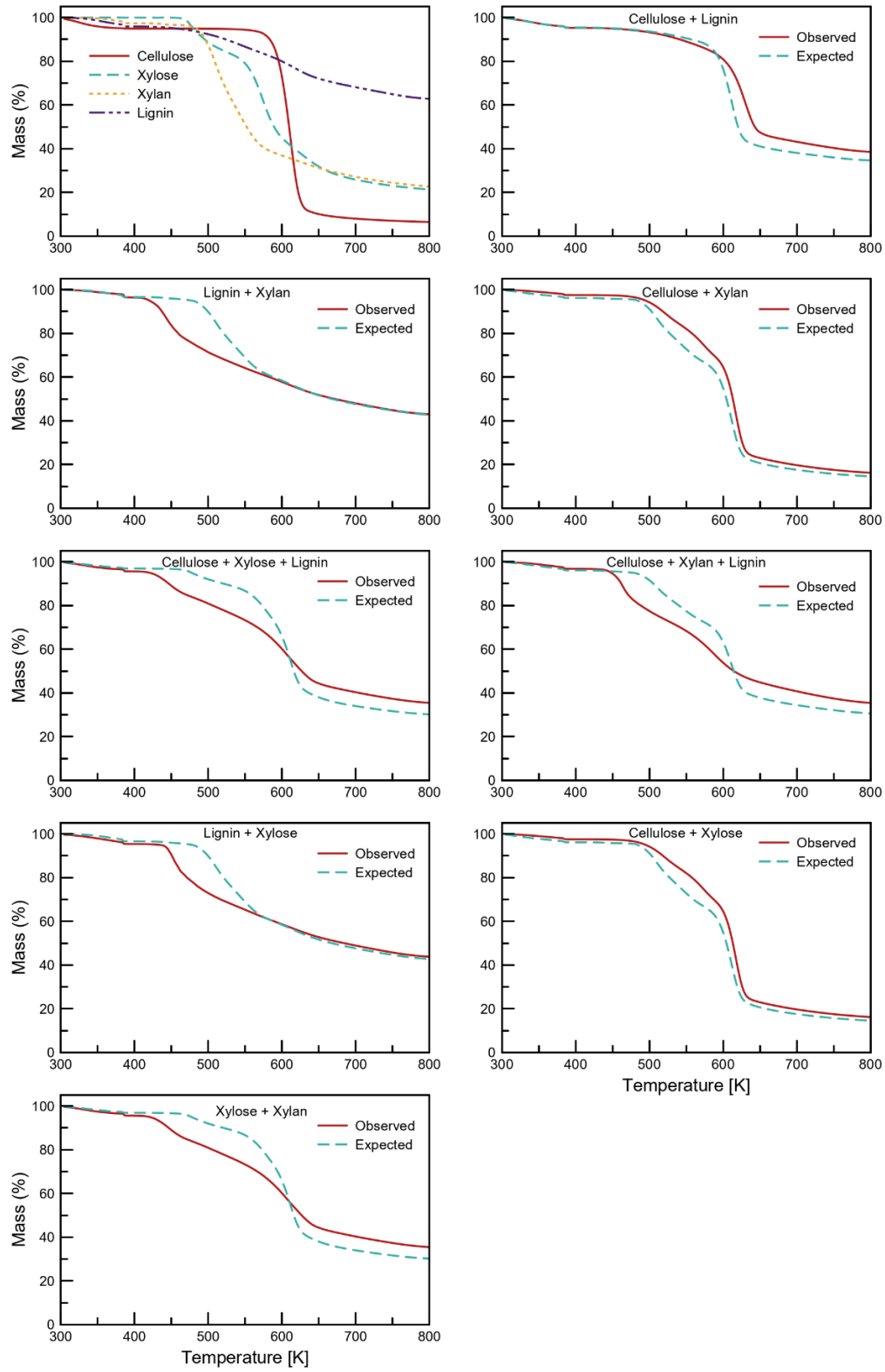


**Figure A2.** Thermogravimetric mass loss regimes for all equimass mixtures expressed as percent mass loss

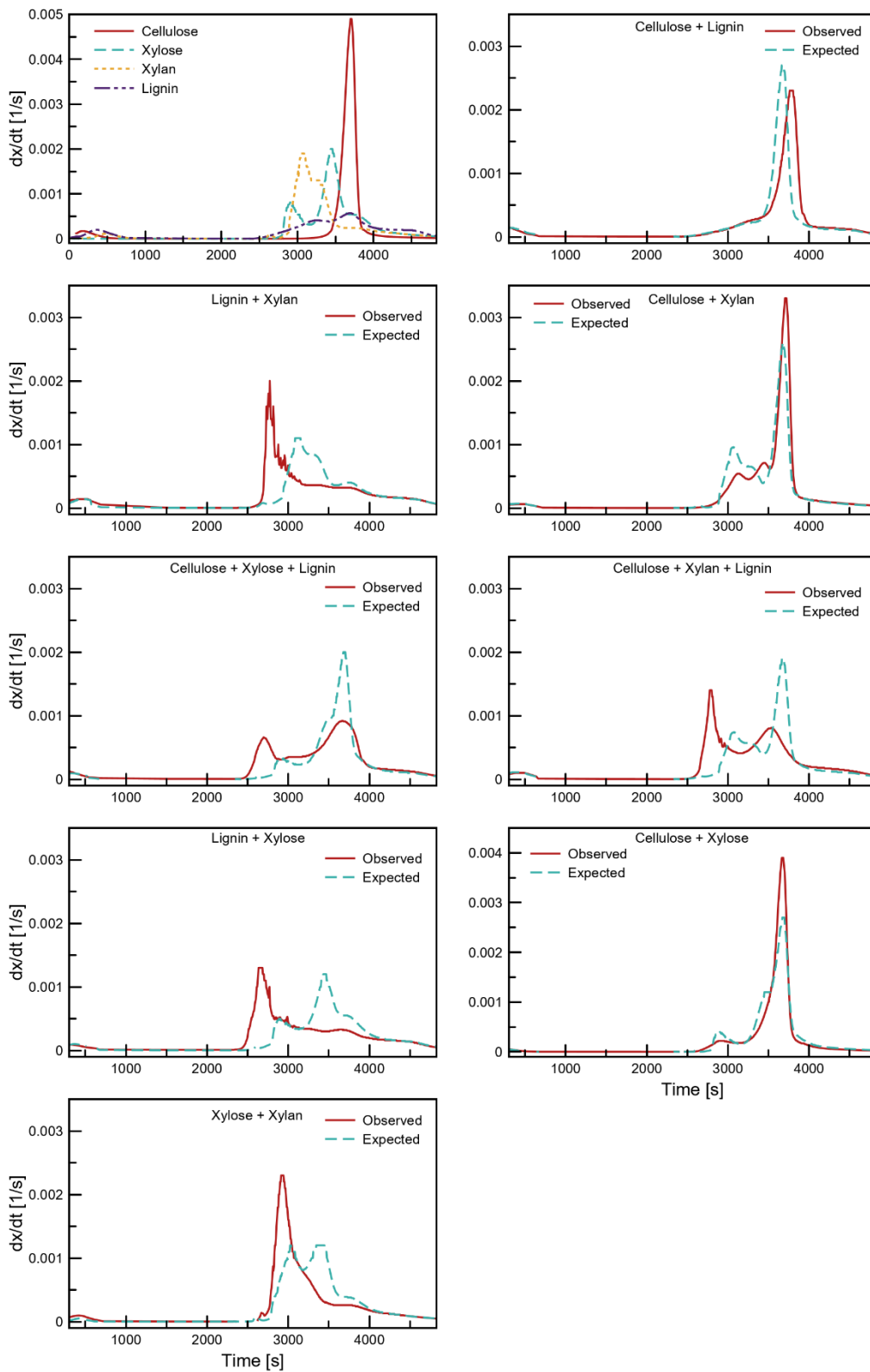


**Figure A3.** Thermogravimetric mass loss regimes for all equimass mixtures expressed as  $dx/dt$  as a function of time

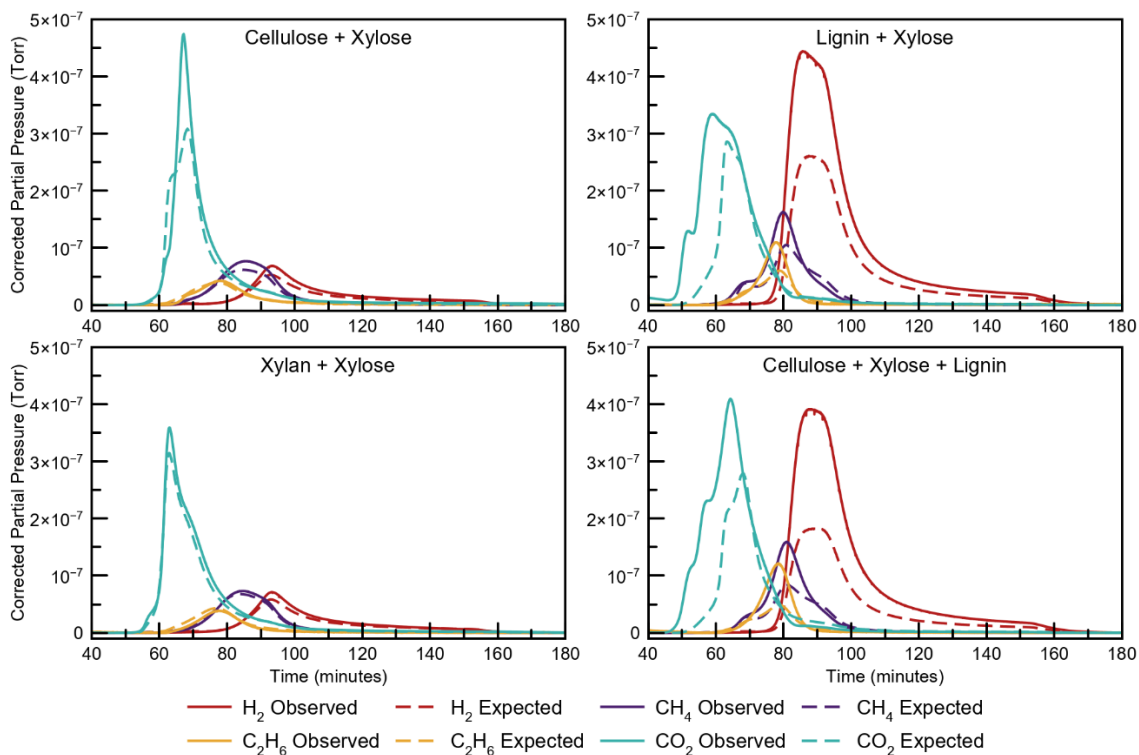


**Figure A4.** Pyrolysis gas evolution for biomass mixtures containing xylose

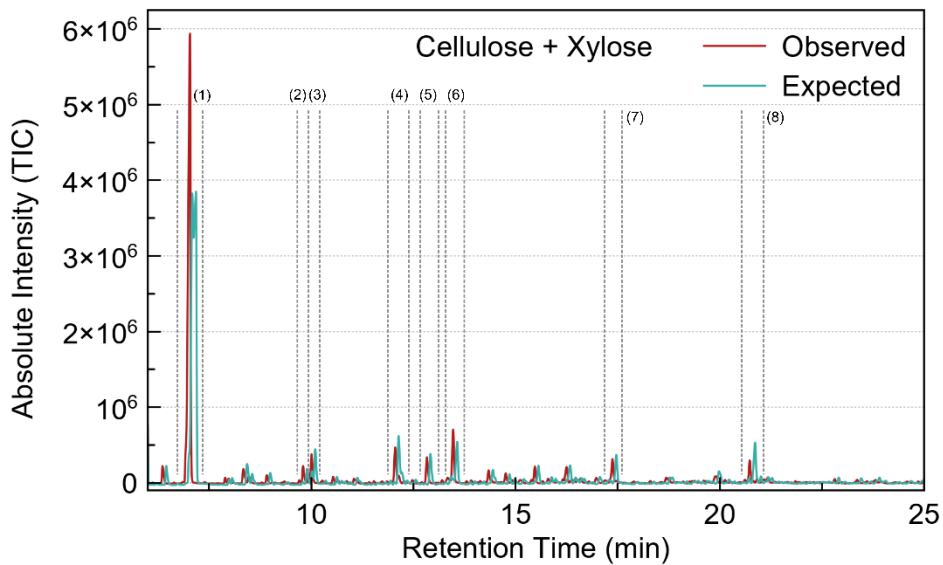


**Figure A5.** Cellulose and xylose bio-oil chromatogram

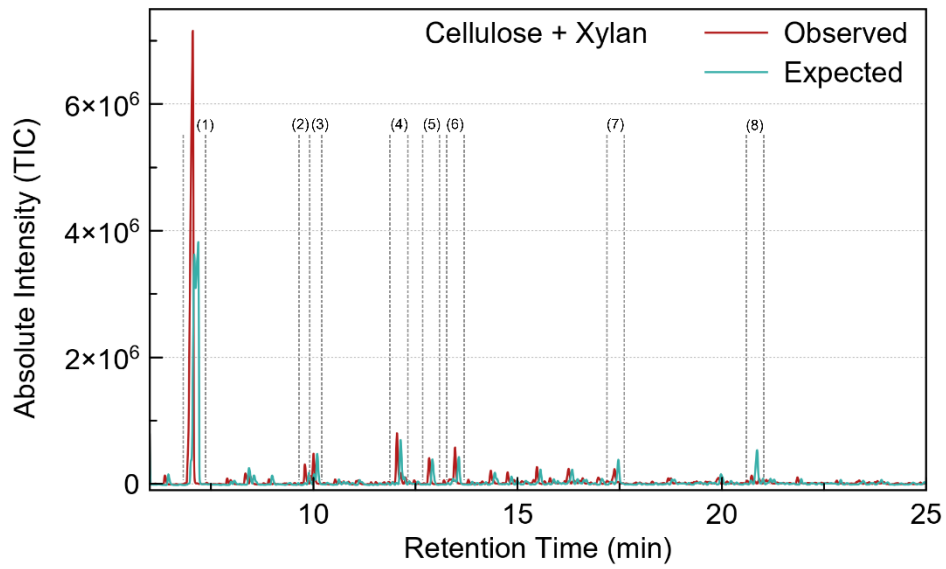


**Figure A6.** Cellulose and xylan bio-oil chromatogram

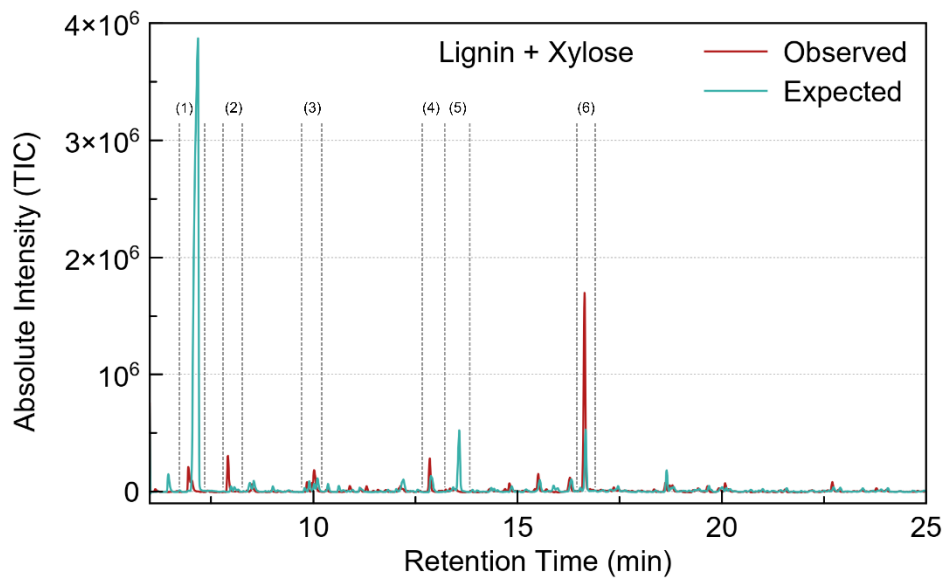


**Figure A7.** Lignin and xylose bio-oil chromatogram

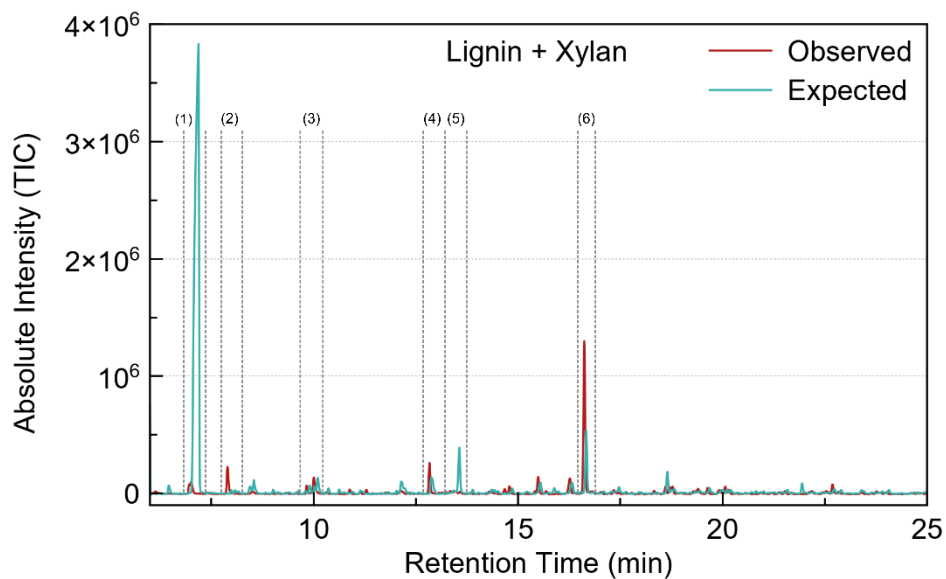


**Figure A8.** Lignin and xylan bio-oil chromatogram

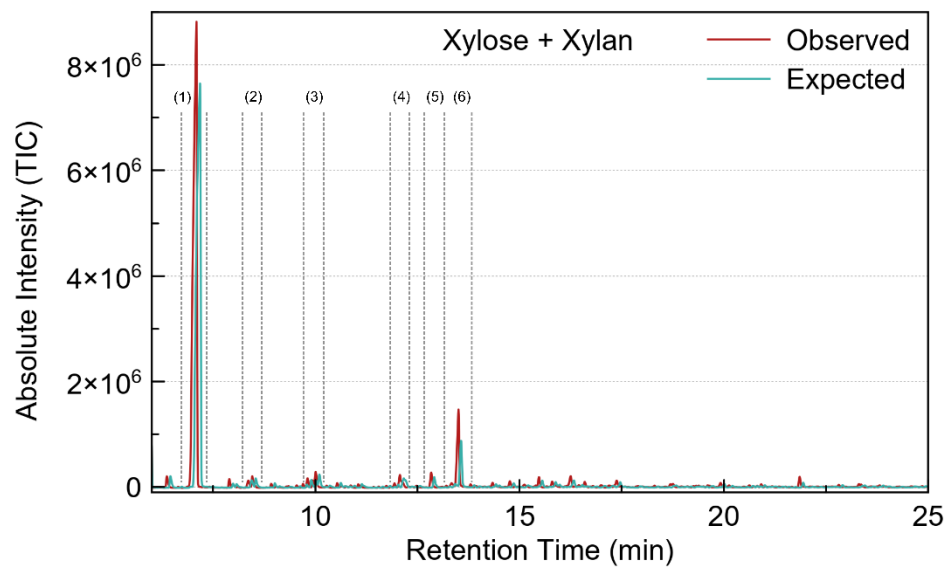


**Figure A9.** Xylose and xylan bio-oil chromatogram

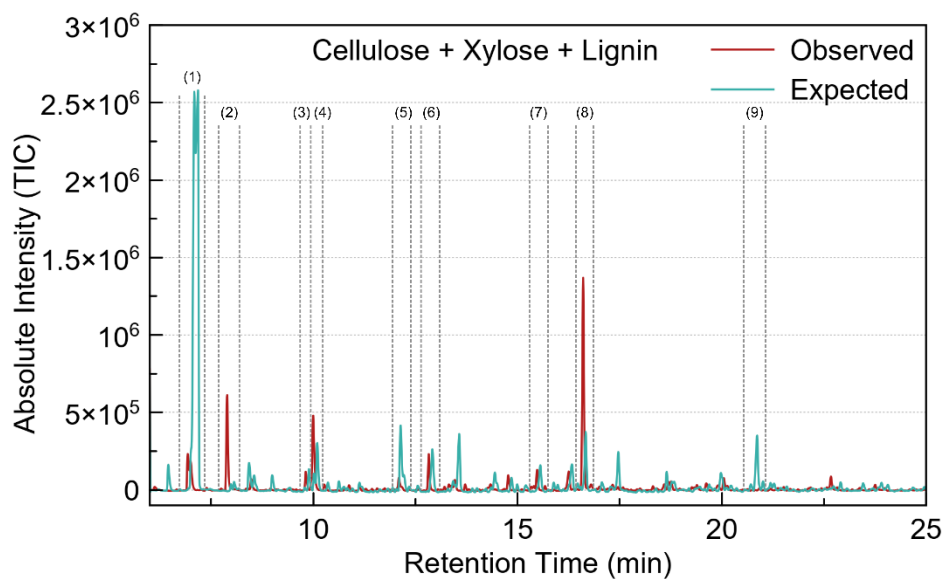


**Figure A10.** Cellulose, xylose, and lignin bio-oil chromatogram

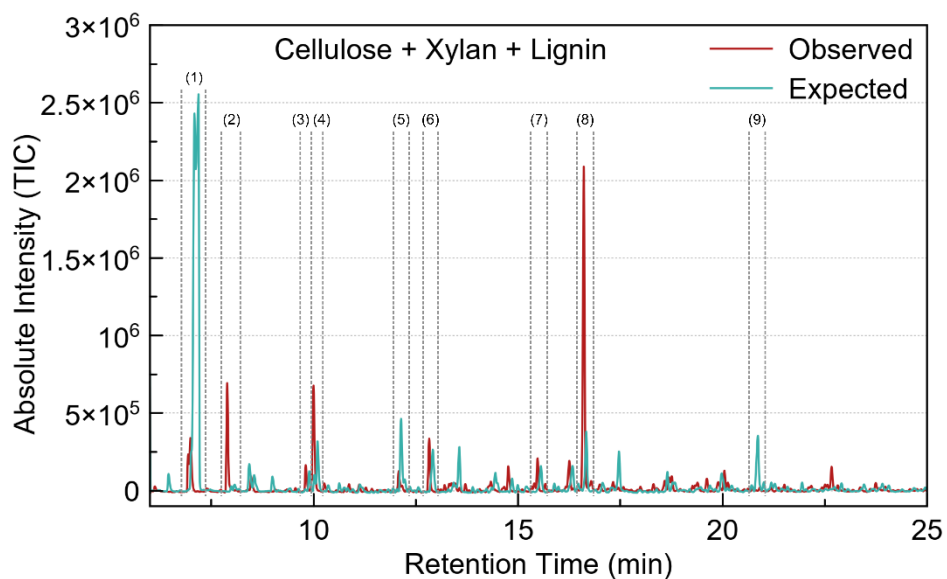


**Figure A11.** Cellulose, xylan, and lignin bio-oil chromatogram

## Appendix B

### Supplemental Information for Chapter 4: Transition Metals as *in situ* Catalysts for Cellulose

Table B1	Carbon dioxide, hydrogen, ethane, and methane gas production values for batch 1 pyrolysis	X
Table B2	Carbon dioxide, hydrogen, ethane, and methane gas production values for batch 2A&2D and 3A&3D pyrolysis	X
Table B3	Carbon dioxide, hydrogen, ethane, and methane gas production values for batch 2B&2E and 3B&3E pyrolysis	XI
Table B4	Carbon dioxide, hydrogen, ethane, and methane gas production values for batch 2C&2F and 3C&3F pyrolysis	XI
Table B5	Average biochar yield at pyrolysis conditions (% of mass input)	XII
Figure B1	Carbon dioxide gas evolution for batches 2 and 2 impregnated cellulose filter papers	XII
Table B6	Group 1 Bio-oil yields as a percent change from the duplicate average blank (no metal) condition	XIII
Table B7	Corresponding compound names and peak numbers for Figures S02 and S03	XIII
Figure B2	Bio-oil chromatograms for batch 1 – labeled with peaks of interest	XIV
Figure B3	Bio-oil chromatograms for batches 2 and 3 – labeled with peaks of interest	XV

**Table B1a.** Carbon dioxide and hydrogen gas production values for batch 1 pyrolysis (corrected for input cellulose)

	Replicate 1B&1E and 1C&1D CO <sub>2</sub> partial pressure average (Torr)	Replicate 1B&1E and 1C&1D CO <sub>2</sub> percent difference between duplicate runs (%)	Replicate 1B&1E and 1C&1D CO <sub>2</sub> percent change in avg. partial pressure as compared to baseline (%)*	Replicate 1B&1E and 1C&1D H <sub>2</sub> partial pressure average (Torr)	Replicate 1B&1E and 1C&1D H <sub>2</sub> percent difference between duplicate runs (%)	Replicate 1B&1E and 1C&1D H <sub>2</sub> percent change in avg. partial pressure as compared to baseline (%)*
Blank (no metal)	2.36E-06	29.3	(baseline)	8.35E-07	6.7	(baseline)
Silver	1.98E-06	3.6	-14.6 to -17.6	1.05E-06	2.7	28.4 to 31.8
Iron(II)	2.27E-06	5.2	-1.3 to -6.3	1.66E-06	10.1	95.9 to 116.8
Copper(II)	2.48E-06	2.1	3.9 to 6.1	1.56E-06	2.6	87.6 to 92.5
Manganese (II)	2.65E-06	6.2	8.5 to 15.5	1.84E-06	3.6	117.0 to 125.0
Nickel(II)	3.40E-06	25.8	25.3 to 62.4	8.38E-06	16.1	851.1 to 1017.6
Zinc	1.96E-06	13.2	-11.4 to -22.4	1.37E-06	5.7	67.0 to 76.8

\*Percent change in average partial pressure as compared to baseline calculated (for all so-reported values in SI) as the percent difference between one metal run and average blank runs, reported as range for duplicate trials

**Table B1b.** Methane and ethane gas production values for batch 1 pyrolysis (corrected for input cellulose)

	Replicate 1B&1E and 1C&1D CH <sub>4</sub> partial pressure average (Torr)	Replicate 1B&1E and 1C&1D CH <sub>4</sub> percent difference between duplicate runs (%)	Replicate 1B&1E and 1C&1D CH <sub>4</sub> percent change in avg. partial pressure as compared to baseline (%)	Replicate 1B&1E and 1C&1D C <sub>2</sub> H <sub>6</sub> partial pressure average (Torr)	Replicate 1B&1E and 1C&1D C <sub>2</sub> H <sub>6</sub> percent difference between duplicate runs (%)	Replicate 1B&1E and 1C&1D C <sub>2</sub> H <sub>6</sub> percent change in avg. partial pressure as compared to baseline (%)
Blank (no metal)	7.00E-07	17.2%	(baseline)	3.36E-06	8.8%	(baseline)
Silver	5.87E-07	8.0%	-12.7 to -19.4	2.69E-06	10.3%	-15.8 to -24.1
Iron(II)	5.55E-07	8.5%	-17.3 to -24.1	2.62E-06	2.2%	-21.1 to -22.8
Copper(II)	7.17E-07	7.5%	-1.3 to 6.4	2.79E-06	19.1%	-8.9 to -24.7
Manganese (II)	6.63E-07	0.2%	-5.2 to -5.4	2.75E-06	8.8%	-14.7 to -21.9
Nickel(II)	4.56E-07	10.4%	-31.5 to -38.2	2.65E-06	18.1%	-13.9 to -28.2
Zinc	5.35E-07	9.9%	-19.7 to -27.3	2.65E-06	5.4%	-19.1 to -23.3

**Table B2a.** Carbon dioxide and hydrogen gas production values for batch 2A&2D and 3A&3D pyrolysis (corrected for input cellulose)

	Replicate 2A&2D and 3A&3D CO <sub>2</sub> partial pressure average (Torr)	Replicate 2A&2D and 3A&3D CO <sub>2</sub> percent difference between duplicate runs (%)	Replicate 2A&2D and 3A&3D CO <sub>2</sub> percent change in avg. partial pressure as compared to baseline (%)	Replicate 2A&2D and 3A&3D H <sub>2</sub> partial pressure average (Torr)	Replicate 2A&2D and 3A&3D H <sub>2</sub> percent difference between duplicate runs (%)	Replicate 2A&2D and 3A&3D H <sub>2</sub> percent change range to baseline (%)
Blank (no metal)	2.16E-06	21.9	(baseline)	8.04E-07	3.3	(baseline)
Copper(II)	2.14E-06	2.2	-2.2 to 0.0	1.83E-06	65.9	52.3 to 202.0
Nickel(II)	2.62E-06	6.3	5.6 to 24.8	4.50E-06	12.0	426.2 to 493.1

**Table B2b.** Methane and ethane gas production values for batch 2A&2D and 3A&3D pyrolysis (corrected for input cellulose)

	Replicate 2A&2D and 3A&3D CH <sub>4</sub> partial pressure average (Torr)	Replicate 2A&2D and 3A&3D CH <sub>4</sub> percent difference between duplicate runs (%)	Replicate 2A&2D and 3A&3D CH <sub>4</sub> percent change in avg. partial pressure as compared to baseline (%)	Replicate 2A&2D and 3A&3D C <sub>2</sub> H <sub>6</sub> partial pressure average (Torr)	Replicate 2A&2D and 3A&3D C <sub>2</sub> H <sub>6</sub> percent difference between duplicate runs (%)	Replicate 3A&3D and 3A&3D C <sub>2</sub> H <sub>6</sub> percent change in avg. partial pressure as compared to baseline (%)
Blank (no metal)	6.16E-07	2.1	(baseline)	2.62E-06	9.8	(baseline)
Copper(II)	7.02E-07	46.5	-12.5 to 40.4	2.91E-06	24.2	-2.2 to 24.8
Nickel(II)	4.26E-07	6.0	-29.4 to -32.8	2.45E-06	4.8	-8.7 to 0.7

**Table B3a.** Carbon dioxide and hydrogen gas production values for batch 2B&2E and 3B&3E pyrolysis (corrected for input cellulose)

	Replicate 2B&2E and 3B&3E CO <sub>2</sub> partial pressure average (Torr)	Replicate 2B&2E and 3B&3E CO <sub>2</sub> percent difference between runs (%)	Replicate 2B&2E and 3B&3E CO <sub>2</sub> percent change in avg. partial pressure as compared to baseline (%)	Replicate 2B&2E and 3B&3E H <sub>2</sub> partial pressure average (Torr)	Replicate 2B&2E and 3B&3E H <sub>2</sub> percent difference between runs (%)	Replicate 2B&2E and 3B&3E H <sub>2</sub> percent change in avg. partial pressure as compared to baseline (%)
Blank (no metal)	1.21E-06	33.5	(baseline)	3.77E-07	25.4	(baseline)
Copper(II)	9.64E-07	10.5	-15.8 to -24.4	5.61E-07	19.9	34.0 to 63.7
Nickel(II)	1.05E-06	18.7	-5.2 to -21.4	1.61E-06	18.9	287.7 to 368.4

**Table B3b.** Methane and ethane gas production values for batch 2B&2E and 3B&3E pyrolysis (corrected for input cellulose)

	Replicate 2B&2E and 3B&3E CH <sub>4</sub> partial pressure average (Torr)	Replicate 2B&2E and 3B&3E CH <sub>4</sub> percent difference between runs (%)	Replicate 2B&2E and 3B&3E CH <sub>4</sub> percent change in avg. partial pressure as compared to baseline (%)	Replicate 2B&2E and 3B&3E C <sub>2</sub> H <sub>6</sub> partial pressure average (Torr)	Replicate 2B&2E and 3B&3E C <sub>2</sub> H <sub>6</sub> percent difference between runs (%)	Replicate 2B&2E and 3B&3E C <sub>2</sub> H <sub>6</sub> percent change in avg. partial pressure as compared to baseline (%)
Blank (no metal)	3.81E-07	11.7	(baseline)	2.55E-06	9.1	(baseline)
Copper(II)	3.08E-07	3.3	-17.7 to 20.4	2.53E-06	0.2	-0.8 to -1.0
Nickel(II)	2.65E-07	7.8	-27.7 to -33.1	2.34E-06	3.7	-6.5 to -9.9

**Table B4a.** Carbon dioxide and hydrogen gas production values for batch 2C&2F and 3C&3F pyrolysis (corrected for input cellulose)

	Replicate 2C&2F and 3C&3F CO <sub>2</sub> partial pressure average (Torr)	Replicate 2C&2F and 3C&3F CO <sub>2</sub> percent difference between runs (%)	Replicate 2C&2F and 3C&3F CO <sub>2</sub> percent change in avg. partial pressure as compared to baseline (%)	Replicate 2C&2F and 3C&3F H <sub>2</sub> partial pressure average (Torr)	Replicate 2C&2F and 3C&3F H <sub>2</sub> percent difference between runs (%)	Replicate 2C&2F and 3C&3F H <sub>2</sub> percent change in avg. partial pressure as compared to baseline (%)
Blank (no metal)	1.61E-06	52.7	(baseline)	1.53E-07	11.0	(baseline)
Copper(II)	1.74E-06	10.8	2.0 to 13.6	4.30E-07	8.3	168.6 to 191.8
Nickel(II)	1.50E-06	24.0	-18.4 to 3.8	2.24E-07	11.0	37.9 to 54.0

**Table B4b.** Methane and ethane gas production values for batch 2C&2F and 3C&3F pyrolysis (corrected for input cellulose)

	Replicate 2C&2F and 3C&3F CH <sub>4</sub> partial pressure average (Torr)	Replicate 2C&2F and 3C&3F CH <sub>4</sub> percent difference between runs (%)	Replicate 2C&2F and 3C&3F CH <sub>4</sub> percent change in avg. partial pressure as compared to baseline (%)	Replicate 2C&2F and 3C&3F C <sub>2</sub> H <sub>6</sub> partial pressure average (Torr)	Replicate 2C&2F and 3C&3F C <sub>2</sub> H <sub>6</sub> percent difference between runs (%)	Replicate 2C&2F and 3C&3F C <sub>2</sub> H <sub>6</sub> percent change in avg. partial pressure as compared to baseline (%)
Blank (no metal)	2.25E-07	2.0	(baseline)	2.45E-06	9.4	(baseline)
Copper(II)	2.34E-07	5.9	1.3 to 6.6	2.47E-06	2.0	0.0 to 2.0
Nickel(II)	2.35E-07	1.4	-1.7 to 10.9	2.43E-06	2.5	-2.0 to 0.5

**Table B5.** Average biochar yield at pyrolysis conditions as a percentage of mass input. Standard deviation reported for values with n>2, otherwise percent difference between the duplicate trials.

	T = 600°C and N <sub>2</sub> = 100ml/min	T = 600°C and N <sub>2</sub> = 200ml/min	T = 350°C and N <sub>2</sub> = 100ml/min
Blank (no-metal)	12.43 ± 0.55	11.46 (14.7%)	17.08 (21.3%)
Copper	14.14 ± 0.91	13.05 (5.6%)	19.83 (0.4%)
Nickel	9.45 ± 1.68	11.67 (5.5%)	20.23 (3.7%)
Silver	13.14 (18.2%)	N/A	N/A
Iron	17.13 (2.6%)	N/A	N/A
Manganese	15.26 (0.4%)	N/A	N/A
Zinc	16.68 (0.5%)	N/A	N/A

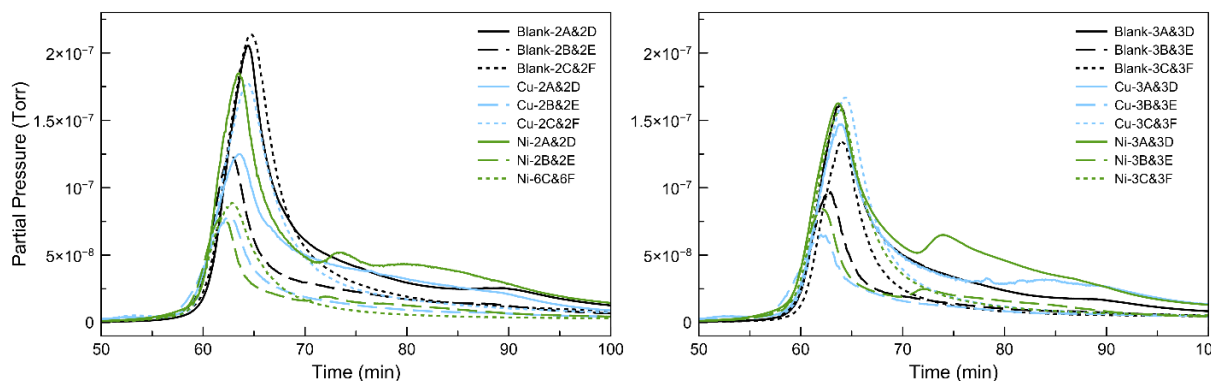


**Figure B1.** Carbon dioxide gas evolution for batches 2 and 3 impregnated cellulose filter papers

**Table B6.** Group 1 Bio-oil yields as a percent change from the duplicate average blank (no metal) condition

	Silver		Iron		Copper		Manganese		Nickel		Zinc	
	Group 1 BE	Group 1 CD										
Furfural	-33.9	-21.3	-2.1	-20.7	-42.3	-38.8	-11.5	-7.2	-27.1	78.0	62.2	59.5
2-Propyl Furan	-25.8	-2.5	-38.5	-72.7	-5.0	-0.6	-63.9	-58.9	-16.4	-24.3	-41.2	-46.4
2(5H)-Furanone	-2.1	1.3	5.6	-100	-43.6	-31.8	93.2	5.3	6.2	32.6	15.2	17.7
1-(2-furanyl)- Ethanone	22.2	48.4	8.4	-35.5	31.8	6.2	-18.9	-44.5	-3.7	-1.6	-13.5	-18.4
3-Hydroxy-2(1H)-Pyridinone	-53.5	-43.6	150.7	-42.9	2.0	-79.7	327.9	-31.4	1101	25.9	-30.9	0.8
5-Methyl-2-Furancarboxaldehyde	-39.7	-13.5	71.6	40.2	-34.6	-27.7	37.1	49.2	48.6	239.8	119.0	184.7
Phenol	16.8	-14.0	-10.6	-47.0	-23.7	-10.8	1.5	-36.7	-10.5	-15.8	-11.0	6.2
3-methyl-1,2-Cyclopentanedione	-11.1	-9.5	125.2	63.1	2.7	14.3	42.0	51.4	22.0	134.0	4.7	42.5
Levogluosenone	49.2	18.8	-13.7	-60.9	78.4	36.4	-26.2	-50.5	-13.3	11.4	0.7	28.0
Heptanal	-74.5	-49.9	81.8	76.0	-69.4	-54.2	-98.0	196.6	43.9	336.4	343.8	549.8
1,4:3,6-Dianhydro- $\alpha$ -D-glucopyranose	-4.4	-11.6	-19.3	-30.1	-13.1	7.4	-37.4	-3.1	-54.9	21.2	-13.5	26.9
1,6-anhydro- $\beta$ -D-Glucopyranose	62.2	-39.7	-38.2	85.5	-74.7	11.5	-62.5	136.4	-85.9	11.1	-78.9	-10.0

**Table B7.** Corresponding compound names and peak numbers for Figures B2 and B3

Peak Number	Compound
1	Furfural
2	2-Propyl Furan
3	2(5H)-Furanone
4	3-Hydroxy-2(1H)-Pyridinone
5	5-methyl-2-Furancarboxaldehyde
6	Phenol
7	3-methyl-1,2-Cyclopentanedione
8	Levogluosenone
9	Heptanal
10	1,4:3,6-Dianhydro- $\alpha$ -D-glucopyranose
11	1,6-anhydro- $\beta$ -D-Glucopyranose

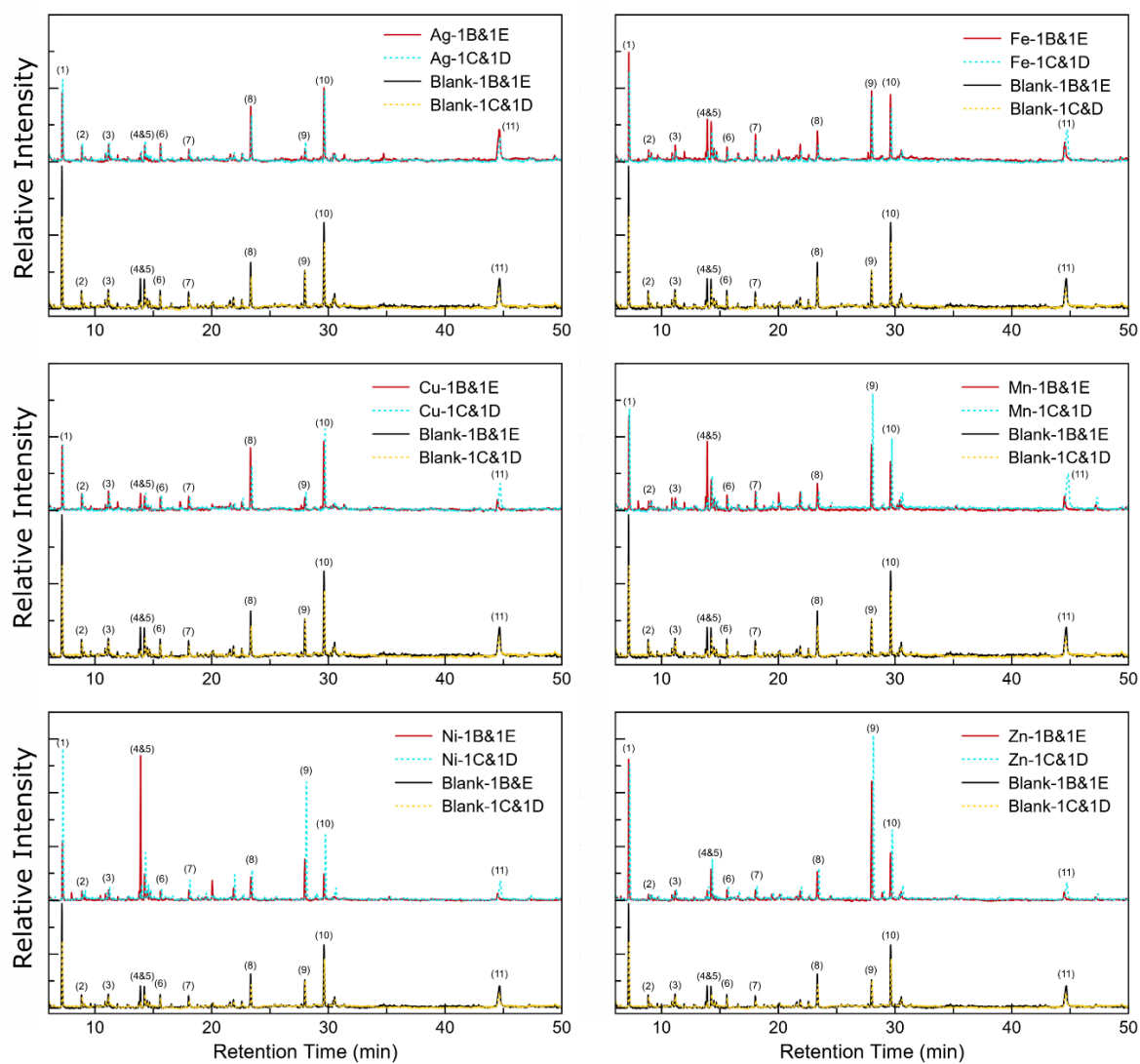


**Figure B2.** Bio-oil chromatograms for batch 1 – labeled with peaks of interest as detailed in Table B6

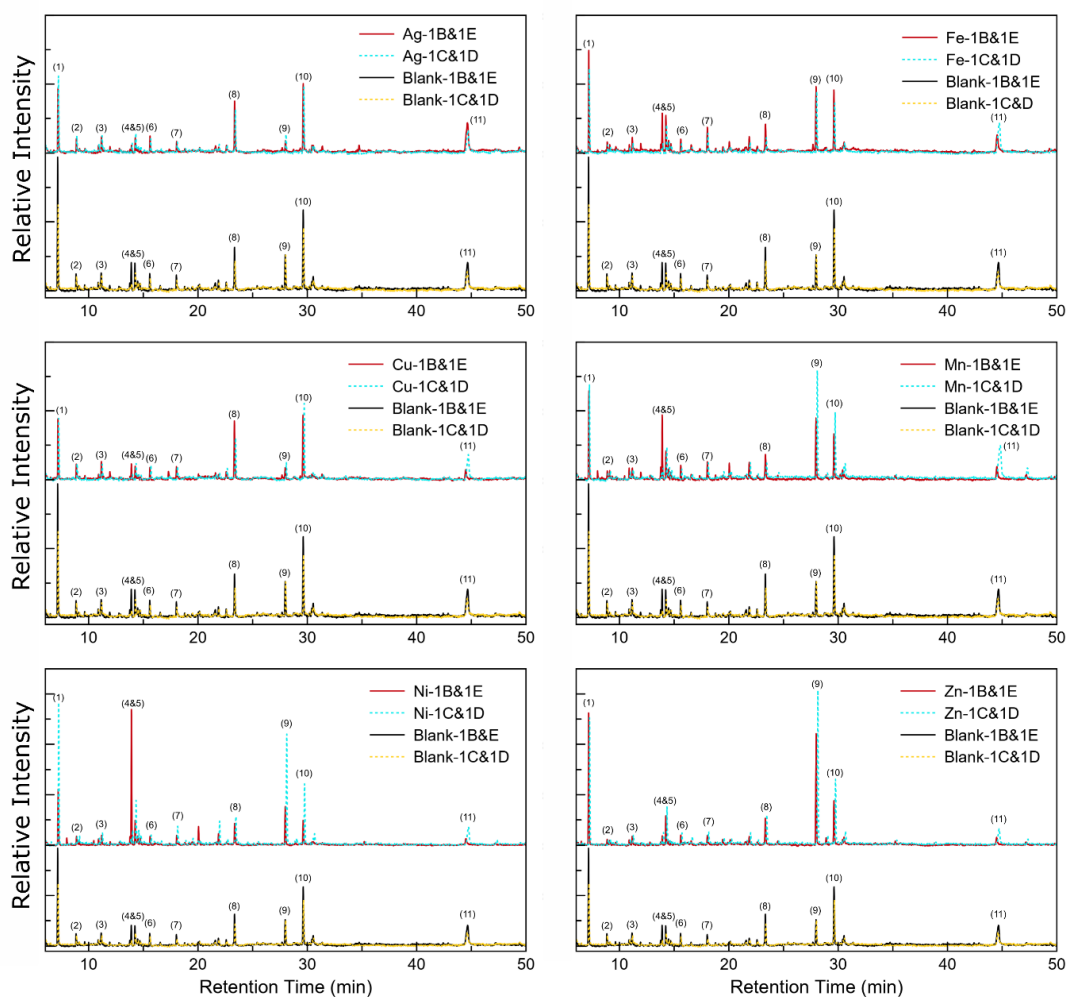


**Figure B3.** Bio-oil chromatograms for batches 2 and 3 – labeled with peaks of interest as detailed in Table B6

## Appendix C

### Supplemental Information for Chapter 6: Transition Metals as *in/ex situ* Catalysts for Cherry Pits

Table C1	Calibration compounds for gas chromatography mass spectroscopy	XVII
Figure C1	Pyrolysis gas formation (hydrogen, methane, ethane) for in situ and ex situ transition metals	XVIII

**Table C1.** Calibration compounds for gas chromatography mass spectroscopy

Trans-2-octene	5-Methyl-2-Furaldehyde	7-Tetradecene
Furfural	Mesitylene	Tetradecane
2,4-Dimethyl-3-Pentanol	Phenol	2,6-Dimethoxy-4-methylphenol
Furfuryl Alcohol (2-Furanmethanol)	3-Methyl-1,2-Cyclopentanedione	1-Chlorooctadecane
5-Hexen-1-ol	O-Cresol (Phenol, 2-methyl-)	Methyl linoleate
2-Methyl-2-Cyclopenten-1-one	Undecane	Heneicosane
Heptaldehyde (Heptanal)	Levoglucosenone	Methyl trans 9-octadecenoate
2-Acetylfuran (1-2-Furanyl-Ethanone)	Dodecane	N-Methyldodecanamide
2,5-Dimethylpyrrole	2-Propyl-1-Heptanol	

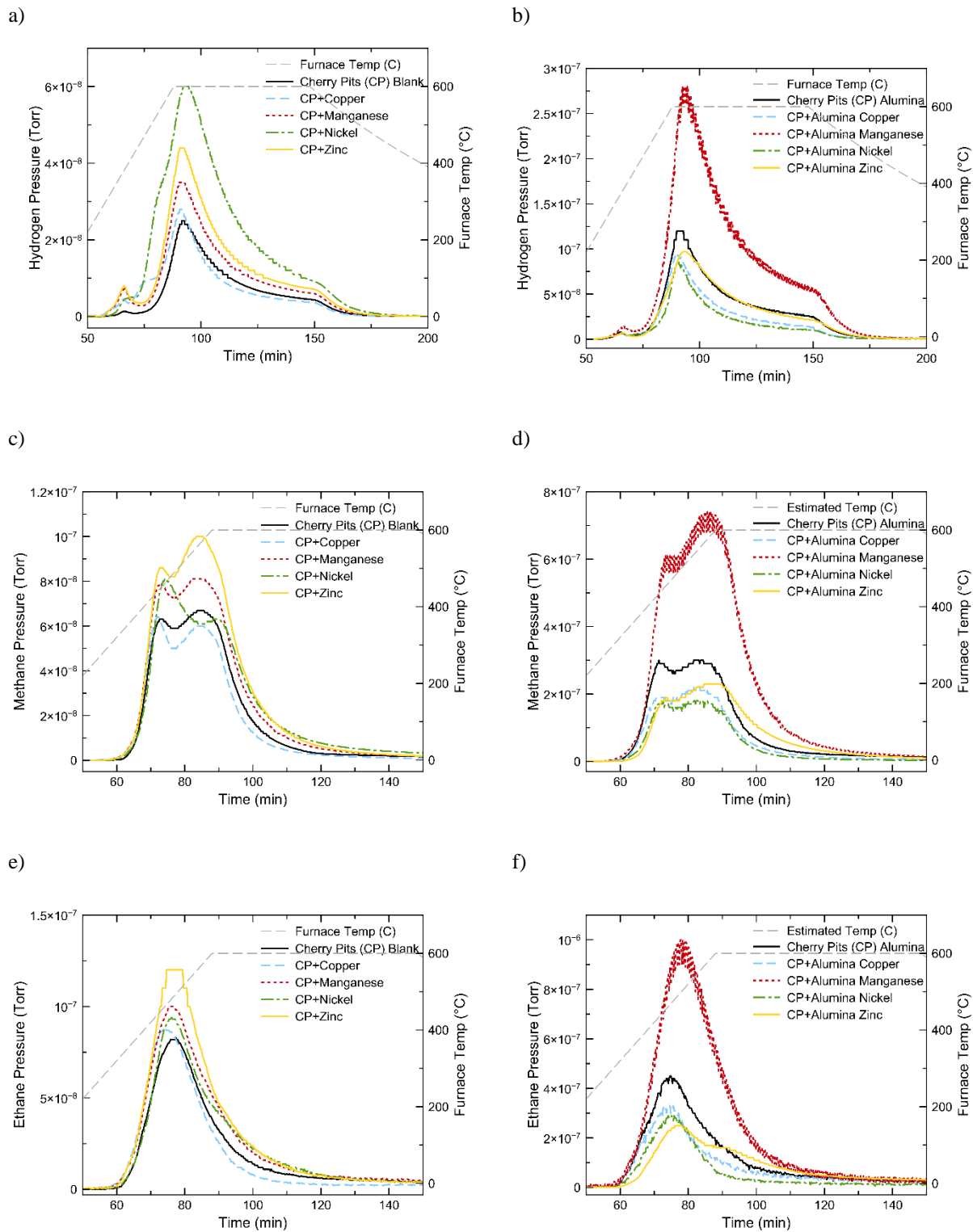


**Figure C1.** Pyrolysis gas formation (hydrogen, methane, ethane) for *in situ* and *ex situ* transition metals

## Appendix D

### Supplemental Information for Chapter 7: Clay Minerals as *in situ* Catalysts for Cherry Pits

Table D1	Bio-oil fatty acid concentration (Cherry Pits, Sand, Illite)	XX
Table D2	Bio-oil fatty acid concentration (Montmorillonite, Attapulgite)	XXI

**Table D1.** Bio-oil fatty acid concentration (Cherry Pits, Sand, Illite)

	Cherry Pits A (PPM)	Cherry Pits B (PPM)	CP + 10% Sand A (PPM)	CP + 10% Sand B (PPM)	CP + 10% Illite A (PPM)	CP + 10% Illite B (PPM)
9-Octadecenoic acid, (E)-	25,075	97,763	70,940	7,958	20,162	40,622
9-Octadecenoic acid, methyl ester, (E)-	15,889	62,844	47,410	24,673	19,213	39,001
Oleic Acid	16,820	0	0	26,844	0	0
9-Octadecenoic acid, 1,2,3-propanetriyl ester, (E,E,E)-	1,007	29,525	20,108	0	646	0
9,12-Octadecadienoic acid (Z,Z)-, methyl ester	9,849	14,703	11,544	8,678	15,387	13,908
n-Hexadecanoic acid	1,761	12,034	5,299	1,296	566	3,853
6-Octadecenoic acid, methyl ester, (Z)-	6,579	0	18,852	9,902	8,429	12,051
Hexadecanoic acid, methyl ester	1,873	10,558	8,030	4,127	2,483	6,520
Trifluoroacetic acid,n- tridecyl ester	6,197	0	0	0	0	0
Octadecanoic acid	0	3,304	0	0	0	0
Methyl stearate	1,733	4,577	3,398	1,428	2,336	2,287
1,2-Ethanediol, diacetate	0	1,733	1,729	0	321	0
10-Octadecenoic acid, methyl ester	1,334	0	0	0	0	0
Vinyl 10-undecenoate	561	0	0	0	0	0
Acetic acid, trifluoro-, undecyl ester	205	331	0	0	124	0
Decyl trifluoroacetate	201	0	0	0	0	0
Hexanoic acid, octadecyl ester	185	0	0	0	0	0
Isoamyl nitrite	0	0	0	0	47	0
trans, trans-Octa-2,4- dienyl acetate	0	0	0	0	0	0
Ethanol, 2-bromo-, acetate	0	0	0	0	0	0
6-Octadecenoic acid, (Z)-	0	0	0	0	0	0
9-Octadecenoic acid	0	0	0	0	10,747	0
<b>Average</b>	<b>163,320</b>		<b>136,108</b>		<b>99,352</b>	
<b>Standard Deviation</b>	<b>74,052</b>		<b>51,202</b>		<b>18,891</b>	

**Table D2.** Bio-oil fatty acid concentration (Montmorillonite, Attapulgite)

	<b>CP + 10% Montmorillonite A (PPM)</b>	<b>CP + 10% Montmorillonite B (PPM)</b>	<b>CP + 10% Attapulgite A (PPM)</b>	<b>CP + 10% Attapulgite B (PPM)</b>
9-Octadecenoic acid, (E)-	218,011	97,854	0	63,503
9-Octadecenoic acid, methyl ester, (E)-	103,546	47,280	19,200	39,448
Oleic Acid	0	0	19,273	0
9-Octadecenoic acid, 1,2,3-propanetriyl ester, (E,E,E)-	0	0	0	16,559
9,12-Octadecadienoic acid (Z,Z)-, methyl ester	21,806	10,592	8,845	10,609
n-Hexadecanoic acid	26,564	10,658	1,456	6,649
6-Octadecenoic acid, methyl ester, (Z)-	0	22,310	8,211	0
Hexadecanoic acid, methyl ester	17,241	8,429	3,167	7,226
Trifluoroacetic acid,n- tridecyl ester	0	0	0	0
Octadecanoic acid	7,656	9,721	0	0
Methyl stearate	10,058	4,578	1,873	3,344
1,2-Ethanediol, diacetate	4,189	0	0	0
10-Octadecenoic acid, methyl ester	0	0	0	0
Vinyl 10-undecenoate	0	0	0	0
Acetic acid, trifluoro-, undecyl ester	1,194	762	0	0
Decyl trifluoroacetate	0	0	185	0
Hexanoic acid, octadecyl ester	0	0	0	0
Isoamyl nitrite	0	0	0	0
trans, trans-Octa-2,4- dienyl acetate	221	0	0	0
Ethanol, 2-bromo-, acetate	0	0	341	0
6-Octadecenoic acid, (Z)-	0	48,333	0	0
9-Octadecenoic acid	0	0	0	0
<b>Average</b>	<b>335,502</b>		<b>104,945</b>	
<b>Standard Deviation</b>	<b>74,984</b>		<b>42,394</b>	

## References

1. Klass, D. L. *Biomass for Renewable Energy, Fuels, and Chemicals*. (Elsevier, 1998).
2. Jones, C. I. Was an Industrial Revolution Inevitable? Economic Growth Over the Very Long Run. *Advances in Macroeconomics* **1**, (2001).
3. Organization for Economic Cooperation and Development. *Renewables 2017: Analysis and Forecasts to 2022*. (2017).
4. L'vov, B. v. *Thermal Decomposition of Solids and Melts*. (Springer Netherlands, 2007).
5. Saha, B. C., Woodward, J. (Jonathan), American Chemical Society. Biotechnology Secretariat., American Chemical Society. Division of Biochemical Technology. & American Chemical Society. Meeting (211th : 1996 : New Orleans, La. ). Fuels and chemicals from biomass. 356 (1997).
6. Bridgwater, A. v. Review of fast pyrolysis of biomass and product upgrading. *Biomass and Bioenergy* **38**, 68–94 (2012).
7. Czernik, S. & Bridgwater, A. V. Overview of applications of biomass fast pyrolysis oil. *Energy and Fuels* **18**, 590–598 (2004).
8. Jahiril, M. *et al.* Biofuels Production through Biomass Pyrolysis —A Technological Review. *Energies* **5**, 4952–5001 (2012).
9. Andrigo, P., Bagatin, R. & Pagani, G. Fixed bed reactors. *Catalysis Today* **52**, 197–221 (1999).
10. Szufa, S. *et al.* Experimental Studies on Energy Crops Torrefaction Process Using Batch Reactor to Estimate Torrefaction Temperature and Residence Time. in *Renewable Energy Sources: Engineering, Technology, Innovation* (eds. Mudryk, K. & Werle, S.) 365–374 (Springer, 2017).

11. Knowlton, T. M. *Fluidized bed reactor design and scale-up. Fluidized Bed Technologies for Near-Zero Emission Combustion and Gasification* (Woodhead Publishing Limited, 2013). doi:10.1533/9780857098801.2.481.
12. Abdelgawad, B. Design of a gas-solid fluidized bed reactor at high temperature and high pressure. (Polytechnique Montréal, 2013).
13. Cheng, Y., Wang, Z., Gilbert, C. J., Fan, W. & Huber, G. W. Production of p-Xylene from Biomass by Catalytic Fast Pyrolysis Using ZSM-5 Catalysts with Reduced Pore Openings. *Angewandte Chemie* **124**, 11259–11262 (2012).
14. Cheng, Y., Jae, J., Shi, J., Fan, W. & Huber, G. W. Production of Renewable Aromatic Compounds by Catalytic Fast Pyrolysis of Lignocellulosic Biomass with Bifunctional Ga/ZSM-5 Catalysts. *Angewandte Chemie* **124**, 1416–1419 (2012).
15. Chang, S. *et al.* Effect of hydrothermal pretreatment on properties of bio-oil produced from fast pyrolysis of eucalyptus wood in a fluidized bed reactor. *Bioresource Technology* **138**, 321–328 (2013).
16. Wang, K., Brown, R. C., Homsy, S., Martinez, L. & Sidhu, S. S. Fast pyrolysis of microalgae remnants in a fluidized bed reactor for bio-oil and biochar production. *Bioresource Technology* **127**, 494–499 (2013).
17. Zhang, H. *et al.* Catalytic pyrolysis of black-liquor lignin by co-feeding with different plastics in a fluidized bed reactor. *Bioresource Technology* **192**, 68–74 (2015).
18. Christensen, E., Yanowitz, J., Ratcliff, M. & McCormick, R. L. Renewable Oxygenate Blending Effects on Gasoline Properties. *Energy and Fuels* **25**, 4723–4733 (2011).

19. McCormick, R. L. *et al.* Selection Criteria and Screening of Potential Biomass-Derived Streams as Fuel Blendstocks for Advanced Spark-Ignition Engines. *SAE International Journal of Fuels and Lubricants* **10**, 442–460 (2017).
20. Westmoreland, P. R. Pyrolysis kinetics for lignocellulosic biomass-to-oil from molecular modeling. *Current Opinion in Chemical Engineering* **23**, 123–129 (2019).
21. Mukarakate, C. *et al.* Influence of crystal allomorph and crystallinity on the products and behavior of cellulose during fast pyrolysis. *ACS Sustainable Chemistry and Engineering* **4**, 4662–4674 (2016).
22. Wu, Z. *et al.* Energy Recovery of Furnace Slag from Steel Industrial and Thermochemical Conversion of Lignocellulosic Biomass: Thermal Behavior and Kinetic Analysis on Cellulose under Fast Pyrolysis Conditions. *Energy & Fuels* **34**, 1111–1118 (2019).
23. Saha, B. C. Hemicellulose bioconversion. *Journal of Industrial Microbiology and Biotechnology* **30**, 279–291 (2003).
24. French, A. D. Idealized powder diffraction patterns for cellulose polymorphs. *Cellulose* **21**, 885–896 (2014).
25. O’Sullivan, A. Cellulose: The Structure Slowly Unravels. *Cellulose* **4**, 173–207 (1997).
26. Demirbaş, A. Mechanisms of liquefaction and pyrolysis reactions of biomass. *Energy Conversion and Management* **41**, 633–646 (2000).
27. Balat, M. Mechanisms of thermochemical biomass conversion processes. Part 1: Reactions of pyrolysis. *Energy Sources, Part A: Recovery, Utilization and Environmental Effects* **30**, 620–635 (2008).
28. Bennett, N. M., Helle, S. S. & Duff, S. J. B. Extraction and hydrolysis of levoglucosan from pyrolysis oil. *Bioresource Technology* **100**, 6059–6063 (2009).

29. Bai, X. & Brown, R. C. Modeling the physiochemistry of levoglucosan during cellulose pyrolysis. *Journal of Analytical and Applied Pyrolysis* **105**, 363–368 (2014).
30. Ashman, C. H., Gao, L. & Goldfarb, J. L. Silver nitrate in situ Upgrades Pyrolysis Biofuels from Brewer's Spent Grain via Biotemplating. *Journal of Analytical and Applied Pyrolysis* 104729 (2019) doi:10.1016/j.jaap.2019.104729.
31. Zhang, Q., Chang, J., Wang, T. & Xu, Y. Review of biomass pyrolysis oil properties and upgrading research. *Energy Conversion and Management* **48**, 87–92 (2007).
32. Zhuang, X. L., Zhang, H. X., Yang, J. Z. & Qi, H. Y. Preparation of levoglucosan by pyrolysis of cellulose and its citric acid fermentation. *Bioresource Technology* **79**, 63–66 (2001).
33. Wang, J., Wei, Q., Zheng, J. & Zhu, M. Effect of pyrolysis conditions on levoglucosan yield from cotton straw and optimization of levoglucosan extraction from bio-oil. *Journal of Analytical and Applied Pyrolysis* **122**, 294–303 (2016).
34. David, G. F., Justo, O. R., Perez, V. H. & Garcia-Perez, M. Thermochemical conversion of sugarcane bagasse by fast pyrolysis: High yield of levoglucosan production. *Journal of Analytical and Applied Pyrolysis* **133**, 246–253 (2018).
35. Holtzapple, M. T. Hemicelluloses. in *Encyclopedia of Food Sciences and Nutrition* 3060–3071 (Elsevier, 2003). doi:10.1016/B0-12-227055-X/00589-7.
36. Ren, J. L. & Sun, R. C. Hemicelluloses. *Cereal Straw as a Resource for Sustainable Biomaterials and Biofuels* 73–130 (2010) doi:10.1016/B978-0-444-53234-3.00004-3.
37. Schwarz, E. C. A. & Timell, T. E. Characterization of the Three Hemicelluloses from the wood of Amabilis Fir (*Abies Amabilis*). *Canadian Journal of Chemistry* **41**, 1381–1388 (2011).

38. Singh, S., Singh, G. & Arya, S. K. Mannans: An overview of properties and application in food products. *International Journal of Biological Macromolecules* **119**, 79–95 (2018).
39. Mussatto, S. I., Carneiro, L. M., Silva, J. P. A., Roberto, I. C. & Teixeira, J. A. A study on chemical constituents and sugars extraction from spent coffee grounds. *Carbohydrate Polymers* **83**, 368–374 (2011).
40. Usino, D. O., Supriyanto, Ylitervo, P., Pettersson, A. & Richards, T. Influence of temperature and time on initial pyrolysis of cellulose and xylan. *Journal of Analytical and Applied Pyrolysis* 104782 (2020) doi:10.1016/j.jaap.2020.104782.
41. Belmokaddem, F. Z., Pinel, C., Huber, P., Petit-Conil, M. & Da Silva Perez, D. Green synthesis of xylan hemicellulose esters. *Carbohydrate Research* **346**, 2896–2904 (2011).
42. Dutta, S. K. & Chakraborty, S. Kinetic analysis of two-phase enzymatic hydrolysis of hemicellulose of xylan type. *Bioresource Technology* **198**, 642–650 (2015).
43. Wang, W., Ren, J., Li, H., Deng, A. & Sun, R. Direct transformation of xylan-type hemicelluloses to furfural via SnCl<sub>4</sub> catalysts in aqueous and biphasic systems. *Bioresource Technology* **183**, 188–194 (2015).
44. Syaftika, N. & Matsumura, Y. Comparative study of hydrothermal pretreatment for rice straw and its corresponding mixture of cellulose, xylan, and lignin. *Bioresource Technology* **255**, 1–6 (2018).
45. Bozell, J. J. & Petersen, G. R. Technology development for the production of biobased products from biorefinery carbohydrates—the US Department of Energy’s “top 10” revisited. *Green Chemistry* **12**, 539–55 (2010).
46. Beaumont, O. Flash pyrolysis products from beech wood. *Wood and fiber science* **17**, 228–239 (1985).

47. Pérez, J., Muñoz-Dorado, J., De La Rubia, T. & Martínez, J. Biodegradation and biological treatments of cellulose, hemicellulose and lignin: An overview. *International Microbiology* **5**, 53–63 (2002).
48. Krulwich, R. The Fantastically Strange Origin of Most Coal on Earth. *National Geographic: Science and Innovation*  
<https://www.nationalgeographic.com/science/phenomena/2016/01/07/the-fantastically-strange-origin-of-most-coal-on-earth/> (2016).
49. Patil, N. D., Tanguy, N. R. & Yan, N. Lignin Interunit Linkages and Model Compounds. in *Lignin in Polymer Composites* 27–47 (Elsevier Inc., 2015). doi:10.1016/B978-0-323-35565-0.00003-5.
50. Zakzeski, J., Bruijninx, P. C. A., Jongerius, A. L. & Weckhuysen, B. M. The Catalytic Valorization of Lignin for the Production of Renewable Chemicals. *Chemical Reviews* **110**, 3552–3599 (2010).
51. Binder, J. B., Gray, M. J., White, J. F., Zhang, Z. C. & Holladay, J. E. Reactions of lignin model compounds in ionic liquids. *Biomass and Bioenergy* **33**, 1122–1130 (2009).
52. Jarvis, M. W. *et al.* Direct detection of products from the pyrolysis of 2-phenethyl phenyl ether. *Journal of Physical Chemistry A* **115**, 428–438 (2011).
53. Ormond, T. K. *et al.* Thermal Decompositions of the Lignin Model Compounds: Salicylaldehyde and Catechol. *Journal of Physical Chemistry A* **122**, 5911–5924 (2018).
54. Chang, Y. C., Choi, D. B., Takamizawa, K. & Kikuchi, S. Isolation of *Bacillus* sp. strains capable of decomposing alkali lignin and their application in combination with lactic acid bacteria for enhancing cellulase performance. *Bioresource Technology* **152**, 429–436 (2014).

55. Asmadi, M., Kawamoto, H. & Saka, S. Thermal reactivities of catechols/pyrogallols and cresols/xilenols as lignin pyrolysis intermediates. *Journal of Analytical and Applied Pyrolysis* **92**, 76–87 (2011).
56. Kawamoto, H. Lignin pyrolysis reactions. *Journal of Wood Science* vol. 63 117–132 (2017).
57. Shahbaz, M. *et al.* Investigation of biomass components on the slow pyrolysis products yield using Aspen Plus for techno-economic analysis. *Biomass Conversion and Biorefinery* 1–13 (2020) doi:10.1007/s13399-020-01040-1.
58. Bridgwater, A. V., Meier, D. & Radlein, D. An overview of fast pyrolysis of biomass. *Organic Geochemistry* **30**, 1479–1493 (1999).
59. Lei, L., Wang, Y., Zhang, Z., An, J. & Wang, F. Transformations of Biomass, Its Derivatives, and Downstream Chemicals over Ceria Catalysts. *ACS Catalysis* **10**, 8788–8814 (2020).
60. Ruivo, L. C. M. *et al.* Iron-based catalyst (Fe<sub>2-x</sub>Ni<sub>x</sub>TiO<sub>5</sub>) for tar decomposition in biomass gasification. *Fuel* **300**, 120859 (2021).
61. Asgari, M., Vitale, G. & Sundararaj, U. Synthesis and characterization of a novel nickel pillared–clay catalyst: In-situ carbon nanotube–clay hybrid nanofiller from Ni-PILC. *Applied Clay Science* **205**, 106064 (2021).
62. Yang, X.-F. *et al.* High-Performance Bifunctional Ni–Fe–S Catalyst in situ Synthesized within Graphite Intergranular Nanopores for Overall Water Splitting. *ChemSusChem* **14**, 3131–3138 (2021).

63. Caine, M. *et al.* The Use of Clays as Sorbents and Catalysts. in *Natural Microporous Materials in Environmental Technology* 49–69 (Springer Netherlands, 1999).  
doi:10.1007/978-94-011-4499-5\_4.
64. Carpenter, D., Westover, T. L., Czernik, S. & Jablonski, W. Biomass feedstocks for renewable fuel production: A review of the impacts of feedstock and pretreatment on the yield and product distribution of fast pyrolysis bio-oils and vapors. *Green Chemistry* vol. 16 384–406 (2014).
65. Balat, M. Mechanisms of thermochemical biomass conversion processes. Part 2: Reactions of gasification. *Energy Sources, Part A: Recovery, Utilization and Environmental Effects* **30**, 636–648 (2008).
66. Wan, S. & Wang, Y. A review on ex situ catalytic fast pyrolysis of biomass. *Frontiers of Chemical Science and Engineering* **8**, 280–294 (2014).
67. Nguyen, L. T. Tr. *et al.* A LaFeO<sub>3</sub> supported natural-clay-mineral catalyst for efficient pyrolysis of polypropylene plastic material. *Asia-Pacific Journal of Chemical Engineering* e2695 (2021) doi:10.1002/APJ.2695.
68. Dong, Y. *et al.* Enhanced Hydrolysis of Cellulose to Reducing Sugars on Kaolinite Clay Activated by Mineral Acid. *Catalysis Letters* 2021 151:10 **151**, 2797–2806 (2021).
69. Boudissa, F. *et al.* Acid-treated clay catalysts for organic dye ozonation – Thorough mineralization through optimum catalyst basicity and hydrophilic character. *Journal of Hazardous Materials* **364**, 356–366 (2019).
70. Dai, H. *et al.* Ni-Based catalysts supported on natural clay of attapulgite applied in the dry reforming of methane reaction. *New Journal of Chemistry* **44**, 16101–16109 (2020).

71. Annett Steudel. *Selection strategy and modification of layer silicates for technical applications. Karlsruher Mineralogische und Geochemische Hefte* vol. 36 (2009).
72. Wolf, E. E. & Alfani, F. Catalysts Deactivation by Coking. <https://doi.org/10.1080/03602458208079657> **24**, 329–371 (2007).
73. Dohrmann, R. Cation exchange capacity methodology I: An efficient model for the detection of incorrect cation exchange capacity and exchangeable cation results. *Applied Clay Science* **34**, 31–37 (2006).
74. Layng, T. E. & Soukup, R. Partial oxidation of methane and ethane in the presence of catalysts. *Proceedings of the Symposium on Combustion* **1–2**, 95–100 (1948).
75. Tyutyunnikov, B. N., Slinkin, A. A., Paper, T. S. F. & Arkhipov, P. P. Structure, physical properties, and catalytic activity of coppernickel catalysts of the hydrogenation of fats- 3. *Kinetics and Catalysis* **v 12, 1 pt 2 Jan**, p 169-173 (1971).
76. Awad, A. A. A., Moustafa Ali, O. A. & Fattah Nassar, D. A. Degradation of dye wastewater by using cobalt, copper and nickel Schiff base complexes as catalysts: spectral, molecular modelling, catalytic activity and metal removal from aqueous solution. <https://doi.org/10.1080/03067319.2021.2014466> (2022)  
doi:10.1080/03067319.2021.2014466.
77. Kumar, A., Mohammed, A. A. A., Saad, M. A. H. S. & Al-Marri, M. J. Effect of nickel on combustion synthesized copper/fumed-SiO<sub>2</sub> catalyst for selective reduction of CO<sub>2</sub> to CO. *International Journal of Energy Research* **46**, 441–451 (2022).
78. Fukuoka, S. Transition Metal Catalyst-Free and Radical Initiator-Free Carbonylation of Aryl Iodides. *Industrial and Engineering Chemistry Research* **55**, 4830–4835 (2016).

79. Liu, Z. *et al.* Transition Metal Catalyst-Free, Base-Promoted 1,2-Additions of Polyfluorophenylboronates to Aldehydes and Ketones. *Angewandte Chemie International Edition* **60**, 16529–16538 (2021).
80. Huh, D. N., Cheng, Y., Frye, C. W., Egger, D. T. & Tonks, I. A. Multicomponent syntheses of 5- and 6-membered aromatic heterocycles using group 4–8 transition metal catalysts. *Chemical Science* **12**, 9574–9590 (2021).
81. Mamun, O., Winther, K. T., Boes, J. R. & Bligaard, T. High-throughput calculations of catalytic properties of bimetallic alloy surfaces. *Scientific Data 2019 6:1* **6**, 1–9 (2019).
82. Wang, F. *et al.* Promoting hydrocarbon production from fatty acid pyrolysis using transition metal or phosphorus modified Al-MCM-41 catalyst. *Journal of Analytical and Applied Pyrolysis* **156**, 105146 (2021).
83. Jedvert, K. & Heinze, T. Cellulose modification and shaping - A review. *Journal of Polymer Engineering* **37**, 845–860 (2017).
84. Zhou, X., Li, W., Mabon, R. & Broadbelt, L. J. A critical review on hemicellulose pyrolysis. *Energy Technology* vol. 5 52–79 (2017).
85. Yang, L., Seshan, K. & Li, Y. A review on thermal chemical reactions of lignin model compounds. *Catalysis Today* **298**, 276–297 (2017).
86. Pasangulapati, V. *et al.* Effects of cellulose, hemicellulose and lignin on thermochemical conversion characteristics of the selected biomass. *Bioresource Technology* **114**, 663–669 (2012).
87. Jaffar, M. M., Nahil, M. A. & Williams, P. T. Pyrolysis-catalytic hydrogenation of cellulose-hemicellulose-lignin and biomass agricultural wastes for synthetic natural gas production. *Journal of Analytical and Applied Pyrolysis* **145**, 104753 (2020).

88. Yang, H. *et al.* Vapor–solid interaction among cellulose, hemicellulose and lignin. *Fuel* **263**, 116681 (2020).
89. Xue, J., Ceylan, S. & Goldfarb, J. L. Synergism among biomass building blocks? Evolved gas and kinetics analysis of starch and cellulose co-pyrolysis. *Thermochimica Acta* **618**, 36–47 (2015).
90. Liu, Q., Zhong, Z., Wang, S. & Luo, Z. Interactions of biomass components during pyrolysis: A TG-FTIR study. *Journal of Analytical and Applied Pyrolysis* **90**, 213–218 (2011).
91. Chen, W. H. & Kuo, P. C. Torrefaction and co-torrefaction characterization of hemicellulose, cellulose and lignin as well as torrefaction of some basic constituents in biomass. *Energy* **36**, 803–811 (2011).
92. Vyazovkin, S. *et al.* ICTAC Kinetics Committee recommendations for analysis of multi-step kinetics. *Thermochimica Acta* vol. 689 178597 (2020).
93. Bhoi, P. R., Ouedraogo, A. S., Soloiu, V. & Quirino, R. Recent advances on catalysts for improving hydrocarbon compounds in bio-oil of biomass catalytic pyrolysis. *Renewable and Sustainable Energy Reviews* **121**, 109676 (2020).
94. Sun, L. *et al.* Improving the monocyclic aromatic hydrocarbons production from fast pyrolysis of biomass over Fe-modified ZSM-5 catalysts. *International Journal of Energy Research* **45**, 6032–6040 (2021).
95. Raymundo, L. M., Mullen, C. A., Strahan, G. D., Boateng, A. A. & Trierweiler, J. O. Deoxygenation of Biomass Pyrolysis Vapors via in Situ and ex Situ Thermal and Biochar Promoted Upgrading. *Energy and Fuels* **33**, 2197–2207 (2019).

96. Wang, M., Li, Z., Huang, W., Yang, J. & Xue, H. Coal pyrolysis characteristics by TG-MS and its late gas generation potential. *Fuel* **156**, 243–253 (2015).
97. Shafizadeh, F. & Bradbury, A. G. W. Thermal degradation of cellulose in air and nitrogen at low temperatures. *Journal of Applied Polymer Science* **23**, 1431–1442 (1979).
98. Lewin, M. & Basch, A. Structure, Pyrolysis, and Flammability of Cellulose. in *Flame - Retardant Polymeric Materials* (Springer, 1978). doi:[https://doi.org/10.1007/978-1-4684-6973-8\\_1](https://doi.org/10.1007/978-1-4684-6973-8_1).
99. Volpe, R., Zabaniotou, A. A. & Skoulou, V. Synergistic Effects between Lignin and Cellulose during Pyrolysis of Agricultural Waste. *Energy and Fuels* **32**, 8420–8430 (2018).
100. Zhang, J. *et al.* Cellulose-hemicellulose and cellulose-lignin interactions during fast pyrolysis. *ACS Sustainable Chemistry and Engineering* **3**, 293–301 (2015).
101. Huang, J., He, C., Wu, L. & Tong, H. Thermal degradation reaction mechanism of xylose: A DFT study. *Chemical Physics Letters* **658**, 114–124 (2016).
102. Jablonsky, M., Botkova, M. & Adamovska, J. Prediction of methoxyl groups content in lignin based on ultimate analysis. *Cellulose Chemistry and Technology Cellulose Chem. Technol* vol. 49 (2015).
103. Faix, O., Jakab, E., Till, F. & Székely, T. Study on low mass thermal degradation products of milled wood lignins by thermogravimetry-mass-spectrometry. *Wood Science and Technology* **22**, 323–334 (1988).
104. Lu, Q. *et al.* A novel interaction mechanism in lignin pyrolysis: Phenolics-assisted hydrogen transfer for the decomposition of the  $\beta$ -O-4 linkage. *Combustion and Flame* **225**, 395–405 (2021).

105. Lehmann, J. & Joseph, S. *Biochar for environmental management: Science and technology. Biochar for Environmental Management: Science and Technology* (Earthscan, 2009).
106. Geoffrey Skinner, P. F. & Kowal, W. M. *United States Patent (19) Skinner et al. 54 Synthesis gas for ammonia.* (1981).
107. Zong, P. *et al.* Pyrolysis behavior and product distributions of biomass six group components: Starch, cellulose, hemicellulose, lignin, protein and oil. *Energy Conversion and Management* **216**, 112777 (2020).
108. Gao, Z., Li, N., Wang, Y., Niu, W. & Yi, W. Pyrolysis behavior of xylan-based hemicellulose in a fixed bed reactor. *Journal of Analytical and Applied Pyrolysis* **146**, 104772 (2020).
109. Agarwal, A., Park, S. J. & Park, J. H. Catalytic upgrading of Kraft lignin derived bio-oil in supercritical ethanol over different crystal size hierarchical nano-HZSM5. *Fuel* **271**, 117630 (2020).
110. Adjaye, J. D. & Bakhshi, N. N. Production of hydrocarbons by catalytic upgrading of a fast Part II : Comparative catalyst performance and reaction pathways. *Fuel Processing Technology* **45**, 185–202 (1995).
111. Wang, L. & Xiao, F. Nanoporous catalysts for biomass conversion. *Green Chemistry* **17**, 24–39 (2015).
112. Geboers, J., Vyver, S. Van de & Carpentier, K. Efficient catalytic conversion of concentrated cellulose feeds to hexitols with heteropoly acids and Ru on carbon. *Chemical communications* **46**, 3577–3579 (2010).

113. Deng, W., Tan, X., Fang, W., Zhang, Q. & Wang, Y. Conversion of cellulose into sorbitol over carbon nanotube-supported ruthenium catalyst. *Catalysis Letters* **133**, 167–174 (2009).
114. Wang, A. & Zhang, T. One-pot conversion of cellulose to ethylene glycol with multifunctional tungsten-based catalysts. *Accounts of chemical research* **46**, 1377–1386 (2013).
115. Hashmi, S. F. *et al.* Effect of metal formates on hydrothermolysis of organosolv lignin for the production of bio-oil. *Fuel* **271**, 117573 (2020).
116. Huo, E. *et al.* Phenols production from Douglas fir catalytic pyrolysis with MgO and biomass-derived activated carbon catalysts. *Energy* **199**, 117459 (2020).
117. Ferreira, A. F. & Soares Dias, A. P. Pyrolysis of microalgae biomass over carbonate catalysts. *Journal of Chemical Technology & Biotechnology* **95**, 3270–3279 (2020).
118. Ghorbannezhad, P., Park, S. & Onwudili, J. A. Co-pyrolysis of biomass and plastic waste over zeolite- and sodium-based catalysts for enhanced yields of hydrocarbon products. *Waste Management* **102**, 909–918 (2020).
119. Iisa, K., French, R. J., Orton, K. A., Dutta, A. & Schaidle, J. A. Production of low-oxygen bio-oil via ex situ catalytic fast pyrolysis and hydrotreating. *Fuel* **207**, 413–422 (2017).
120. Huber, G. W., Iborra, S. & Corma, A. Synthesis of transportation fuels from biomass: Chemistry, catalysts, and engineering. *Chemical Reviews* vol. 106 4044–4098 (2006).
121. Kantarelis, E., Yang, W. & Blasiak, W. Effect of zeolite to binder ratio on product yields and composition during catalytic steam pyrolysis of biomass over transition metal modified HZSM5. *Fuel* **122**, 119–125 (2014).

122. Oyer, M. M., Karakaya, C., Kee, R. J. & Rewyn, B. T. In Situ Formation of Metal Carbide Catalysts. *ChemCatChem* **9**, 3090–3101 (2017).
123. Bali, S., Tofanelli, M. A., Ernst, R. D. & Eyring, E. M. Chromium(III) catalysts in ionic liquids for the conversion of glucose to 5-(hydroxymethyl)furfural (HMF): Insight into metal catalyst:ionic liquid mediated conversion of cellulosic biomass to biofuels and chemicals. *Biomass and Bioenergy* **42**, 224–227 (2012).
124. Sykes, A. G. *Kinetics of Inorganic Reactions*. (Pergamon Press, 1970).
125. Tang, X., Ding, W. & Li, H. Improved hydrodeoxygenation of bio-oil model compounds with polymethylhydrosiloxane by Brønsted acidic zeolites. *Fuel* **290**, 119883 (2021).
126. Kazansky, V. B., Frash, M. V. & Van Santen, R. A. Quantumchemical study of the isobutane cracking on zeolites. *Applied Catalysis A: General* **146**, 225–247 (1996).
127. Corma, A. & Orchillés, A. V. Current views on the mechanism of catalytic cracking. *Microporous and Mesoporous Materials* **35–36**, 21–30 (2000).
128. Shao, Y. *et al.* Sulfated TiO<sub>2</sub> nanosheets catalyzing conversion of biomass derivatives: influences of the sulfation on distribution of Brønsted and Lewis acidic sites. *Journal of Chemical Technology & Biotechnology* **95**, 1337–1347 (2020).
129. Lu, Q., Xiong, W., Li, W., Guo, Q. & Zhu, X. Catalytic pyrolysis of cellulose with sulfated metal oxides: A promising method for obtaining high yield of light furan compounds. *Bioresource technology* **100**, 4871–4876 (2009).
130. Yu, I. K. *et al.* Aluminium-Biochar Composites as Sustainable Heterogeneous Catalysts for Glucose Isomerisation in a Biorefinery. *Green Chemistry* (2018)  
doi:10.1039/C8GC02466A.

131. Liu, W. J., Jiang, H. & Yu, H. Q. Development of Biochar-Based Functional Materials: Toward a Sustainable Platform Carbon Material. *Chemical Reviews* vol. 115 12251–12285 (2015).
132. Mullen, C. A. *et al.* Bio-oil and bio-char production from corn cobs and stover by fast pyrolysis. *Biomass and Bioenergy* **34**, 67–74 (2010).
133. Pokorna, E. *et al.* Study of bio-oils and solids from flash pyrolysis of sewage sludges. *Fuel* **88**, 1344–1350 (2009).
134. Zhou, Y., Gao, B., Zimmerman, A. R. & Cao, X. Biochar-supported zerovalent iron reclaims silver from aqueous solution to form antimicrobial nanocomposite. *Chemosphere* **117**, 801–805 (2014).
135. Smyth, M., García, A., Rader, C., Foster, E. J. & Bras, J. Extraction and process analysis of high aspect ratio cellulose nanocrystals from corn (*Zea mays*) agricultural residue. *Industrial Crops and Products* **108**, 257–266 (2017).
136. Lazdovica, K. & Kampars, V. Catalytic intermediate pyrolysis of cellulose for hydrocarbon production in the presence of zeolites by using tga-ftir method. in *Key Engineering Materials* vol. 850 KEM 127–132 (Trans Tech Publications Ltd, 2020).
137. Banyasz, J. L., Li, S., Lyons-Hart, J. & Shafer, K. H. Gas evolution and the mechanism of cellulose pyrolysis. *Fuel* **80**, 1757–1763 (2001).
138. Lu, Q. *et al.* A novel interaction mechanism in lignin pyrolysis: Phenolics-assisted hydrogen transfer for the decomposition of the  $\beta$ -O-4 linkage. *Combustion and Flame* **225**, 395–405 (2021).

139. LeBlanc, J., Quanci, J. & Castaldi, M. J. Experimental Investigation of Reaction Confinement Effects on Coke Yield in Coal Pyrolysis. *Energy and Fuels* **30**, 6249–6256 (2016).
140. Luik, H., Johannes, I., Palu, V., Luik, L. & Kruusement, K. Transformations of biomass internal oxygen at varied pyrolysis conditions. *Journal of Analytical and Applied Pyrolysis* **79**, 121–127 (2007).
141. Shengyu, L. The Fate of Organic Oxygen During Coal Pyrolysis. *Energy Sources* **25**, 479–488 (2003).
142. Li, J. *et al.* Examination of CO, CO<sub>2</sub> and active sites formation during isothermal pyrolysis of coal at low temperatures. *Energy* **185**, 28–38 (2019).
143. Hoydonckx, H. E., Van Rhijn, W. M., Van Rhijn, W., De Vos, D. E. & Jacobs, P. A. Furfural and Derivatives. in *Ullmann's Encyclopedia of Industrial Chemistry* (Wiley-VCH Verlag GmbH & Co. KGaA, 2007). doi:10.1002/14356007.a12\_119.pub2.
144. Blythe, D. A. & Schroeder, L. R. Degradation of a nonreducing cellulose model, 1,5-anhydro-4-0-β-D-glucopyranosyl-D-glucitol, under kraft pulping conditions. *Journal of Wood Chemistry and Technology* **5**, 313–334 (1985).
145. Arteaga-Pérez, L. E. *et al.* Catalytic upgrading of biomass-derived vapors on carbon aerogel-supported Ni: Effect of temperature, metal cluster size and catalyst-to-biomass ratio. *Fuel Processing Technology* **178**, 251–261 (2018).
146. Ogoshi, S. *Nickel Catalysis in Organic Synthesis*. (Wiley-VCH, 2020).
147. Freel, J. & Galwey, A. K. Hydrocarbon cracking reactions on nickel. *Journal of Catalysis* **10**, 277–289 (1968).

148. Oyer, M. M., Karakaya, C., Kee, R. J. & Rewyn, B. T. In Situ Formation of Metal Carbide Catalysts. *ChemCatChem* **9**, 3090–3101 (2017).
149. Shafizadeh, F. Introduction to pyrolysis of biomass. *Journal of Analytical and Applied Pyrolysis* vol. 3 283–305 (1982).
150. Ogoshi, S. *Nickel Catalysis in Organic Synthesis*. (Wiley-VCH, 2020).
151. Chemler, S. R. Copper catalysis in organic synthesis. *Beilstein Journal of Organic Chemistry* vol. 11 2252–2253 (2015).
152. Sahebdelfar, S., Bijani, P. M. & Yaripour, F. Deactivation kinetics of  $\gamma$ -Al<sub>2</sub>O<sub>3</sub> catalyst in methanol dehydration to dimethyl ether. *Fuel* **310**, 122443 (2022).
153. Kalogiannis, K. G., Stefanidis, S. D. & Lappas, A. A. Catalyst deactivation, ash accumulation and bio-oil deoxygenation during ex situ catalytic fast pyrolysis of biomass in a cascade thermal-catalytic reactor system. *Fuel Processing Technology* **186**, 99–109 (2019).
154. Hammes, G. G. & Amdur, I. (Isadore). *Principles of chemical kinetics*. (Academic Press, 1978).
155. Tang, Z. *et al.* Preparation of low-nitrogen and high-quality bio-oil from microalgae catalytic pyrolysis with zeolites and activated carbon. *Journal of Analytical and Applied Pyrolysis* **159**, 105182 (2021).
156. David, E. Evaluation of Na-13X zeolites activity in the catalytic pyrolysis of rapeseed oil cake to produce bio-oil. *Applied Catalysis A: General* **617**, 118126 (2021).
157. Rahman, M. M., Liu, R. & Cai, J. Catalytic fast pyrolysis of biomass over zeolites for high quality bio-oil – A review. *Fuel Processing Technology* **180**, 32–46 (2018).

158. Limarta, S. O., Kim, H., Ha, J. M., Park, Y. K. & Jae, J. High-quality and phenolic monomer-rich bio-oil production from lignin in supercritical ethanol over synergistic Ru and Mg-Zr-oxide catalysts. *Chemical Engineering Journal* **396**, 125175 (2020).
159. Li, Z., Jiang, E., Xu, X., Sun, Y. & Tu, R. Hydrodeoxygenation of phenols, acids, and ketones as model bio-oil for hydrocarbon fuel over Ni-based catalysts modified by Al, La and Ga. *Renewable Energy* **146**, 1991–2007 (2020).
160. Resasco, J. *et al.* Relationship between Atomic Scale Structure and Reactivity of Pt Catalysts: Hydrodeoxygenation of m-Cresol over Isolated Pt Cations and Clusters. *ACS Catalysis* **10**, 595–603 (2020).
161. Bodachivskiy, I., Kuzhiumparambil, U. & Williams, D. B. G. Metal triflates are tunable acidic catalysts for high yielding conversion of cellulosic biomass into ethyl levulinate. *Fuel Processing Technology* **195**, 106159 (2019).
162. Xiong, Z. *et al.* Effects of vapor-/solid-phase interactions among cellulose, hemicellulose and lignin on the formation of heavy components in bio-oil during pyrolysis. *Fuel Processing Technology* **225**, 107042 (2022).
163. Frišták, V. *et al.* Physicochemical Characterization of Cherry Pits-Derived Biochar. *Materials 2022, Vol. 15, Page 408* **15**, 408 (2022).
164. Yangali, P., Celaya, A. M. & Goldfarb, J. L. Co-pyrolysis reaction rates and activation energies of West Virginia coal and cherry pit blends. *Journal of Analytical and Applied Pyrolysis* **108**, 203–211 (2014).
165. Pollard, Z. A. & Goldfarb, J. L. Valorization of cherry pits: Great Lakes agro-industrial waste to mediate Great Lakes water quality. *Environmental Pollution* **270**, 116073 (2021).

166. Foreign Agricultural Service, G. M. A. *Fresh Peaches and Cherries: World Markets and Trade*. <https://public.govdelivery.com/accounts/USDAFAS/subscriber/new> (2021).
167. United States Department of Agriculture: National Statistics for Cherries. National Agricultural Statistics Service.  
[https://www.nass.usda.gov/Statistics\\_by\\_Subject/result.php?4DA594EC-B4CC-333F-9B93-929A52E35D50&sector=CROPS&group=FRUIT %26 TREE NUTS&comm=CHERRIES](https://www.nass.usda.gov/Statistics_by_Subject/result.php?4DA594EC-B4CC-333F-9B93-929A52E35D50&sector=CROPS&group=FRUIT%26TREE%26NUTS&comm=CHERRIES) (2020).
168. Zhang, S. *et al.* Upgrading of bio-oil from catalytic pyrolysis of pretreated rice husk over Fe-modified ZSM-5 zeolite catalyst. *Fuel Processing Technology* **175**, 17–25 (2018).
169. Li, Y. *et al.* Unraveling the role of reaction environment and catalysts for pyrolysis of technical lignin into different functional bio-oil yield. *Journal of the Energy Institute* **100**, 47–54 (2022).
170. Feroso, J. *et al.* Bio-oil production by lignocellulose fast-pyrolysis: Isolating and comparing the effects of indigenous versus external catalysts. *Fuel Processing Technology* **167**, 563–574 (2017).
171. Han, Y. *et al.* Hydrotreatment of pyrolysis bio-oil: A review. *Fuel Processing Technology* **195**, 106140 (2019).
172. de Luna, M. D. G., Cruz, L. A. D., Chen, W. H., Lin, B. J. & Hsieh, T. H. Improving the stability of diesel emulsions with high pyrolysis bio-oil content by alcohol co-surfactants and high shear mixing strategies. *Energy* **141**, 1416–1428 (2017).
173. Kwak, J. H., Hu, J. Z., Kim, D. H., Szanyi, J. & Peden, C. H. F. Penta-coordinated Al<sup>3+</sup> ions as preferential nucleation sites for BaO on  $\gamma$ -Al<sub>2</sub>O<sub>3</sub>: An ultra-high-magnetic field <sup>27</sup>Al MAS NMR study. *Journal of Catalysis* **251**, 189–194 (2007).

174. Feng, K. *et al.* Late-stage oxidative C(sp<sup>3</sup>)-H methylation. *Nature* 2020 580:7805 **580**, 621–627 (2020).
175. Dey, S. & Praveen Kumar, V. v. The performance of highly active manganese oxide catalysts for ambient conditions carbon monoxide oxidation. *Current Research in Green and Sustainable Chemistry* **3**, 100012 (2020).
176. Xia, Y., Xiong, Y., Lim, B. & Skrabalak, S. E. Shape-Controlled Synthesis of Metal Nanocrystals: Simple Chemistry Meets Complex Physics? *Angewandte Chemie International Edition* **48**, 60–103 (2009).
177. Dey, S., Dhal, G. C., Mohan, D. & Prasad, R. The choice of precursors in the synthesizing of CuMnOx catalysts for maximizing CO oxidation. *International Journal of Industrial Chemistry* **9**, 199–214 (2018).
178. Mei, Y. *et al.* Impact of cellulose deoxidization temperature on the composition of liquid products obtained by subsequent pyrolysis. *Fuel Processing Technology* **184**, 73–79 (2019).
179. Lang, C., Sécordel, X., Kiennemann, A. & Courson, C. Water gas shift catalysts for hydrogen production from biomass steam gasification. *Fuel Processing Technology* **156**, 246–252 (2017).
180. Rossetti, I. & Tripodi, · Antonio. Catalytic Production of Renewable Hydrogen for Use in Fuel Cells: A Review Study. *Topics in Catalysis* 2022 **1**, 1–20 (2022).
181. Mortensen, P. M., Grunwaldt, J. D., Jensen, P. A., Knudsen, K. G. & Jensen, A. D. A review of catalytic upgrading of bio-oil to engine fuels. *Applied Catalysis A: General* **407**, 1–19 (2011).

182. Schutyser, W. *et al.* Chemicals from lignin: an interplay of lignocellulose fractionation, depolymerisation, and upgrading. *Chem. Soc. Rev* **47**, 852 (2018).
183. Kristianto, I. *et al.* Effective depolymerization of concentrated acid hydrolysis lignin using a carbon-supported ruthenium catalyst in ethanol/formic acid media. *Bioresource Technology* **234**, 424–431 (2017).
184. Bhorodwaj, S. K. & Dutta, D. K. Heteropoly acid supported modified Montmorillonite clay: An effective catalyst for the esterification of acetic acid with sec-butanol. *Applied Catalysis A: General* **378**, 221–226 (2010).
185. Baloyi, J., Ntho, T. & Moma, J. Synthesis of highly active and stable Al/Zr pillared clay as catalyst for catalytic wet oxidation of phenol. *Journal of Porous Materials* **26**, 583–597 (2019).
186. Baloyi, J., Ntho, T. & Moma, J. A Novel Synthesis Method of Al/Cr Pillared Clay and its Application in the Catalytic Wet Air Oxidation of Phenol. *Catalysis Letters* **148**, 3655–3668 (2018).
187. Carroll, D. ION EXCHANGE IN CLAYS AND OTHER MINERALS. **70**, 749–780 (1959).
188. Vifttaria, M., Nurhayati & Anita, S. Surface Acidity of Sulfuric Acid Activated Maredan Clay Catalysts with Boehm Titration Method and Pyridine Adsorption-FTIR. *Journal of Physics: Conference Series* **1351**, 012040 (2019).
189. Ayodele, O. B. & Abdullah, A. Z. Exploring kaolinite as dry methane reforming catalyst support: Influences of chemical activation, organic ligand functionalization and calcination temperature. *Applied Catalysis A: General* **576**, 20–31 (2019).

190. Fahn, R. & Fenderl, K. Reaction products of organic dye molecules with acid-treated montmorillonite. *Clay Minerals* **18**, 447–458 (1983).
191. Delavernhe, L., Pilavtepe, M. & Emmerich, K. Cation exchange capacity of natural and synthetic hectorite. *Applied Clay Science* **151**, 175–180 (2018).
192. Kircher, C. C. Separation and characterizations of fractions from Mayan, Heavy Arabian, and Hondo crude oils. *American Chemical Society, Division of Petroleum Chemistry, Preprints* v **34**, n **2**, p 416-420 (1989).
193. Jeffrey, A. W. A. THERMAL AND CLAY CATALYSED CRACKING IN THE FORMATION OF NATURAL GAS. (Texas A&M, 1981).
194. Ballantine, J. A. The Reactions in Clays and Pillared Clays. *Chemical Reactions in Organic and Inorganic Constrained Systems* 197–212 (1986) doi:10.1007/978-94-009-4582-1\_16.
195. Oh, Y. *et al.* Molecular-size selective hydroconversion of FCC light cycle oil into petrochemical light aromatic hydrocarbons. *Catalysis Today* **352**, 329–336 (2020).
196. Reddy, C. R., Bhat, Y. S., Nagendrappa, G. & Jai Prakash, B. S. Brønsted and Lewis acidity of modified montmorillonite clay catalysts determined by FT-IR spectroscopy. *Catalysis Today* **141**, 157–160 (2009).
197. Margi, N. H. & Yadav, G. D. Molybdenum oxide modified montmorillonite K10 clay as novel solid acid for flow synthesis of ionone isomers. *Molecular Catalysis* **501**, 111362 (2021).
198. McCabe, R. *Inorganic materials*. (John Wiley and Sons, 1996).

199. Constant, S. *et al.* Reactive organosolv lignin extraction from wheat straw: Influence of Lewis acid catalysts on structural and chemical properties of lignins. *Industrial Crops and Products* **65**, 180–189 (2015).
200. Dyckhoff, F., Schlagintweit, J. F., Reich, R. M. & Kühn, F. E. Pushing the limits of activity and stability: the effects of Lewis acids on non-heme iron–NHC epoxidation catalysts. *Catalysis Science & Technology* **10**, 3532–3536 (2020).
201. Selvarajoo, A., Wong, Y. L., Khoo, K. S., Chen, W.-H. & Show, P. L. Biochar production via pyrolysis of citrus peel fruit waste as a potential usage as solid biofuel. *Chemosphere* **294**, 133671 (2022).
202. Chen, R., Sheng, Q., Dai, X. & Dong, B. Upgrading of sewage sludge by low temperature pyrolysis: Biochar fuel properties and combustion behavior. *Fuel* **300**, 121007 (2021).
203. Liew, Y. W., Senthil, ., Arumugasamy, K. & Selvarajoo, A. Potential of Biochar as Soil Amendment: Prediction of Elemental Ratios from Pyrolysis of Agriculture Biomass Using Artificial Neural Network. *Water, Air, & Soil Pollution 2022 233:2* **233**, 1–21 (2022).
204. Alfattani, R., Shah, M. A., Siddiqui, M. I. H., Ali, M. A. & Alnaser, I. A. Bio-Char Characterization Produced from Walnut Shell Biomass through Slow Pyrolysis: Sustainable for Soil Amendment and an Alternate Bio-Fuel. *Energies 2022, Vol. 15, Page 1* **15**, 1 (2021).
205. Hung, C. M. *et al.* Activation of percarbonate by water treatment sludge–derived biochar for the remediation of PAH-contaminated sediments. *Environmental Pollution* **265**, 114914 (2020).

206. Chen, M. *et al.* Biochar nanoparticles with different pyrolysis temperatures mediate cadmium transport in water-saturated soils: Effects of ionic strength and humic acid. *Science of The Total Environment* **806**, 150668 (2022).
207. sen Gupta, S., Sreenivasan Sreepasad, T., Mundampra Maliyekkal, S., Kumar Das, S. & Pradeep, T. Graphene from Sugar and its Application in Water Purification. (2012) doi:10.1021/am300889u.
208. Priya, B. *et al.* Photocatalytic mineralization and degradation kinetics of ampicillin and oxytetracycline antibiotics using graphene sand composite and chitosan supported BiOCl. *Journal of Molecular Catalysis A: Chemical* **423**, 400–413 (2016).
209. Wang, S. *et al.* Catalytic pyrolysis of waste clay oil to produce high quality biofuel. *Journal of Analytical and Applied Pyrolysis* **141**, 104633 (2019).
210. Bu, Q. *et al.* A review of catalytic hydrodeoxygenation of lignin-derived phenols from biomass pyrolysis. *Bioresource Technology* **124**, 470–477 (2012).
211. Chen, X. *et al.* Catalytic fast pyrolysis of biomass: Selective deoxygenation to balance the quality and yield of bio-oil. *Bioresource Technology* **273**, 153–158 (2019).
212. Valizadeh, S. *et al.* Effect of torrefaction and fractional condensation on the quality of bio-oil from biomass pyrolysis for fuel applications. *Fuel* **312**, 122959 (2022).
213. Siddique, N., Suzue, M., Kato, M., Hiromori, K. & Shibasaki-Kitakawa, N. Process optimization for continuous production of sustainable biodiesel from completely non-edible biomass, lignocellulosic hydrous ethanol and waste fatty acids. *Fuel* **289**, 119884 (2021).
214. Abomohra, A. E. F., Wang, Q., Huang, J. & Saad-Allah, K. M. A sustainable approach for bioconversion of food and lignocellulosic wastes into liquid biofuel using a new

- Metschnikowia pulcherrima isolate. *International Journal of Energy Research* **45**, 3430–3441 (2021).
215. Vasaki, M. *et al.* Biodiesel production from lignocellulosic biomass using *Yarrowia lipolytica*. *Energy Conversion and Management: X* **13**, 100167 (2022).
216. Ravanchi, M. T. & Sahebdehfar, S. Catalytic Upgrading of Bio-oil for Production of Drop-In Fuels. *Handbook of Ecomaterials* **3**, 1965–1983 (2019).
217. Kumar, R. *et al.* Lignocellulose biomass pyrolysis for bio-oil production: A review of biomass pre-treatment methods for production of drop-in fuels. *Renewable and Sustainable Energy Reviews* **123**, 109763 (2020).
218. Kyritsis, D. C., Roychoudhury, S., McEnally, C. S., Pfefferle, L. D. & Gomez, A. Mesoscale combustion: a first step towards liquid fueled batteries. *Experimental Thermal and Fluid Science* **28**, 763–770 (2004).
219. Cai, L., vom Lehn, F. & Pitsch, H. Higher Alcohol and Ether Biofuels for Compression-Ignition Engine Application: A Review with Emphasis on Combustion Kinetics. *Energy & Fuels* **35**, 1890–1917 (2021).
220. Scudiere, C., Chen, J.-Y., Dibble, R. & Aznar, M. Investigation of argon oxy combustion with low molecular weight fuels: Improving thermodynamic efficiency. *2017 Fall Technical Meeting of the Western States Section of the Combustion Institute, WSSCI 2017* (2017).
221. Pandiyan, R., Palanisamy, S., Subbiah, L., Velu, R. K. & Samiappan, S. C. Identification and detection of biofuel precursor cumene (benzene, (1-methylethyl)-) by spectroscopic and chromatographic techniques. *Biomass Conversion and Biorefinery 2021* 1–10 (2021) doi:10.1007/S13399-021-02080-X.

222. Gueddida, S., Badawi, M., Aminabhavi, T. & Lebègue, S. Competitive adsorption of phenol and toluene onto silica-supported transition metal clusters for biofuel purification. *Molecular Systems Design & Engineering* **6**, 817–824 (2021).
223. Franck, H.-G. & Stadelhofer, J. W. Production and uses of benzene derivatives. *Industrial Aromatic Chemistry* 132–235 (1988) doi:10.1007/978-3-642-73432-8\_5.